Robust Model-Based Control of Nonlinear Bio-Inspired Autonomous Underwater Vehicles

Cássio Thomé de Faria

Dissertation submitted to the faculty of the Virginia Polytechnic Institute and State University in partial fulfillment of the requirements for the degree of

Doctor of Philosophy
In
Mechanical Engineering

Daniel J. Inman, Co-Chair
Shashank Priya, Co-Chair
Mary E. Kasarda
Andrew J. Kurdila
Michael K. Philen
Pablo A. Tarazaga

August 23, 2013
Blacksburg, VA

Keywords: robust control, model-based, bio-inspired, autonomous underwater vehicles, discrete sliding mode controller.

Robust Model-Based Control of Nonlinear Bio-Inspired Autonomous Underwater Vehicles

By

Cássio Thomé de Faria

ABSTRACT

The growing need for ocean surveillance and exploration has pushed the development of novel autonomous underwater vehicle (AUV) technology. A current trend is to make use of bio-inspired propulsor to increase the overall system efficiency and performance, an improvement that has deep implications in the dynamics of the system. The goal of this dissertation is to propose a generic robust control framework specific for bio-inspired autonomous underwater vehicles (BIAUV). These vehicles utilize periodic oscillation of a flexible structural component to generate thrust, a propulsion mechanism that can be tuned to operate under resonance and consequently improve the overall system efficiency. The control parameter should then be selected to keep the system operating in such a condition. Another important aspect is to have a controller design technique that can address the time-varying behaviors, structured uncertainties and system nonlinearities. To address these needs a robust, model-based, nonlinear controller design technique is presented, called digital sliding mode controller (DSMC), which also takes into account the discrete implementation of these laws using microcontrollers. The control law is implemented in the control of a jellyfish-inspired autonomous underwater vehicle.

Dedication

I dedicate this work to my family. My parents: Alcides and Emilcy. My brothers: Theo, Adriano, Juliano and Tomas. My grantmothers: Cacilda and Romilda. They supported me throughout my life and I'm truly grateful for all their efforts.

Acknowledgements

First, I would like to thank my advisor Dr. Daniel J. Inman for all the support and advices that he gave me during my PhD. I learned a lot from him and I'm grateful for him sponsoring this lifetime adventure of studying in a foreign country.

I would also like to thank my co-advisor, Dr. Shashank Priya for the great opportunity of working on the jellyfish project. It was a fascinating experience to work with such a capacitated group of people.

I would like to acknowledge the financial support from ONR/MURI Jellyfish program, grant number N00014-08-1-0654.

Thank you to all my committee members, Dr. Kasarda, Dr. Kurdila, Dr. Philen and Dr. Tarazaga.

Finally I would like to thank all my friends: from my hometown (Campo Grande/MS/Brazil), from my former university (UNESP/Ilha Solteira/SP/Brazil), from CIMSS and Virginia Tech (Blacksburg/VA/USA), from University of Michigan (Ann Arbor/MI/USA) and the ones spread all around the world. They all, in some way, contributed to the making of this dissertation.

Table of Contents

List of Figures

List of Tables

1. Introduction

Approximately 71% of the earth surface is covered by saline water [1] with a large portion of this area being still unexplored and unprotected. Besides the large surface area occupied by this water-filled portion of the planet, the average depth is quite significant too (about 4.3 km) [2]. This aquatic environment is somewhat hostile to human occupation due to the overwhelming pressure exerted by the large water column and aggressive corrosion due to the salinity. Both of these aspects limit the use of current exploration technologies to unravel and guard the natural wonders of this unknown portion of our planet. A large-scale world effort is then required to expand the human occupation frontier deep into earth's oceans.

The widespread deployment of underwater exploration technologies requires either autonomy or remote operation capabilities of the vehicle itself, since having a human operator inside the vehicle is dangerous and costly [3]. All unmanned exploration platforms are then classified into two groups: remote operating vehicle (ROV) or autonomous underwater vehicle (AUV). The main difference between both groups is that ROV's are connected to a host station through an umbilical cable while the AUV's are untethered. A truly autonomous underwater vehicle would be the ideal exploration tool because it can be easily deployed (no need for operator or host station) and has improved performance (doesn't have to overcome the drag imposed by the umbilical cable).

The need to improve the current methods of exploration of such large underwater areas pushes engineers to develop novel concepts, either in material science or fluid mechanics and to develop platforms capable of fulfilling these searching tasks. Looking into nature's designs and solutions to similar problems has proven itself to be a very effective way of developing these exploration platforms [4]. Biologically inspired (or bio-inspired) solutions rely on the fact that natural selection has been driving organisms to be fully adapted to their environment, *e.g.* the humpback anglerfish that lives in depths of up to 2km where their bodies have adapted to the enormous water pressure.

An optimal solution to the underwater exploration issue would just be a matter of finding an animal that is fully adapted to that reality and understanding the underlying physics that allows such beings to thrive on that harsh environment. Murphy and

Haroutunian [5] provide a great comparison between the capabilities of traditional autonomous underwater vehicles (AUV's) designs and several marine animals. Both groups are compared in terms of the following attributes: variations in body forms, speed and agility, depth capabilities, maneuverability and energetics (cost of transport and endurance). After comparing the capabilities of biological and traditionally engineered systems, the authors concluded that there are systems in certain animal species (or group of species) that can exhibit superior performance to AUV's in one or more of the studied capabilities (*i.e.* speed, depth, etc.).

From all those marine animals investigated one important observation can be made regarding the propulsion mechanism of all nature's "autonomous underwater vehicles", they rely on a oscillatory motion of a flexible body part of these animals. The work of Murphy and Haroutunian [5] provides reasons why the bio-inspired approach should be pursued especially when it comes to improving underwater vehicle speed, maneuverability and overall efficiency for a wide range of travelling speeds (in terms of cost of transport and endurance).

When compared to the traditional propulsion mechanism [6] (where a fixed motor powers a rotating propeller) nature's way to propel itself has proven to be fundamentally different, relying in different fluid-structure interaction (FSI) processes to generate thrust [7]. In nature, the use of body oscillations as a means of locomotion is the dominant design choice, either on running, swimming or flying animals. Only in the bacterial level has a fixed rotary motor been found in nature. The structure is known as bacterial *flagella* motor [8].

At this point it is important to clearly define the two major propulsion design approaches for AUV's: the traditional method, defined by a fixed motor with stiff rotating blades; the bio-inspired (or biomimetic) method, characterized by the oscillation of a flexible part of the vehicle. From the 212 AUV's cataloged in the Autonomous Undersea Vehicle Application Center [9] only 6 were listed as biomimetic. This data indicates the dominance of the traditional design methodology when it comes to commercially deployable platforms. Figure 1.1 presents both the traditional and the bio-inspired designs for comparison.

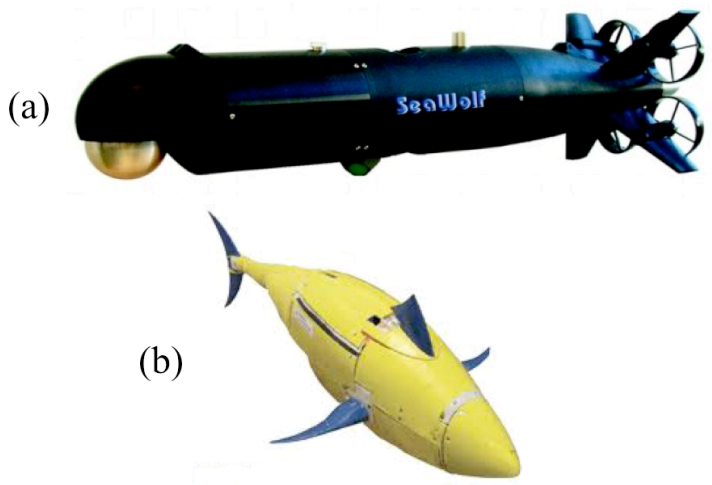

Figure 1.1. Comparison between two types of AUV design (a) traditional (SeaWolf®) and (b) bio-inspired (GhostSwimmer™).

In the past decade more attention has been paid toward the development of bio-inspired autonomous underwater vehicles (BIAUV). As pointed out by previous research [5] each marine animal species have a different set of capabilities and the choice of each one should be used in the biomimetic process is an outcome of the mission requirements for the vehicle. For instance, if the mission requires fast swimming and maneuverability fish-like BIAUV's are preferred [10][11]. One of the most advanced platforms developed so far is the one called GhostSwimmer™, developed by the Boston Engineering Corporation [12].

If payload and maneuverability are the critical issues in a mission then other marine animals with smaller propulsor and large body are the choice, such as, penguins [13], turtles [14] or even manta rays [15]. Rays are one of the most interesting biomimetic platforms and the BIAUV develop by EvoLogic® [15] has good performance and is already commercially available.

For high efficiency and station keeping mission, jellyfish-like vehicles are an appropriate choice [16]. This simple creatures have a very low cost-of-transport [17] and are able to perform maneuvers by asymmetrically contracting its body [18]. Figure 1.2 is a figure of the prototype developed by Villanueva *et.al.* [16].

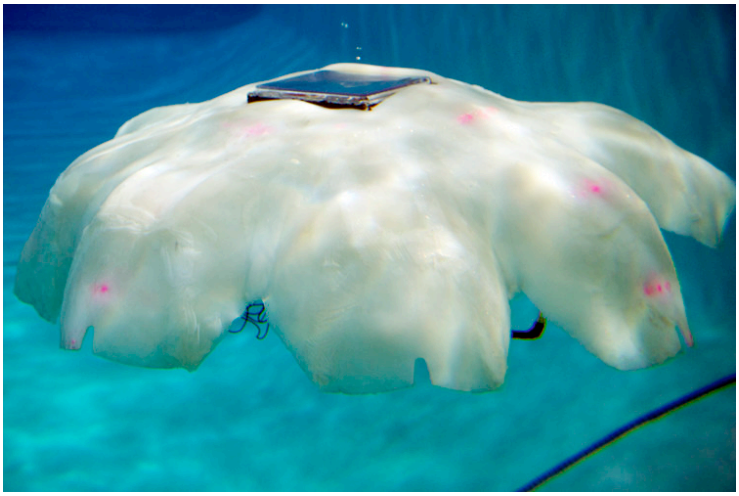

Figure 1.2. Bio-Inspired Autonomous Underwater Vehicle named Cyro developed by Villanueva *et.al.* at Virginia Tech.

It is clear that, exploring biomimetic and bio-inspired designs significantly improve AUV's performance when compared to the traditional design method. But these benefits in maneuverability, speed range and efficiency come at a cost: the increased complexity of the overall system. Now, part of the vehicle's body plays a role on thrust generation and consequently locomotion. In some cases the distinction between body and propulsor is not clear. Besides the development of materials and sensor to adequately emulate the animal abilities, attention also has to be given towards the internal decision-making process of the vehicle that enables its autonomy. This decision-making process is also referred to as the system's controller.

Although there are lots of similarities between a biomimetic vehicle and the marine animal, when it comes to the control logic the bio-inspiration process has to be dealt with a slightly different approach. Because the overall mission of the vehicle is somehow different from what the animal usually does, engineers have to use conventional tools to satisfy the mission requirements. One simple example is the fact that jellyfish cannot be trained to perform station keeping, a requirement for navy applications. However it is still possible to refer to nature for inspiration for more basic control functions, *i.e.* replicating the different swimming gaits of the animal.

Autonomy requires that the vehicle take a series of actions to fulfill the mission requirements, *e.g.* choose an adequate path to follow a target. Conventionally these

decisions are fundamentally classified into three hierarchical levels: mission management, path planning and execution [19].

To better understand these control levels let us use the following hypothetical example, a simple solar powered AUV (with a battery bank) that has to dive to one-tenth of the ocean depth in a given location and stay there until either it runs out of power or it identifies the presence of marine life nearby. After identifying a neighboring animal it has to surface and report the findings to a host station.

The mission management controller is the one responsible to identify the most critical task of the vehicle and command it, *e.g.* if the AUV is running out of power this structure interrupts the primary mission (of finding marine life) and commands a surfacing action to recharge the battery bank. This level is also described as the ship's "captain". Once the command of either diving or surfacing is given to the lower level controllers the path planning stage starts. In this example this level has to identify the current vehicle depth and ocean-floor distance to define how far the vehicle is from the target position (either the water surface or the one-tenth-depth requirement). Execution control is then responsible to actuate the vehicle to achieve the specified depth. Notice that there is a directional flow of commands between the control levels and at each stage different sensory inputs are required.

Although the lowest level controller does not directly affect the decision-making process of higher levels, it is the single most important component of the entire process. Without the proper execution all the higher level commands fail. That is why a large number research papers focus on the control of the actuators in traditional AUV using different execution controller design strategies, such as sliding mode [20], Proportional-Integral-Derivative [21] and fuzzy logic [22]. These papers focus on creating a relationship between a sensor measurement (*e.g.* depth, orientation, etc.) and the input to the vehicle (*e.g.* propeller motor voltage, rudder angle, etc.). Some authors agree that incorporating the thruster dynamics into the controller design, *i.e.* modeling the actuator, can significantly improve the vehicle performance [23][24].

For bio-inspired AUV the common approach is to implement these traditional techniques [25][26] despite their radically different thrust generation mechanism. As pointed out by Yoerger *et.al.* [23] and Loueipour & Hadian [24] even for traditional

(motor propelled) incorporating the actuator dynamics into the controller design can significantly improve the vehicle performance. Very few authors have incorporated the oscillatory component that is inherent to bio-inspired propulsion into the description of the control law [27][28][29]. The idea was to represent the thrust generation as a nonlinear oscillatory dynamic system and incorporate this as part of the controller design process. These ideas are recent [27][28][29] and are trying to keep up with the rapidly changing mechanism of propulsion generation for underwater locomotion, but there is still a lot to be discussed and developed when it comes to specific controller design tools of bio-inspired propulsion.

In face of this reality, this study is devoted to create a generic framework for the execution control level of oscillatory system with particular interest in autonomous underwater vehicles applications. Because the generation of a net thrust by the BIAUV relies on a cyclical motion the incorporation of this information in the controller design process could lead to improvements in the overall performance of the system. To simplify the notation throughout this document the execution control level will be simply called as the system control/controller.

The initial step is to provide an appropriate mathematical description of the problem being dealt by defining a generic nonlinear dynamic expression for the AUV system. Notice that the system is presented in normal (canonical) form and describes an explicit time-dependent nonlinear dynamic system:

$$\begin{aligned} \dot{\boldsymbol{\eta}} &= \boldsymbol{f}(\boldsymbol{\eta}, \boldsymbol{\xi}, t) \\ \dot{\boldsymbol{\xi}} &= \boldsymbol{f}_a(\boldsymbol{\eta}, \boldsymbol{\xi}, t) + \boldsymbol{G}_a(\boldsymbol{\eta}, \boldsymbol{\xi}, t)\mathbf{u} \end{aligned} \tag{1.1}$$

where $\boldsymbol{\eta}$ and $\boldsymbol{\xi}$ are state vectors, t is the time, $\boldsymbol{f}$ and $\boldsymbol{f}_a$ are the dynamic vector fields, $\mathbf{G}_a$ is the input matrix and $\mathbf{u}$ is the input vector. The over-dot represents differentiation with respect to time. Equation (1.1) is very convenient way (in the controller design perspective) to represent, for example, the AUV error kinematics ($\boldsymbol{\eta}$) and dynamics ($\boldsymbol{\xi}$) under the presence of external propulsion forces ($\mathbf{u}$).

The dynamic vector fields and input matrix are a function of time because in this type of system the propulsion generation is related to body oscillations which leads to dynamic property changes over time. This time dependence incorporates the inseparability between body and propulsor on a BIAUV. The uniqueness of the problem

described by equation (1.1) arises when the input vector (*e.g.* propulsion forces) is defined as an oscillatory component, which will be defined here by the period (T), the average cycle value ($\mathbf{u}_{avg}$), a deviation amplitude distribution over the period ($\mathbf{u}_{dev}$) and a phase difference between inputs ($\boldsymbol{\varphi}$). Figure 1.3 illustrates the thrust force from a bio-inspired propulsor and shows the oscillatory characteristics.

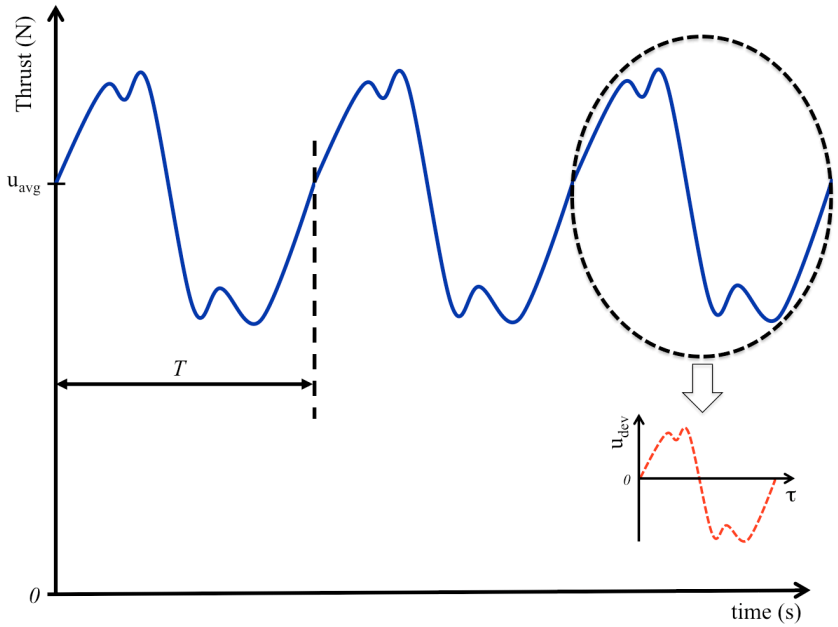

Figure 1.3. Properties illustration of an oscillation thrust force. In detail the plot of the $\mathbf{u}_{dev}$ component is shown, it corresponds to the thrust profile generated over a period minus the average thrust.

The properties associated with the periodic input were defined as vector quantities (bold variables) so that this mathematical description is generic enough to accommodate systems that have more then one bio-inspired propulsor. The input vector can be written as a function of the oscillatory characteristics:

$$\mathbf{u} = \mathbf{u}\left(T, \mathbf{u}_{avg}, \mathbf{u}_{dev}, \boldsymbol{\varphi}\right) \tag{1.2}$$

It is critical for the controller design that the pulsating input is properly taken into account. Because this term is a result of a complex fluid-structure interaction process it is usually highly nonlinear and an appropriate model it is either not available or demands intensive numerical computations.

Another important factor is the choice of an appropriate control variable for the system. This becomes an issue due to the nonlinearity of the problem that allows, for example, a frequency dependent (inverse of T) average propulsion magnitude ($\mathbf{u}_{avg}$). A wise choice of control variables could not only lead to an overall vehicle efficiency improvement but also simplify the mathematical description of the problem.

Presenting a discussion on why to choose a specific control variable is one of the main objectives of this dissertation. Chapter 2 is dedicated to presenting a simple model that is able to capture the most basic oscillating thrust generation mechanism from a fluid-structure interaction process. Experiments were conducted to validate the modeling approach.

The main phenomenon to be explored in these oscillatory systems is the resonance: a constructive interference process between states of a dynamic system. There is a set of requirements that define the existence of resonant modes in an arbitrary system [30]. A more mathematical interpretation for resonance is the one that points out divisions by zero (or sufficiently small number) in the dynamical system, resulting in large amplitude responses. Poincaré described this as “the fundamental problem of dynamics”.

When it comes to promote the resonance on a submersed oscillatory structure there are three variables that play a significant role in the process: period, amplitude and structural stiffness. For a generic system its resonant modes are a function only of frequency (for linear resonance) and frequency and amplitude (for the nonlinear case). Changing structural stiffness of the oscillator dislocates the entire process on the frequency domain. It is interesting to notice that nature uses these variables while performing swimming, as pointed out by McHenry *et.al.* [31]. The fact that fish have these capabilities could indicate that resonance is indeed explored by animals for underwater locomotion.

The implementation of swimming gaits that takes advantage of resonant effects has to be done in the execution control level. As an example as a command is sent requiring the vehicle to reach a certain speed the BIAUV has to choose a set of oscillating frequencies, amplitudes and structural stiffness, not only to satisfy the speed requirement, but also to keep the system operating under a resonant-mode. Defining an appropriate controller to

fulfill such requirements is not a trivial task and requires a design iteration method/process.

There are two approaches when it comes to the execution level controller design, it could either be model-based or non-model-based approach. The difference between each one is the development (or not) of a mathematical relation that is able to predict the behavior of the system to be controlled. If the dynamic model is available and is reliable, one can use a model inversion process to define an appropriate input that results in the desired dynamics, the inversion characterizes model-based approaches. Several controller design techniques can be listed as model-based, such as, LQR, feedback linearization, backstepping, sliding mode, etc [32]

The alternative design method involves choosing an arbitrary function and tuning the parameters (gains) until the system has the desired performance. Typical examples of non-model-based techniques are PID and fuzzy logic controllers [33]. To overcome the challenges of tuning the controller several adaptive techniques has been proposed for this class of controllers and always involves the computation of a performance index that has to be maximized/minimized [33].

Independently from the control approach chosen by the designer the technique has to be able to deal with three specific intrinsic characteristics of these dynamics systems: the periodicity, nonlinearity and uncertainties/disturbances. While the first two issues are caused by the BIAUV complexity the third is environmental. In underwater operations there are a large number of ambient factors that can affect the vehicle's behavior, such as changes in water salinity, small flow currents, etc. A controller that can deal with these changes in operation conditions and still perform adequately is defined as a robust technique.

A robust controller is one that responds in a satisfactory manner even when the systems are operating in conditions different then the ones it was designed. An effective way to impose robustness is through negative feedback, *i.e.* measuring the current system state and using that information in the decision-making process of the future input. This closed-loop system improves the response of the system under the presence of disturbances because it takes into account what is actually happening to the systems to

control it [34]. Because of this robustness advantage the closed-loop (feedback) strategy will be applied throughout this work.

Another important discussion to be made regarding the control architecture is the use (or not) of a mathematical model in the design of the system's controller. Although the derivation, identification and verification of a model are costly processes it can also be very productive. The development of a model for the dynamic system allows for virtual tests on the system a property that, not only can be used to predict controller responses, but can also help identifying physical parameters that have to be changed to improve the BIAUV performance.

The model-based controller design approach, besides providing insight into the system behavior a priori, significantly reduces the need for controller tuning. It requires from the operator a great knowledge of the system that is being dealt with and reduces the computation requirements for the onboard electronics when it comes to this decision-making process. For these reasons the model-based design approach was pursued. Figure 1.4 illustrates the architecture chosen for the controller of BIAUVs, a feedback, model-based approach. Notice that it is also shown that higher order control structures can still command the control law by a direct input mechanism.

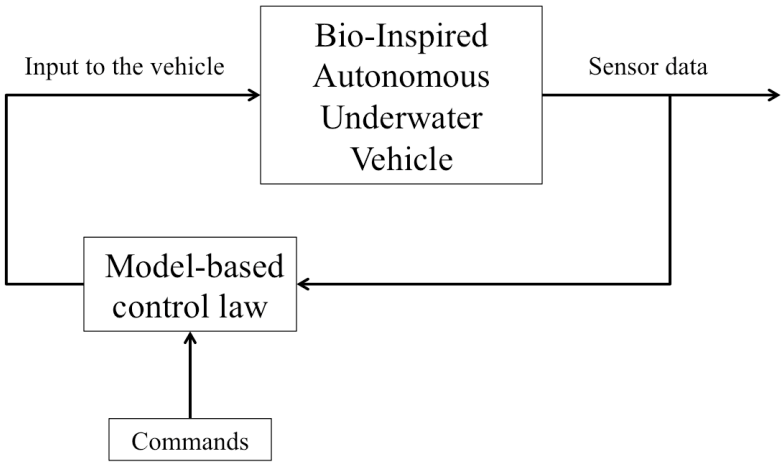

Figure 1.4. Selected robust control structure.

From the controller design methodologies available for nonlinear systems the sliding mode control (SMC) is one of the most suitable and has been extensively applied to

current AUV technology [20][35][36]. The resulting control law is inherently robust because it was designed to operate under the presence of structured uncertainties (changes in the model parameters used to describe the system dynamics). An example of structured uncertainty is the addition of mass to the system during operation, if the model already takes into account inertia, the mass increment will only create more inertia and not create an unexpected dynamic behavior. In this example the controller should be able to compensate for this unexpected system change and maintain satisfactory response.

Sliding mode controller (SMC) is the use of variable structure systems theory [37] as a design tool to create a feedback control law that stabilizes a continuous-time dynamic system. The overall idea behind this design method is to use different input structures to attract the state to an asymptotically stable hyperplane, also called a switching surface or sliding manifold. Once, the stable hyperplane has been reached the state "slides" asymptotically to the equilibrium point over that manifold.

The SMC operates in three different modes: reaching (RM), sliding (SM) and steady state (SS). When the current state is not on a desired sliding surface, the reaching mode creates a "force" to drive the current state to the desired sliding surface. If the state was successfully driven to the switching surface the sliding mode takes over and pushes the state along the sliding manifold until the equilibrium point is reached. Finally the steady-state mode is activated keeping the system at its equilibrium.

The continuous-time (analogic) implementation of a control law requires the design of a specific electric circuitry that has the dynamic behavior designed for the controller. Although it is a very effective method of realizing the controller it has some drawbacks, especially when it comes to making any sort of change to the original circuitry, which requires a hardware modification. On the other hand a discrete (digital) implementation, through a microcontroller, is more lenient because it allows changes via software modifications.

Digital implementation of control laws has several advantages when compared to analog laws, such as: noise rejection, high reliability and low overall cost [38]. All these advantages come with the addition of a sampling apparatus, which transform the continuous-time states of the dynamic system into a set of discrete values. Figure 1.5 illustrates the principles of the discretization process for the type of control architecture

being explored in this research. Notice that the control law now is discretely commanding the BIAUV (continuous system dynamics) behavior.

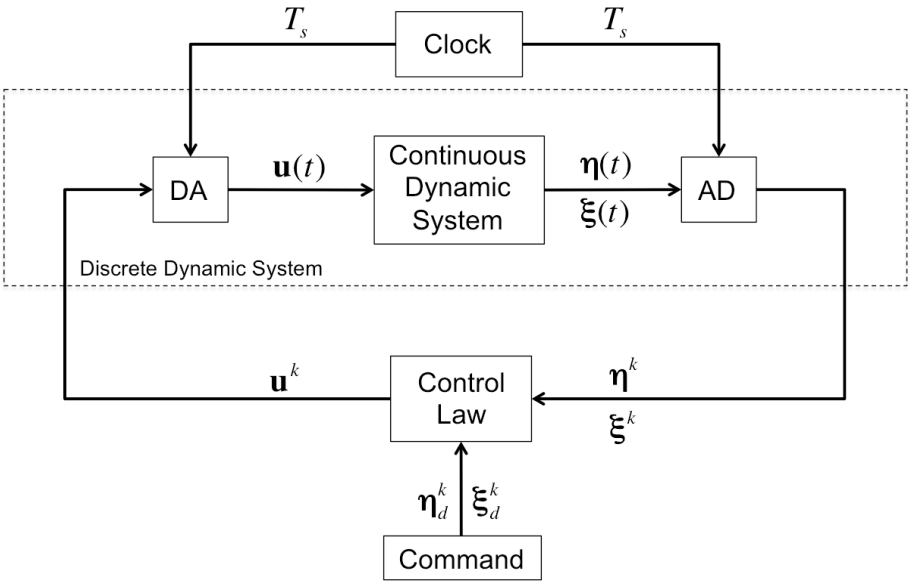

Figure 1.5. Discrete control structure implementation with sampling time T_s. Digital-to-analogic (DA) and analogic-to-digital (AD) conversions are expressed in terms of dynamic blocks.

Because the system to be controlled also involves the sampling process there is a need to investigate and compensate for the effects of this new discrete system. Chapter 3 of this dissertation presents the development of a new controller design technique, the discrete sliding mode controller (DSMC). This novel methodology fills a gap in current literature to address the implementation of the sliding mode theory using microcontrollers (digital systems) in an attempt to improve the controller performance and understand its limitations.

Besides of all the advantages of the digital implementation previously mentioned this sampling process could also be used as means to compensate (or even eliminate) the oscillatory component that is inherent in BIAUV dynamics. If the sampling time is appropriately selected these oscillations could be rejected by the discrete dynamic system either by averaging or by matching the periodicity of the propulsor.

This last piece of theory enables a complete discussion on several control architectures for bio-inspired autonomous underwater vehicles. In chapter 4 a generic BIAUV model is used to exemplify the implementation and provide a comparison between some relevant control architectures that satisfies the requirements previously presented in this chapter.

In short, the author recognizes the need to explore earth's oceans by using bio-inspired autonomous underwater vehicles solutions and tries to provide a generic framework for a control structure for these types of vehicles. A proper controller design and implementation can improve the overall system performance (maneuverability, cost-of-transport, endurance, etc.) and consequently broaden the use of this exploration technology.

First, by investigating the fundamental characteristics of thrust generation in submersed flexible structures, an appropriate control variable is determined (chapter 2). Chapter 3 develops a robust, discrete, model-based, nonlinear control theory that can be applied to these bio-inspired systems, a fundamental tool to address the oscillatory characteristics of the propulsion. Chapter 4 demonstrates the capabilities of the framework on an assumed AUV model considering some different control architectures. Finally a series of conclusion are drawn from the work developed in the previous chapters and are compiled into a final statement of the accomplishments of this research.

2. Defining the Control Variable

Several engineering applications rely on the energy transfer between domains, *e.g.* thermal energy converted into motion. An understanding on how the transfer occurs empowers designers with appropriate tools and concepts to maximize, or minimize, this process. Mathematical models that adequately describe the interference between two or more physical domains are commonly defined as multidisciplinary. A more particular nomenclature is given to problems that involve fluid and structure interactions (FSI).

FSI is key for the propulsion of underwater vehicles, since the motion of a structural component (*e.g.* rotating propeller) displaces a portion of fluid, creating a reaction force that displaces the vehicle. It is easy to see that the mechanical energy of the structure/vehicle is transferred to the surrounding fluid, propelling the vehicle. For the traditional propulsion design, *i.e.* stiff revolving propellers, the structural deformation is not taken into account in the model, a reasonable assumption that significantly simplifies the problem. When it comes to bio-inspired propulsion, that might not be the case as the structural deformations can play a significant role in the thrust generation process.

This chapter presents a very simple analytical FSI model that captures the three basic features of the propulsion problem: structural flexibility, energy transfer between physical domains and unsteady flow. This model allows for inferences on the nature of the thrust generation process and predictions of optimum operation points (maximizing thrust production) on an oscillatory bio-inspired propulsor.

Initially a bibliographical review of the fluid-structure interaction model is presented in section 2.1, followed by a description of the new model being proposed by the author in section 2.2. The experimental setup is presented in section 2.3 where the results are discussed in order to validate the mathematical approach. Section 2.4 explores some numerical thrust predictions when a sinusoidal force input is applied to the structure. Finally a discussion is presented on why the use of oscillation amplitude as a control variable could improve the overall performance of a bio-inspired propeller.

2.1. Bibliographical review of fluid-structure interaction models

This review focus on a subclass of the Fluid-Structure Interaction (FSI) problems: solid slender-body structures, particularly beams, actively vibrating in incompressible Newtonian fluid, as they can represent propulsion generation in fish-like structures [1], etc. The mathematical foundation for this kind of problem was developed by Rayleigh [40][41]. In practice the problem is usually addressed by ignoring one domain, disregarding coupling effects that could be beneficial for the application itself. Wu [42] ignored the structural domain, assuming that the plate induced a known displacement to the surrounding fluid. Using potential flow theory, he evaluated the pressure distribution and accessed the lift and drag forces on the plate produced by such oscillations.

Lindholm [43] provided vast experimental data and analytical developments on the structural side of the problem, disregarding the flow patterns created by the plate oscillation. Lindholm's goal was to predict and understand generation of high frequency noise by the structure, a recurrent phenomenon in ship design in the 1950s. The plate equation was modified considering that the fluid added inertia to the system and the apparent mass was calculated based on the pressure distribution around the plate using strip theory. A ratio between the natural frequency of the plate in air and water was derived for each mode shape and results were compared to experimental data. One important observation was the fact that mode shapes in water were fairly similar from the ones observed in air.

In the late 1960s and early 1970s researchers started using the term fluid-structure interaction (later know by the acronym FSI) to describe analysis that would take in account the reciprocal effect on both domains [44]. Several fluid mechanists, interested in understanding fish locomotion, developed elegant coupled analytical models that provided great insight on the physics of the problem [1][45][46]. The flow around the oscillating structure was described in terms of a known unsteady flow potential, which was used in the calculation of a pressure field and then combined to the structure elasticity and inertia. Unfortunately for simplification and comparison reasons, the structural inertia was dropped out of the analysis, *i.e.* ignoring the fluid-structure resonance phenomenon. Haddara and Cao [47] addressed this issue by lumping the fluid effects into an added mass term to allow an analytical solution.

Following the drastic improvement in computational power, several numerical methods (discrete) were developed to describe complex fluid behaviors. Fu and Price [48] laid out a complete structural and fluid model (independent of each other), where the flow potential was resolved using a panel method and the structure using the finite element method. The more elaborate FSI analysis allowed a discussion on the coupled system damping and pointed out differences between fluid effects on lower and higher mode shapes of the structure.

Discrete methods introduce a gap between domains requiring coupling strategies to be implemented as part of the solution algorithm. Maity and Bhattacharyya [49] describe the most common approaches to the problem and give several references on each. Several other researchers contributed on improving the computational fluid dynamics (CFD) side of the problem [50][51][52]. Although these methods improve the representation of such complex coupled systems, they do not provide an explicit interpretation of the underlying physics.

In trying to understand the basic mechanism originating from the coupling of both domains and to reduce the computational power required to describe the phenomenon, a large number of papers were published on the analytical development of the problem [53][54][55][56]. Despite the insights on added inertia and thrust/drag obtained by these models, few try to discuss the damping introduced by the surrounding fluid and its impact on energy transfer across the domains. Another important aspect of these models (and most FSI research and literature) is that they usually focus on flow-induced vibration disregarding the bi-directionality of the problem, *i.e*. vibration-induced flows.

Permanent energy exchange was investigated by Tang *et.al*. [57], who focused on the energy transferred to the structural domain by the fluid, enabling the concept the authors call "flutter mill." The analysis was based on several numerical simulations each one with different parameters. The design of such energy harvesting devices and other engineered systems relies on an understanding of how the coupling process takes place.

2.2. FSI model formulation

Interested in explaining the interaction between fluid and structural domain, we developed a simple analytical model that captures the most basic features of the

phenomenon. The resulting differential equation that represents the coupled system behavior has two new components (when compared to just the structural model): an increase in inertia and energy transport diffusion to the adjacent media, *i.e*. the fluid.

Assuming that structural mode shapes are not affected by the presence of a surrounding fluid is a key concept of the modeling process. Although such hypothesis is generally considered to be valid by several authors in the literature [58], an experimental test was performed to evaluate the cantilevered beam lower mode shapes and its modal properties.

The novelty of the proposed approach is based on the effects of the fluid motion into the structural damping, a parameter that has been neglected in past studies and that carries important information on the permanent energy exchange across domains. The modeling process starts by assuming a form to the flow field that takes into account the beam vertical displacement. A forcing function on the beam due to fluid reaction is obtained from this flow expression using the Navier-Stokes equation. The solution of the Euler-Bernoulli beam equation under the presence of this forcing term results in the definition of both structural displacement and flow field simultaneously. This process is described in detail in the following subsections.

2.2.1. Fluid domain model

The evaluation of pressure fields around a body/structure immersed in a fluid that has a prescribed motion is quite a complex problem. Several researchers and engineers appeal to discrete (numerical) methods to obtain such data. Examples can be found in Maity and Bhattacharyya [49]. A less common approach is to develop analytical solutions, which carries more physical meaning, but requires a large number of simplifications, *e.g*. Haddara and Cao [47].

In order to understand the coupling mechanism between the beam and surrounding fluid a simple analytical model in both domains is required. Figure 2.1 provides an illustration of the simplified model used here. An active cantilevered beam, of length (L), is immersed into a fluid. It is important to notice that the beam motion (y_b) is only activated in the y-direction.

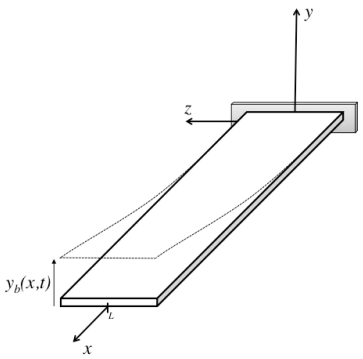

Figure 2.1. Coordinate reference frame of a vibrating beam immerse in a fluid.

The fluid is Newtonian and the flow is considered to be incompressible and two-dimensional, *i.e*. there is no fluid-velocity component or gradients in the *z*-direction. The flow over the beam is assumed to have the same vertical (*y*) velocity as the beam, which can be found by deriving the beam *y*-position (y_b) with respect to time. Separation of variables is assumed throughout this work to describe the beam displacement:

$$y_b(x,t) = X_i(x)T_i(t) \tag{2.1}$$

where $X_i(x)$ is the beam mode shape and $T_i(t)$ is the temporal solution.

The induced fluid velocity component by the beam, in the *y*-direction (v), is considered to exponentially decay with the fluid particle distance from the vibration source. This assumption is not far from flow field obtained by Haddara and Cao [47] using potential flow theory. Mathematically this concept is described by:

$$v(x,y,t) = a_1(x,t)e^{-\sigma y} \tag{2.2}$$

where a_1 is the magnitude coefficient to be determined by the boundary conditions of the problem and σ is the decay rate (always greater then zero). Physically this negative exponential defines a volume of fluid over the beam that is affected (displaced) by the structural motion.

At an infinite distance from the beam there is no flow in the *y*-direction and at the beam the fluid *y*-velocity is equal to the beam *y*-velocity. At this point the vertical axis is divided into two, an upper side (above the beam) and a lower side. Figure 2.2 illustrates the boundary conditions and both regions.

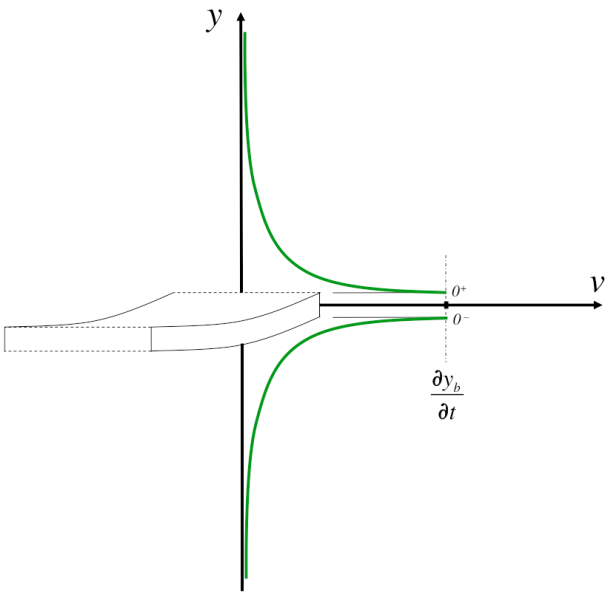

Figure 2.2. Boundary conditions for the upper (+) and lower (-) regions (vibration induced *y*-velocity).

It is important to notice that in this analysis the beam thickness is discarded once it is small compared to the theoretical infinite distance. As a result a *y*-velocity field is found for each region, where the positive superscript denotes the positive region of the *y*-axis and negative superscript denotes the negative region:

$$v^{+} = \frac{\partial y_b}{\partial t} e^{-\sigma y} \tag{2.3.a}$$

$$v^{-} = \frac{\partial y_b}{\partial t} e^{\sigma y} \tag{2.3.b}$$

The continuity equation for this type of flow can be written as:

$$\frac{\partial u}{\partial x} + \frac{\partial v}{\partial y} = 0 \tag{2.4}$$

Using eq. (2.4) the flow velocities in the *x*-direction (u) can be described for each region:

$$u^{+} = \sigma e^{-\sigma y} \int_{-\infty}^{x} \frac{\partial y_b}{\partial t} dx \tag{2.5.a}$$

$$u^{-} = -\sigma e^{\sigma y} \int_{-\infty}^{x} \frac{\partial y_b}{\partial t} dx \tag{2.5.b}$$

The velocity fields have been determined, eqs. (2.3) and (2.5), permitting the evaluation of fluid momentum on the *y*-direction (Navier-Stokes equation).

$$\rho\left(\frac{\partial v}{\partial t}+u\frac{\partial v}{\partial x}+v\frac{\partial v}{\partial y}\right)=-\frac{\partial P}{\partial y}+\mu\left(\frac{\partial^2 v}{\partial x^2}+\frac{\partial^2 v}{\partial y^2}\right) \tag{2.6}$$

where P is the pressure field, ρ is the fluid density and μ is the flow viscosity. The body force in the fluid, in this case pressure field, is the only unknown of the problem. Equation (2.6) can be evaluated in each region (upper and lower), resulting in a pressure gradient for each side of the beam. By integrating the resulting gradients from the beam surface to a infinite distance and assuming that the pressure at a far point is the same in both sides of the beam, the pressure difference between top and bottom surfaces is the following (a complete derivation is presented in the appendix A):

$$P^- - P^+ = \Delta P = \frac{2}{\sigma}\left[\mu\left(X''_i+\sigma^2 X_i\right)\right]\dot{T}_i - \frac{2\rho}{\sigma}X_i\ddot{T}_i \tag{2.7}$$

where the superscript prime denotes a spatial derivative and over dot a time derivative.

The resulting expression described by eq. (2.7) can be interpreted as a forcing function per unit area on the beam (in the *y*-direction). To define this pressure field about the structure, knowing the fluid properties and the beam displacement is necessary.

2.2.2. Fluid-Structure interaction model

Structural dynamics is directly affected by the external forces applied to the system as stated by the Newton's law; these forces are also affected by the structural motion and become part of the dynamic system. Dealing with these interconnected systems is a challenge in fluid-structure interaction problems [49]. The most direct way to deal with this problem is to ignore the coupling effects and treat them as independent domains. This concept can be extended to an interative approach, where they are independently solved until both results converge to the same value. The more elegant solution is to treat them as a single system and simultaneously provide a solution for both. This later technique will be employed in this work to provide an analytical solution for the problem under consideration.

The pressure difference distribution across the beam described by eq. (2.7) times its width (w) could be interpreted as an external force (per unit length) applied at the

beam. Considering a viscously damped (D) and homogeneous Euler-Bernoulli beam (constant bending stiffness EI and density ρ^*), the dynamic equation can be written as:

$$\rho^* hw \frac{\partial^2 y_b}{\partial t^2} + Dhw \frac{\partial y_b}{\partial t} + EI \frac{\partial^4 y_b}{\partial x^4} = w\Delta P \tag{2.8}$$

The piezoelectric actuator used in the experiments is not directly taken into account into the model. The reasoning behind this is the fact that the micro-fiber composite (MFC) patches have a relatively small mass when compared to the overall structure. A similar reasoning also applies to the actuator stiffness.

Combining eq. (2.8) with the pressure distribution definition, eq. (2.7), and rearranging the terms yields:

$$\ddot{T}_i + \frac{2}{\left(1+\frac{2\alpha}{h\sigma}\right)}\left[\frac{D}{2\rho^*} - \frac{\mu}{\sigma h \rho^*}\left(\frac{X''_i}{X_i} + \sigma^2\right)\right]\dot{T}_i + \frac{c^2}{\left(1+\frac{2\alpha}{h\sigma}\right)}\frac{X''''_i}{X_i}T_i = 0 \tag{2.9}$$

where h is the beam thickness, α is the ratio between fluid density (ρ) and beam density (ρ^*) and c^2 is the ratio between bending stiffness (EI) and the linear mass distribution ($wh\rho^*$).

From this point on, the goal is to determine both time and spatial functions of eq. (2.9). A key assumption made here is that the mode shapes are the same for the case where no fluid interacts with the structure, *i.e.* beam vibrating in vacuum. Besides being a common assumption throughout models in the literature [58], there is experimental evidence that such hypothesis could be valid for lower mode shapes of beams [43].

For such conditions these spatial functions are widely found in literature for several boundary conditions [59] and also satisfy the following:

$$\frac{X''''_i(x)}{X_i(x)} = \beta^4 \tag{2.10}$$

where β is the wave number of the mode shape considered. This assumption is experimentally verified in latter section of this paper.

Equation (2.9) can be manipulated to assume a damped spring-mass system form:

$$\ddot{T}_i(t) + 2\zeta(x)\omega_n \dot{T}_i(t) + \omega_n^2 T_i(t) = 0 \tag{2.11}$$

where:

$$\zeta(x) = \frac{2}{c\beta^2\sqrt{\left(1+\frac{2\alpha}{h\sigma}\right)}}\left[\frac{D}{2\rho^*} - \frac{\mu}{\sigma h\rho^*}\left(\frac{X''_i}{X_i} + \sigma^2\right)\right] \tag{2.12.a}$$

$$\omega_n^2 = \frac{c^2\beta^4}{\left(1+2\alpha/h\sigma\right)} \tag{2.12.b}$$

The modal damping ratio (2.12.a) is a key term in this model, as it is responsible for a permanent energy transfer between the two domains. The term is composed of two different sources: beam viscous damping (D) and fluid viscosity (μ).

Viscous damping is the component responsible for energy dissipation within the structure due to its internal friction. This term is inherent to the beam and will be the only damping mechanism when there is no fluid around it. The other two terms arise exclusively from the presence of and interaction with the fluid. Fluid viscosity is by definition a diffusive term since it transports momentum if there exists a velocity gradient.

The natural frequency (2.12.b) also carries information about the coupling. The density ratio (α) indicates that an added mass is now part of the system and this inertia increase reduces the natural frequency of the coupled system. The resonance frequency of a beam in vacuum is obtained by setting α to zero. One can then compute the frequency shift induced by submerging the beam into a Newtonian fluid by the following expression.

$$\lambda = \frac{\omega_{fluid}}{\omega_{vacuum}} = \sqrt{\frac{1}{\left(1+\frac{2\alpha}{h\sigma}\right)}} \tag{2.13}$$

This expression is similar to the ones described by Lindholm [43] and clearly indicates the added mass effect described earlier. In fact this is one of the most common approaches to the fluid structure interaction problem. For instance Han and Xu [60] view the surrounding fluid as an added mass to the vibrating mechanical system.

Equation (2.11) is a second order homogeneous differential equation that can be directly solved assuming all other parameters (boundary conditions, mode of vibration, initial conditions, material and fluid properties) are known.

A more generic solution of the coupled system can be found by assuming that the superposition principle holds for the beam displacement, *i.e.* the total beam displacement (y_b) is the sum of the ith mode shape (X_i) times the ith temporal function (T_i).

The Galerkin's method [61] is then applied to define the temporal functions. The method consists in multiplying eq. (2.11) by the ith mode shape and by the jth mode shape, integrating the resulting equation over the spatial domain (from zero to the beam length). One could compose a set of N differential equations with N variables, $T_i(t)$, by choosing a finite number of mode shapes (N) to represent the problem. A numerical method, such as Runge-Kutta, can then be used to solve the temporal domain. Appendix B presents the derivation of the method for the problem at hand under the excitation of an arbitrary external force.

2.3. Experimental validation of the FSI model

2.3.1. Experimental setup

An experiment was designed to access three different characteristic of a cantilevered beam vibrating in Newtonian fluids. The goals are to verify the hypothesis that mode shapes are not affected by the presence of surrounding fluid, to characterize the change in natural frequency imposed by the coupling of both domains and finally to define the damping ratio's spatial and modal dependence.

The test beam is made out of O1 tool steel, with density of 7800 kg/m^3 and Young's modulus of 214 GPa. The beam is 1.6 mm thick, 19 mm wide and 300 mm long. Six measurement points were evenly distributed across the beam, the first one at the free end and the sixth one at the clamped end; in each of these points a circular reflexive tape, with 5 mm diameter, was attached. An experimental setup and the beam are presented in figure 2.3.

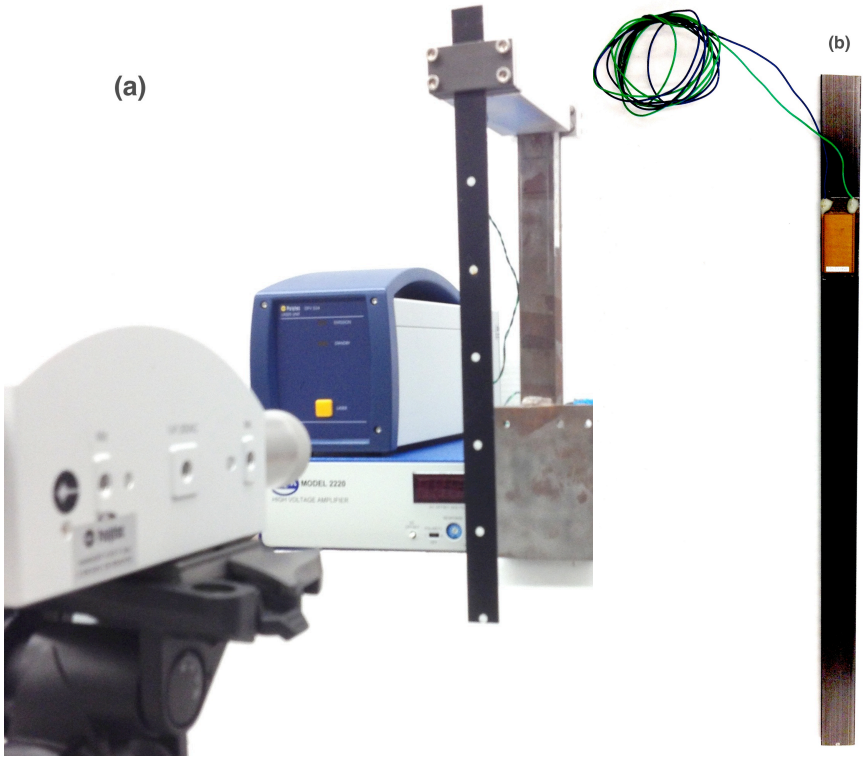

Figure 2.3. Beam utilized in this experiments (a) Experimental setup for tests in air (b) test beam before final preparation with detail on the MFC patch.

Near vacuum tests were performed in a Tenney® environment chamber 36ST at 10 torr; such low pressure was assumed to be the "fluid-less" condition. Both tests in air and water were performed inside a glass aquarium to minimize external sources of flow perturbations around the test beam.

To excite the structure a Micro-Fiber Composite (MFC) patch M2814P1 (38mm x 20mm) from Smart Material® was bonded close to the clamped end of the beam. The actuator mass and stiffness added to the base structure is not taken into account by the model. Only 10.67% of the beam's length was covered by the active material, which also has a stiffness 14 times smaller then the host structure and the actuator's mass is about 0.9% of the beam. MFC's were chosen because they are light weight, flexible, encased in kapton and have a much higher coupling coefficient thus producing more actuation force per input control voltage.

Velocity measurements were conducted using a Polytec® OFV 303 laser head and an OFV 3001 signal conditioner. The sensitivity of the laser measurement was 125

mm/s/V and a velocity filter of 20 kHz. Data was acquired using a Siglab® data acquisition system model 20-42 with 4 input channels and 2 output channels. A sampling frequency of 2.6 kHz was chosen to collect data, with 8192 points per observation, yielding in a frequency resolution of 0.317 Hz. If the input data from the laser vibrometer exceeded the channel limit (2.5 V) the data set was rejected. The data was processed using 50% overlap and Hanning windowing, the resulting frequency response function was then averaged over previous measurements of the same point. The final result was obtained when 100 measurements were performed and averaged using the adding method.

The input applied to the MFC patch was a band-limited white noise signal, with root mean square average of 0.9 V, without offset and limited at 1000 Hz. This signal was amplified two hundred times by TREK® amplified model 2220 and then applied to the MFC patch.

2.3.2. Experimental results

The resulting frequency response functions (FRF) at the beam tip for the beam in three different media are presented by figure 2.4.

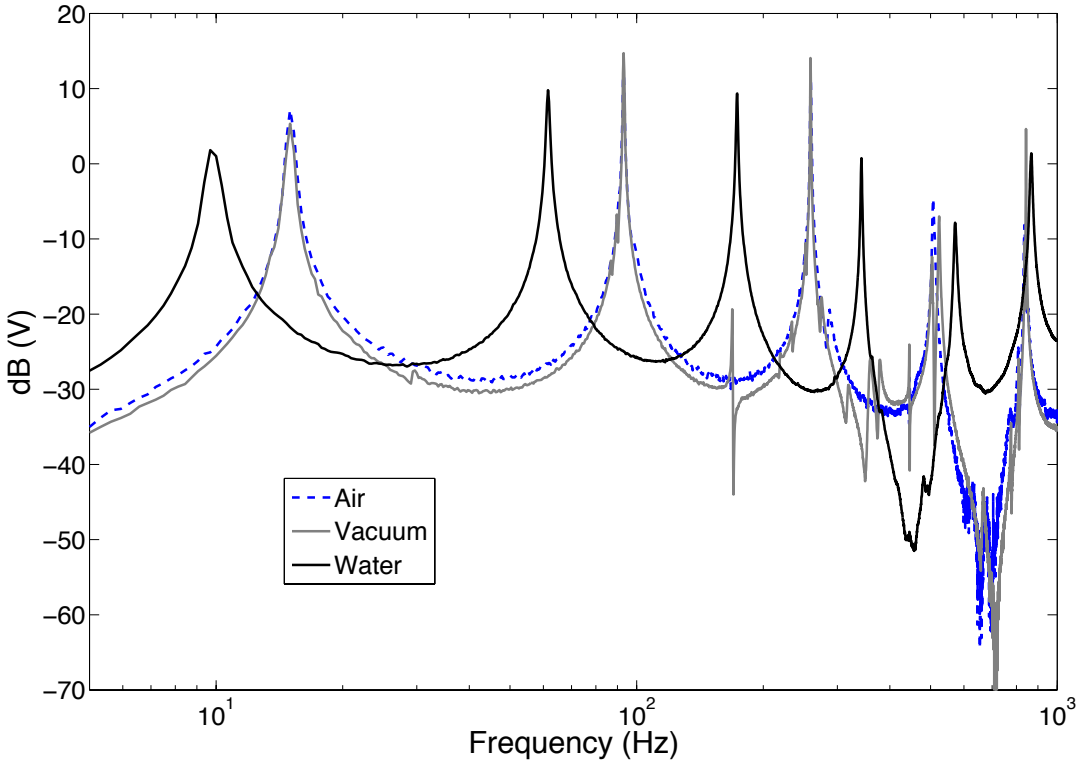

Figure 2.4. Magnitude FRF of a cantilevered beam in three different media (at the beam tip).

Modal information was extracted by analyzing each one of the peaks in the magnitude FRF, in that same frequency a crossing had to be observed in the phase FRF plot. The frequency in which the peak occurred was chosen as the damped natural frequency (the first peak is the first mode and so on). The modal damping ratio was measured by applying the 3-dB down point concept, described in detail by Ewins [62]. Natural frequency is then calculated by knowing these two parameters; the relation is widely known in literature.

Table 2.1 compiles the modal information of all frequency response functions for a mode (peak) averaged over the measurement points. Each of the columns represents the medium in which the beam was immersed. The experimental transfer function data was interpolated using splines to increase frequency resolution, from 0.317 Hz to 0.001 Hz, allowing more precise calculation for the modal damping ratio.

Table 2.1. Average modal data and standard deviation obtained from experimental measurements.

	Natural Frequency (Hz)			Modal damping ratio ($1e^{-3}$)		
Mode	Vacuum	Air	Water	Vacuum	Air	Water
1st	14.975±0.03	15.081±0.07	9.822±0.06	19.46±2.91	19.84±1.87	34.62±1.91
2nd	93.168±0.03	93.089±0.02	61.646±0.06	3.40±0.62	4.12±0.23	7.43±0.15
3rd	259.192±0.06	259.309±0.02	173.350±0.06	1.44±0.10	1.98±0.27	3.88±0.13
4th	523.959±0.16	506.872±0.17	342.419±0.11	3.60±0.05	4.16±0.30	3.00±0.10
5th	843.019±0.02	835.955±0.33	572.432±0.47	0.65±0.02	2.88±1.11	5.20±2.24

The magnitude at each peak at each measurement point can be used to reconstruct the mode shapes. The phase information is used to define if the value is positive or negative. This procedure is described in further detail by Inman [59]. The resulting shape is finally normalized by half of the maximum displacement. Figure 2.5 presents a comparison between the measured experimental mode shapes of the beam in the three media, it also has the analytical version for further comparison.

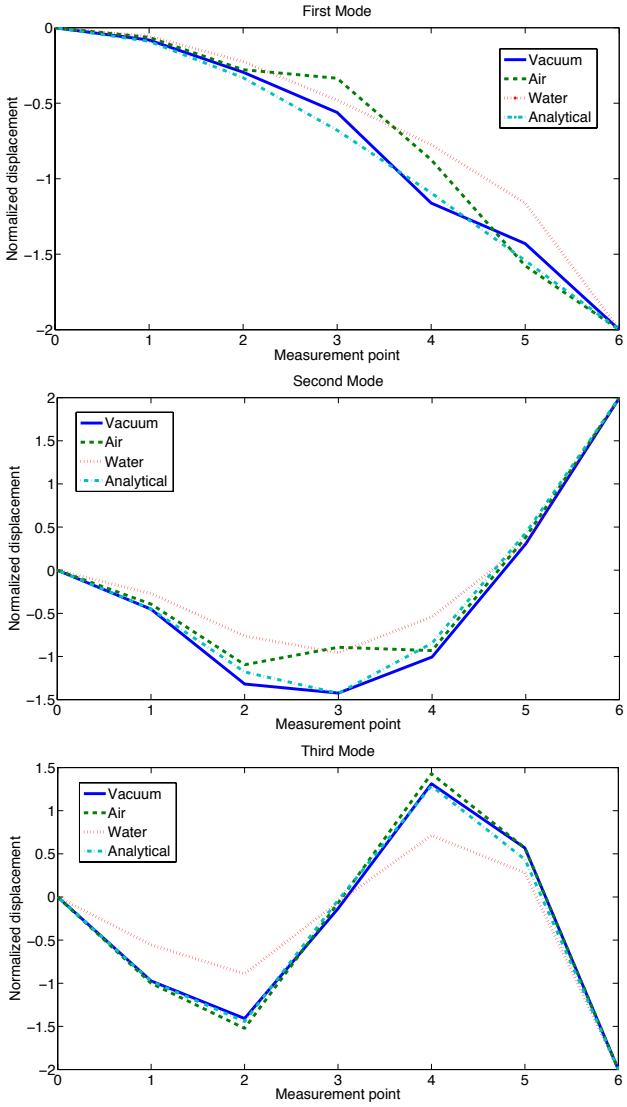

Figure 2.5. Experimental and analytical mode shapes in different media.

Equation (2.12.a) suggests a spatial and modal dependency of the damping ratio. In order to investigate that relationship, the modal damping coefficients are plotted for each measurement point. The average values (given in table 2.1) are also presented by solid lines across the plot.

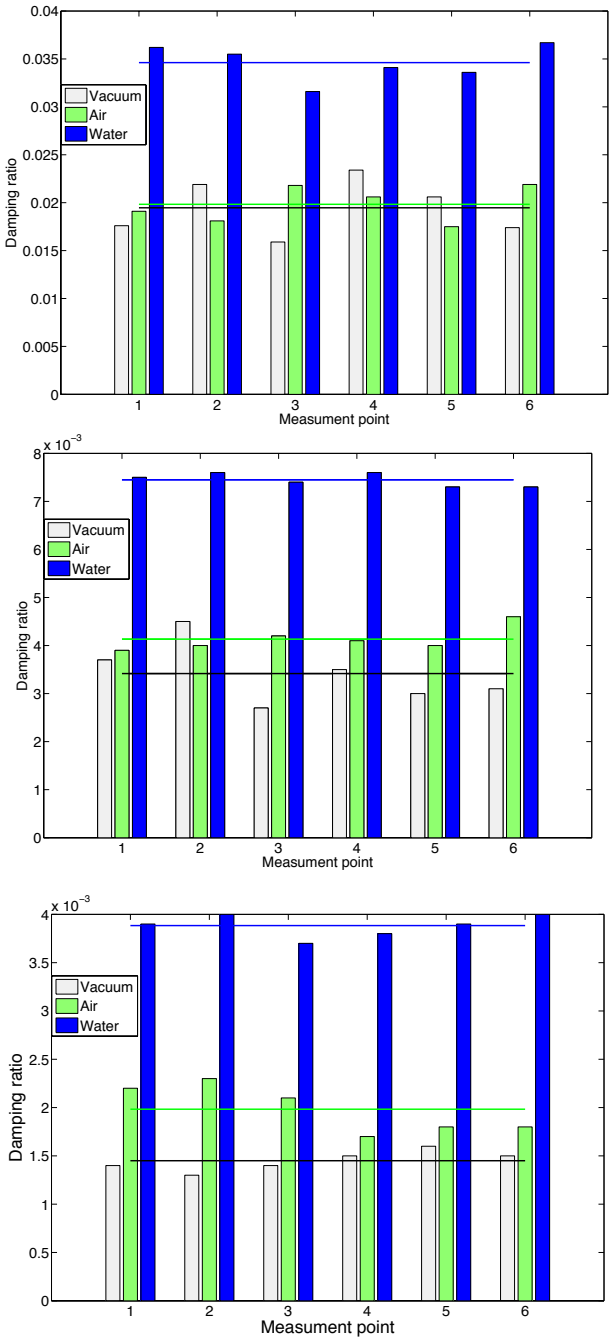

Figure 2.6. Spatial distribution of the modal damping coefficients across the cantilevered beam – top left is the first mode shape, top right is the second mode shape and bottom is the third mode shape.

By inspection of the plots there is no clear relation between the modal damping coefficients and its spatial distribution, as suggested by eq. (2.12.a). It is evident by these plots that the overall modal damping coefficient drops as mode number increases, an

expected result confirmed by experimental data. Also the relative difference between the average coefficient in different media increases as the mode number grows.

2.3.3. Discussion of experimental results

Validation of the structural model

The first step is to perform a direct comparison between the structural model prediction and experimental measurements in vacuum (fluid-less condition). One of the most important modal parameters is the natural frequency. The frequency can be calculated using eq. (2.12.b), the beam properties described in the second paragraph of the experimental section and setting the density ratio (α) to zero. Table 2.2 brings the measured and computed values side by side so a contrast could be made between the two.

Table 2.2. Vacuum natural frequency comparison between experimental and analytical.

	Vacuum (Hz)		Error
	Exp.	Analyt.	
1st	14.98	15.04	0.40%
2nd	93.17	94.27	1.18%
3rd	259.192	263.96	1.84%
4th	523.96	517.25	1.28%
5th	843.02	855.05	1.43%

It is reasonable to state at this point that the model is a good representation of the structural domain since the results of the simulation are in line with experimental data within a 2% error margin.

Statistical analysis of the modal data

To allow a correct interpretation of the values presented by table 2.1, the raw experimental data (before averaging) was treated using statistical tools. The experimental units are considered to be the points on the beam in which laser measurements were performed (see Ott and Longnecker [63] for the definition of experimental unit). Both

modal parameters are the outputs of each observation. Each experimental unit was subjected to a treatment that was a combination of vibration mode number (mode factor) and surrounding fluid (media factor); it is important to notice that the mode factor is nested within the media.

By performing an analysis of variance on the data (ANOVA) followed by a Tukey-Kramer Higher Significant Difference (HSD) comparison [63] one can isolate the effect of natural experimental variability and conclude whether the measured modal parameters are, in fact, different across fluids and mode shapes.

Such analysis was performed with the JMP® software for a confidence interval of 95%. As a result the technique indicated that natural frequencies measured in both air and vacuum for the first, second and third modes are not statistically different. All the other measured natural frequencies in table 1 are statistically different.

The analysis for modal damping ratios is more complex and is presented by table 2.3. If two mode shapes share the same letter, it means that they are not statistically different from each other. Also a letter further down the alphabet represents a smaller damping ratio then one closed to the letter A. Table 2.3 compares the measured damping values across modes in each fluid

Table 2.3. Tukey HSD comparison across mode shapes for each fluid.

Mode	Water	Mode	Air	Mode	Vacuum
1st	A	1st	A	1st	A
2nd	B	2nd	B	2nd	B
3rd	C D	3rd	C	3rd	C
4th	C	4th	B	4th	B
5th	D	5th	B C	5th	C

Table 2.3 indicates that modal damping measurements for the fourth and fifth modes are not adequate, since no clear statistical difference could be observed during the experiments independent of the surrounding fluid. The large experimental variability

observed in the damping measurements for higher modes indicates that the white noise excitation method applied is not adequate in those cases.

Experimental evaluation of the decay rate

In the proposed model the decay rate (σ) is key and can be physically interpreted as the region of fluid affected by the beam motion. By manipulating eq. (2.13) one can isolate this parameter, allowing for an experimental identification procedure based on the ratio between natural frequencies in vacuum and fluid (λ):

$$\sigma = \frac{2\alpha\lambda^2}{h(1-\lambda^2)} \tag{2.14}$$

As pointed out by the statistical analysis, there is no real measurable difference between frequencies in vacuum and air for the first modes, impeding the use of such modal data to evaluate the decay rate in air. Conversely, the data of in-water test can be used for such. Using the first five natural frequencies the decay rate determined to be on average 126.18m^{-1} (±7.15). This value could be interpreted as the inverse distance from the beam where the fluid will have 36.8% of the beam vertical velocity (approximately 8 mm from the beam in water).

Modal damping rates

The coupled model of a beam immersed in a fluid expresses the modal damping ratio as a function of spatial coordinates. Such a relationship exists to satisfy physical constrains of the problem, *i.e.* no displacement should occur at a node, and at that point the model drives the modal damping ratio to infinity as a mathematical way to guarantee such a constraint on eq. (2.7).

The spatial dependent term is composed of mode shape derivatives divided by the mode shape itself, eq. (2.12.a). In practice the model will see this ratio as a scaling factor for the fluid properties to modulate its effect in the modal damping ratio. Such practical aspects can be seen in the experimental tests, where the spatial variations of the measured modal damping ratios are not correlated to the measured mode shape and its derivatives. In fact, such measurement fluctuations presented by figure 2.6 are most likely caused by natural experimental variability.

Since the same beam was used for experiments in Newtonian fluids the modal damping increase was caused by the fluid structure interaction. Such increase is shown in figure 2.6. A simple expression to measure such effect is obtained by subtracting the vacuum modal damping ratio out of the measured modal damping ratio in air or water:

$$\zeta_{fluid} = \zeta - \zeta_{vac} \tag{2.15}$$

Table 2.4 compiles the absolute effect of the fluid in the modal damping ratio calculated based on experimental data for the first three mode shapes.

Table 2.4. Absolute effect of fluid in the modal damping ratio.

Mode	Air	Water
1st	0.0008667	0.015150
2nd	0.0007167	0.004033
3rd	0.0005333	0.002433

The absolute effect indicates that the lower modes are responsible for a higher energy transfer between domains, being the most efficient in converting the beam vibration into net fluid motion and hence propulsion. A reasonable explanation for such phenomenon is the fact that these modes have higher amplitudes, being able to displace more fluid at each cycle.

Now if one normalizes the value calculated in eq. (2.15) by the vacuum modal damping ratio coefficient, the relative fluid impact in each mode shape can be understood, as presented by figure 2.7.

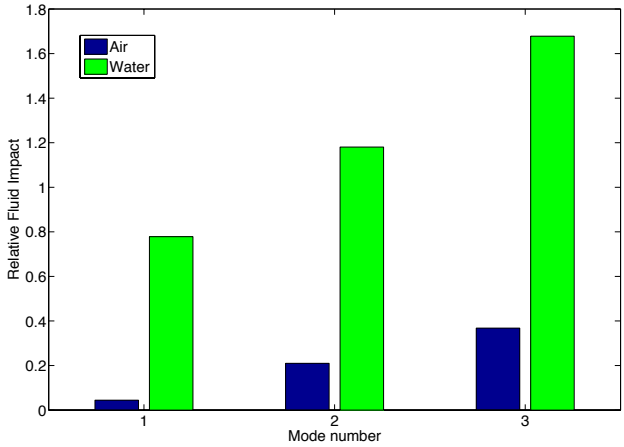

Figure 2.7. Relative fluid impact on modal damping ratios.

When the comparison of the modal damping ratio is relative to the fluid-less condition, the fluid effect is more significant for higher mode shapes. This result indicates that the fluid is more effective in changing the higher mode shapes. This characteristic can also be noticed at figure 2.5, where the mode shape distortions due to fluid-structure interaction are more evident for higher modes.

Mode shapes hypothesis

The hypothesis used while modeling the problem that the mode shapes in fluid were not affected by the fluid is not absolutely true. Experimental measurements presented by figure 2.5 pointed out slight differences between mode shapes in different media, especially when compared with the analytical mode shapes. This discrepancy is accentuated for higher modes. In an overall perspective such assumption holds for lower modes, once the changes in relative magnitude and node shifts are small compared to length scale of the beam.

The modal technique applied in this experimental test is a reasonable method for obtaining data for lower modes of vibration. By using a white noise input, the energy is spread evenly across the spectrum, revealing the most energetic (large amplitude motion) of the lower modes. Inherent to the testing technique is the poor quality of high frequency data, a fact that makes the use of such information impractical.

2.4. Thrust production – model predictions

The FSI model presented is indeed capable of capturing the most basic phenomena associated with a bio-inspired propulsor: structural flexibility, energy transfer across domains and induced flow due to the oscillations. It is important to notice that no claims are made that this approach provides a complete description to the thrust generation problem, which, for a fact, is a much more complex phenomenon that usually involves vortex sheeting and turbulent structures [50]. The assertion being made here is that even the more refined FSI models still contain the same fundamental principles captured by the proposed analytical approach and, consequently, the inferences made on the simple model can be somewhat generalized to all bio-inspired propulsor systems.

With the understanding that the model predictions are somehow limited, the thrust produced by a forced response of the vibrating beam submerged in water can be qualitatively analyzed. The use of the Galerkin's method results in a total beam displacement that is the sum of modal displacements, that is:

$$y_b(x,t) = \sum_{i=1}^{N} X_i(x) T_i(t) \tag{2.16}$$

Consequently the pressure distribution, described by eq. (2.7), will also be expressed as linear independent contribution of each mode-of-vibration:

$$\Delta P(x,t) = \sum_{i=1}^{N} \left\{ \frac{2}{\sigma} \left[\mu \left(X''_i(x) + \sigma^2 X_i(x) \right) \right] \dot{T}_i(t) - \frac{2\rho}{\sigma} X_i(x) \ddot{T}_i(t) \right\} \tag{2.17}$$

This pressure gradient acts across the beam thickness, which is normal to the surface of the structure. Figure 2.8 illustrates this distributed force acting over the beam (dF). It is important to notice that it can be decomposed into vertical (y) and horizontal (x) components.

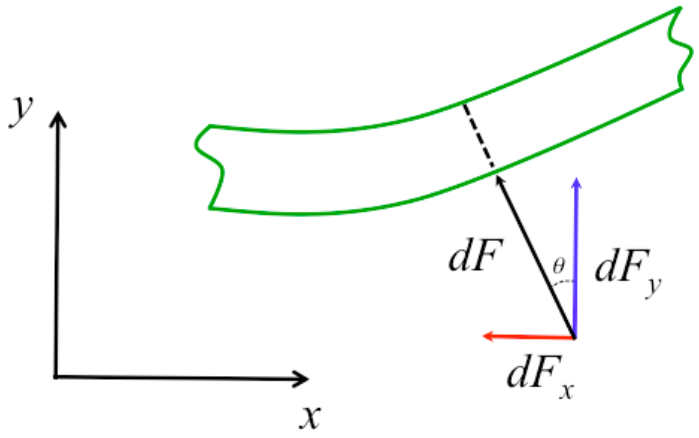

Figure 2.8. Representative beam-section under the action of a distributed force (dF), which is caused by an external pressure gradient (ΔP) due to the surrounding fluid.

Mathematically the force is described and decomposed into the following:

$$dF = w \ \Delta P \tag{2.18}$$

$$dF_y = dF \cos\theta \cong dF \tag{2.19.a}$$

$$dF_x = dF \sin\theta \cong dF\theta = dF \frac{\partial y_b}{\partial x} \tag{2.19.b}$$

These differential forces in each direction can be integrated over the beam length in order to compute an effective force being applied to the entire structure. The lift can be defined as the sum of forces in the *y* direction:

$$L(t) = \int_0^L \Delta P(x,t)\ w\ dx \tag{2.20}$$

The integral of the force component in the *x* direction is defined as the thrust produced by (or applied in) the structure:

$$T(t) = \int_0^L \Delta P(x,t)\ w\ \frac{\partial y_b}{\partial x} dx \tag{2.21}$$

To further investigate the propulsion capabilities of the model proposed a harmonic forcing function was chosen to represent a possible actuation on such a systems. This input was defined to be a sinusoidal force of frequency f and amplitude A_s applied at the beam tip (represented by the Dirac delta function, δ).

$$\mathrm{f}(x,t) = \delta(x-L)A_s \sin(2\pi ft) \tag{2.22}$$

Figure 2.9 corresponds to the thrust and lift produced by a beam, with the same dimensions as the one used during experiments, under the excitation described by eq. (2.22). The surrounded fluid was chosen to be water and the decay rate is the one calculated experimentally for that media. Appendix B describes in further detail the equations being solved in order to simulate this FSI behavior.

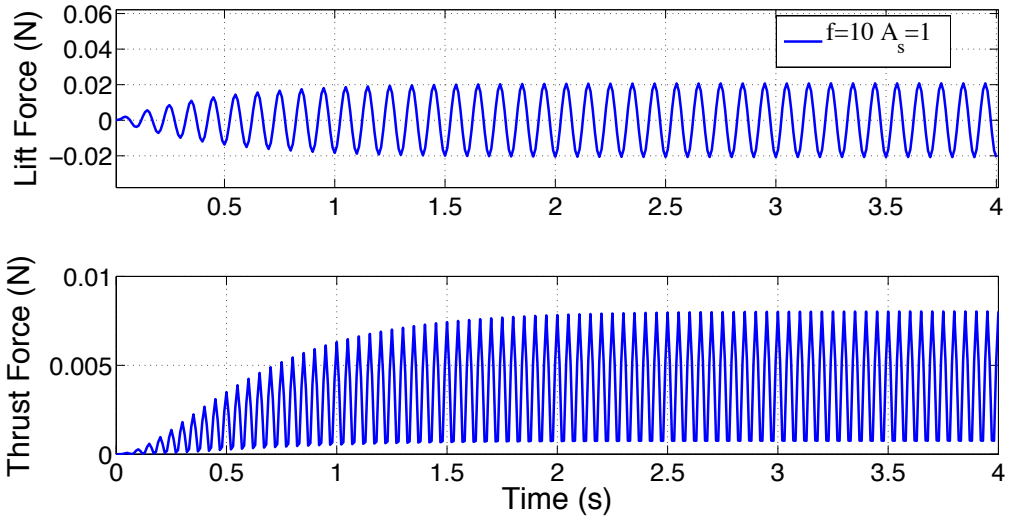

Figure 2.9. Thrust and lift forces acting on the submersed vibrating beam with a 10Hz sinusoidal input at the tip (A_s=1).

Notice that while the lift has an approximate zero mean the thrust has an average component. It is also clear the oscillatory nature of the propulsion process with the thrust period being half of the lift one. For this single forced oscillator three input characteristics (*i.e.* control variables) that can be changed: where the force is being applied (position x), frequency (f) and amplitude (A_s).

The position where the force is being applied can significantly improve the performance of the system, but actively changing its position during operation requires a complex system with distributed actuators. Thus this control parameter will be considered a project-specific characteristic and will not be treated as a variable in this analysis. On the other hand frequency and amplitude are easily tunable and will be the main object of investigation. Figure 2.10 compiles a series of simulations of the average, steady-state thrust generation for problem being simulated under a wide range of input frequencies (f) and three different input amplitudes.

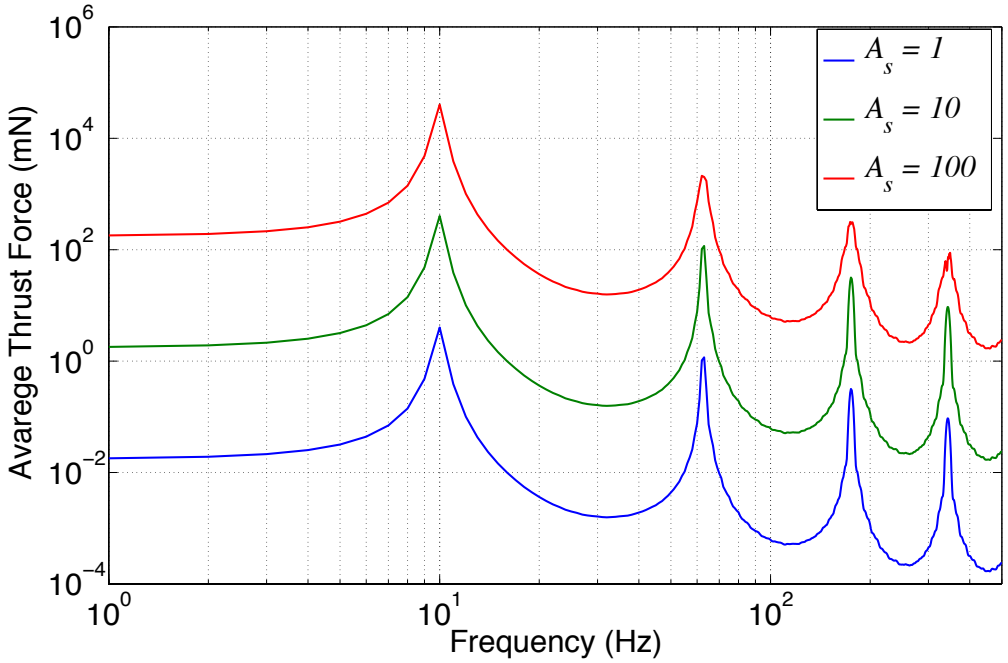

Figure 2.10. Steady-state average thrust force created by each actuation frequency for three different sinusoidal amplitudes (A_s).

The peaks in thrust production in figure 2.10 coincide with the natural frequencies of the coupled system previously presented by table 2.1. For all the different input

amplitudes the maximum thrust was produced at the first natural frequency (9.82 Hz). The average magnitude is also scaling with the square of the input amplitude.

2.5. Choosing amplitude as the control variable

Based on the simulation results of the actively vibrating submersed beam (figure 2.10) some inferences can be made when it comes to the variable being used to control the thrust generation. Choosing the amplitude as the control variable and setting f to the first natural frequency gives the system large capabilities when it comes to thrust force range. It is also interesting from a controller designer perspective that the average thrust scales with the square of the input amplitude a trivial relationship that simplifies the control law.

The increase in thrust production at the first natural frequency is a product of the resonance phenomenon that occurs at that frequency. This constructive interference maximizes structural motion and consequent downstream fluid displacement, which directly results in more thrust being produced. Exploring this resonant condition could significantly improve the overall system performance.

The question then becomes if resonance is also a fundamental characteristic of an arbitrary bio-inspired underwater propulsor. The answer relies in two distinct steps, first provide the mathematical condition/fundaments that allows resonance in an arbitrary system and second evaluate if these conditions are met by an arbitrary bio-inspired propulsor. If it is proven that resonance is indeed a fundamental part of a generic BIAUV system then the conclusions drawn to FSI model presented in this chapter can be extended to all similar systems.

Kartashova [30] define on her book that an arbitrary partial differential equation (PDE) that has (physically) a wave-like solution and which time and space coordinates can be treated separately is called an evolutionary dispersive PDE. The dispersion function is a real-valued function of the wave-number ($\mathbf{k}_i$) that relates to the wave-frequency (ω) of a wave-like solution and its second derivative with respect to the wave-number is different then zero.

Notice that no restriction has been made whether the PDE is linear or nonlinear. It is considered that the system described above is under the influence of a number of

external wave-like disturbances. Finally the resonance condition for a *s*-wave processes, with *s* being less then infinity, read as [30]:

$$\omega(\mathbf{k}_1) \pm \omega(\mathbf{k}_2) \pm \cdots \pm \omega(\mathbf{k}_s) = 0 \tag{2.23.a}$$

$$\mathbf{k}_1 \pm \mathbf{k}_2 \pm \cdots \pm \mathbf{k}_s = 0 \tag{2.23.b}$$

Although the condition (2.23) seems complex it has quite an intuitive interpretation, for the resonance to occur the excitation has to match both the frequency and the shape of the wave-like solution of the PDE being excited.

This approach is quite useful in the context of this research because it guarantees the existence of some form of resonance as long as the physical system have travelling waves as an intrinsic part of their fundamental behavior. There is no need to have prior knowledge of the linearity/nonlinearity of the system to guarantee resonant behavior it is only required that the dispersion function second derivative is different then zero (to eliminate first order systems responses).

Now that we have the necessary mathematical tools to analyze the bio-inspired propulsion systems lets inspect both components of the problem (structure and fluid). The flexible nature of the structure by itself presents the reasoning of why wave-like behaviors can easily represent the motion of the system. For the fluid side wave-like solutions/responses are also intuitive expression of fluid motion for low Reynolds number (before the beginning of the transition to turbulence), *e.g.* vortex shedding.

In other words, it is a fundamental characteristic of bio-inspired propulsor to resonate both in the structural and the fluid domains. Making use of this constructive interference process reduces the amount of input energy necessary to achieve a desired thrust production level thus increasing the overall system efficiency. In order to operate on such condition the actuation frequency has to match the FSI natural frequency as demonstrated by the proposed modeling approach. As a result the amplitude of the input is a good choice of control input parameter to maximize the efficiency in thrust production.

3. Sliding Mode Control

The fundamental control architecture utilized throughout this dissertation is a combination of a model-based controller design, with the feedback and an input command channel, as illustrated by figure 1.4. As discussed in the first chapter of this dissertation, closed-loop (feedback) control architecture is indeed a requirement to improve the overall systems robustness in the operation of bio-inspired autonomous underwater vehicles (BIAUV). The command input is also a prerequisite since the vehicle autonomy demands that high-level decisions alter the execution control set point.

The model-based controller design approach provides insight into the system behavior a priori and requires a great knowledge from the operator of the system that is provided by a mathematical model. Consequently this approach reduces the computation requirements on the onboard electronics when it comes to this decision-making process. However, a precise modeling of the dynamic behavior of BIAUV can be a challenging task, thus requiring a tradeoff between model precision and simplicity from the designer. A minimalistic model approach usually leads to a very useful prediction tool that can be tuned to adequately represent a set of experimental data, *i.e.* a problem with a known structure but with uncertain coefficients. Choosing an appropriate controller design tool that can deal with these structured uncertainties in the model is key to successfully achieve a model based control law.

Sliding mode control (SMC) is a nonlinear, model-based controller design technique that is fundamentally characterized by its robustness, *i.e.* capabilities to compensate for structured uncertainties on the model utilized to represent the physical system. This latter characteristic of the resulting control law is the main reasoning to apply the SMC design methodology to autonomous underwater vehicles (AUVs). However the need to utilize a reliable mathematical model of the system is also a very useful outcome of the procedure.

This chapter is organized as follows: The first section is a literature review of the sliding mode controller theory and design process. Section 3.2 provides the general concepts behind sliding mode controller design for nonlinear systems, both for continuous and discrete systems. In section 3.3 the controller designs are revisited to

provide robustness to structured uncertainties and disturbances in the feedback law. The last section applies the proposed method to a benchmark example to illustrate the method.

3.1. Literature review on sliding mode controllers

The study of ordinary differential equations with discontinuous right-hand-side by Fillipov [37] provides the theoretical foundation for the development of variable structure systems (VSS). These systems are characterized by large qualitative changes of its phase portrait when submitted to different types of input, *i.e.* the structure of the system changes based on the input characteristic [64]. Figure 3.1 illustrates this concept.

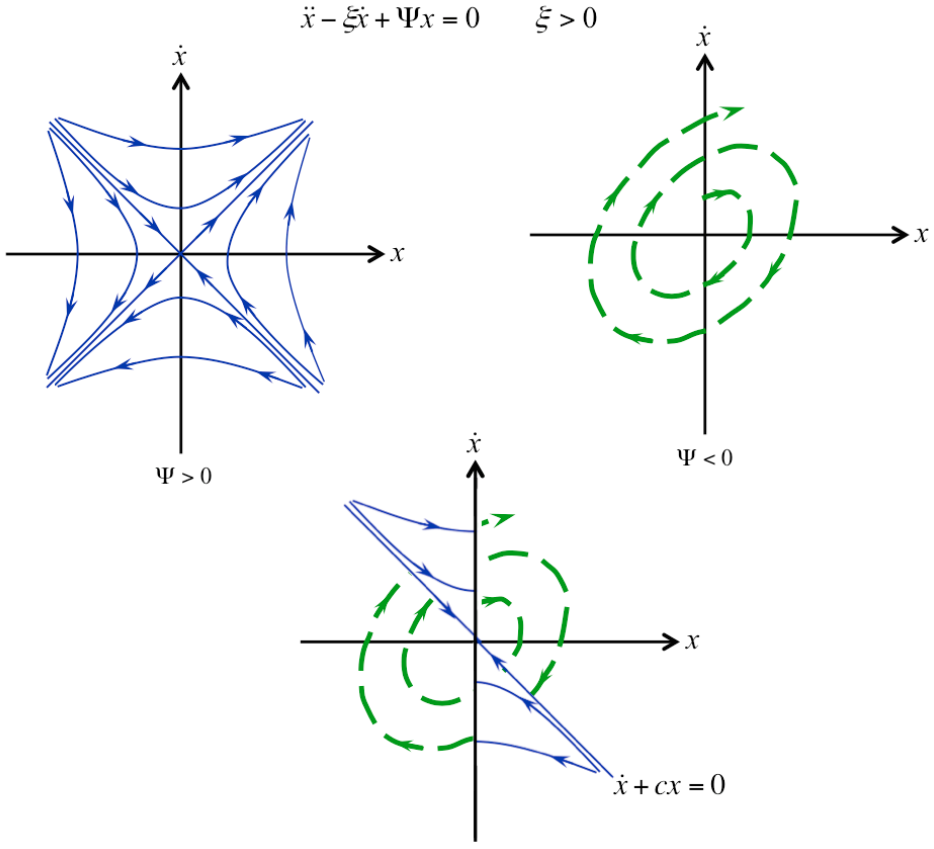

Figure 3.1. General idea behind VSS, based on [64]. The second order system described by the equation in the top of the figure has a tunable (Ψ) gain and a fixed (ξ) parameter. The top plots represent the system behavior under different gain structures (positive and negative gains). Although both overall behaviors are unstable, they can be combined in

such a way that the overall system becomes stable. The bottom plot illustrates one possible combination of structures to stabilize the system.

The use of variable structure properties as a means to control the system itself can be quite intuitive and has been developed since the 50's [65]. VSS also has mathematical applications [66]. One of the most important VSS characteristics explored is that an asymptotically stable system can be obtained from an arrangement of unstable systems [64], as illustrated in figure 3.1. In control applications of this property is very useful and desirable due to its robustness to uncertainties and disturbances. Sliding mode controller (SMC), also known as variable structure controller (VSC), is the use of VSS theory as a design tool to create a feedback control law that stabilizes a continuous dynamic system. The overall idea behind this design method is to use different input structures to attract the state to an asymptotically stable hyperplane, also called switching surface or sliding manifold. Once, the stable hyperplane has been reached the state "slides" asymptotically to the equilibrium point over that manifold.

The SMC operates in three different modes: reaching (RM), sliding (SM) and steady state (SS). When the current state is not on a desired sliding surface, the reaching mode creates a force to drive the current state to the desired sliding surface. If the state was successfully driven to the switching surface the sliding mode takes over and pushes the state along the sliding manifold until the equilibrium point is reached. Finally the steady-state mode is activated keeping the system at its equilibrium. Figure 3.2 illustrates these three main operating modes of the SMC for a second order system.

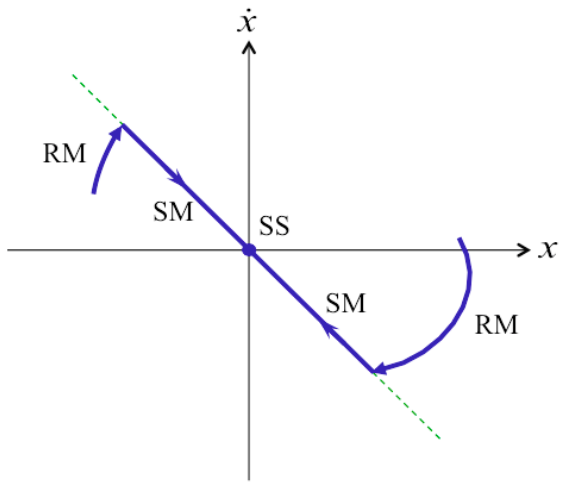

Figure 3.2. Operating modes of the SMC.

There are two design challenges in implementing a SMC. The first is related to finding an appropriate sliding manifold and the second defining appropriate structures to attract the state to the stable hyperplane. The behavior of the system while it is on the sliding mode is just a function of the hyperplane itself. This invariance with respect to model parameters and disturbances is of extreme importance when controller robustness is required. Initially a SMC design technique was developed only for continuous-time linear systems [67][68] and later it was also expanded for continuous-time nonlinear systems [69][70][71]. In practical applications, the use of a discontinuous control function in the presence of model uncertainties leads to chattering around the sliding manifold, a phenomenon that could lead to high frequency excitation of the physical system. Slotine [69] introduced the concept of a switching surface boundary layer to address the chattering issue. This feature can be understood as a smoothing of the transition between different control structures.

Following the advances in the Lyapunov stability theory, a "standard" method for designing the robust SMC for continuous-time systems has been investigated in literature [71] [32] [72], referred to here as Analog Sliding Mode Controller or ASMC. Prior publications have applied this technique to applications such as controlling satellite attitude [73], chemical reactions [74], underwater vehicles [20], and various others

[75][76][77]. The ASMC has also been extensively applied in the design of state observers for a large group of systems [78][79].

In the 80's, the use of microprocessors as a means of implementing a control law introduced a new relevant effect: the discretization/sampling process [80]. Although authors understood the fundamental difference between the analog and discrete/digital control of a system, they still relied on the robustness of the method to discretely apply the ASMC laws [69][80]. The initial steps toward realizing a discrete/digital sliding mode control (DSMC) were developed by Milosavljevic [81]. It was found that reaching the sliding manifold with a discrete control action was not practical and thus the theory was extended to a quasi-sliding mode concept [81]. A similar concept was also applied to the SS mode resulting in the quasi-steady state mode.

Other studies in literature have developed the DSMC technique for discrete linear systems using different constraints in the controller design to guarantee that the overall system would reach the quasi-sliding mode of operation [82][83][84]. Gao *et al.* [84] have defined three desired attributes for the DSMC as listed here: crossing of the switching surface in a finite time; after crossing the sliding manifold for the first time the state would have to cross it again at each successive time step (zigzag motion); and non-increasing step of the zigzag motion, *i.e.* trajectory must stay within a specified band. It is important to notice that these attributes are not a necessary condition for the stability of a discrete linear system. Su *et al.* [85] reduced the oscillation band size of the quasi-sliding mode by using previous state information to predict disturbances. Zheng *et al.* [86] applied the linear theory of DSMC to a nonlinear system by representing it in terms of Takagi-Sugeno fuzzy model, *i.e.* a weighted sum of local linear models.

Starting from the work developed by Sarpturk *et al.* [82], Sira-Ramirez [87] expanded the DSMC concept from linear to nonlinear systems, providing sufficient and necessary conditions for reaching and existence of quasi-sliding modes. Although the conclusions presented here agrees with the findings of Sira-Ramirez [87] the existence and reaching of a quasi-sliding manifold is guaranteed by a Lyapunov-type of a discrete functional condition (similar to Furuta [83]). Another important contribution presented here is the inclusion of the Taylor-Lie discretization effects [88] on the controller design and stability analysis of a nonlinear system.

3.2. Sliding mode controller design

Consider an autonomous nonlinear system, written in the regular/canonical form:

$$\begin{aligned} \dot{\boldsymbol{\eta}} &= \boldsymbol{f}(\boldsymbol{\eta},\boldsymbol{\xi}) \\ \dot{\boldsymbol{\xi}} &= \boldsymbol{f}_a(\boldsymbol{\eta},\boldsymbol{\xi}) + \boldsymbol{G}_a(\boldsymbol{\eta},\boldsymbol{\xi})\mathbf{u} \end{aligned} \tag{3.1}$$

where $\boldsymbol{\eta}$ and $\boldsymbol{\xi}$ are the state vectors, $\boldsymbol{f}$ and $\boldsymbol{f}_a$ are vector fields representing the system's dynamics, $\mathbf{u}$ is the input vector and $\boldsymbol{G}_a$ is the input matrix. Without loss of generality the system (3.1) is also said to have an equilibrium at the origin, *i.e.* $\mathbf{x}_e = [\boldsymbol{\eta},\boldsymbol{\xi}]^T = [\mathbf{0},\mathbf{0}]^T$.

The dynamic system described by equation (3.1) is a generic representation of several physical models and will be referred throughout this chapter as the system to be controlled. The following subsections will describe the design of an ASMC (the conventional technique), the discretization of the nonlinear system using Taylor-Lie derivatives and finally the design of a DSMC.

3.2.1. Analog (continuous-time) sliding mode controller design

The design of a sliding mode controller is a two-step process, where, first, a stable sliding manifold has to be chosen and, second, the different control structures have to be defined. For a regular form system, such as (3.1), the $\boldsymbol{\xi}$ trajectory that asymptotically stabilizes the $\boldsymbol{\eta}$ dynamics is a possible choice of a sliding manifold. Asymptotical stability can be guaranteed using Lyapunov stability theory. A common approach in literature [32] is to define a quadratic Lyapunov function (V_1) for the $\boldsymbol{\eta}$-state and choose a $\boldsymbol{\xi}$-trajectory, $\boldsymbol{\xi}=\boldsymbol{\phi}(\boldsymbol{\eta})$, which imposes a strict negative rate on the Lyapunov function:

$$\begin{aligned} \mathrm{V}_\eta &= \frac{1}{2}\boldsymbol{\eta}^T\boldsymbol{\eta} \\ \dot{\mathrm{V}}_\eta &= \boldsymbol{\eta}^T\dot{\boldsymbol{\eta}} = \boldsymbol{\eta}^T\boldsymbol{f}(\boldsymbol{\eta},\boldsymbol{\phi}(\boldsymbol{\eta})) < 0 \end{aligned} \tag{3.2}$$

The hyperplane, $\boldsymbol{\xi}=\boldsymbol{\phi}(\boldsymbol{\eta})$, also has to satisfy the equilibrium point at the origin, *i.e.* $\boldsymbol{\phi}(\mathbf{0})=\mathbf{0}$. A simple linear coordinate transformation can be defined to verify if the $\boldsymbol{\xi}$-trajectory designed is being achieved or not, this new variable is called the reaching state:

$$\mathbf{s} = \boldsymbol{\xi} - \boldsymbol{\phi}(\boldsymbol{\eta}) \tag{3.3}$$

It is obvious that the origin of the reaching state ($\mathbf{s}=\mathbf{0}$) is the sliding manifold. If the dynamic system is on this hyperplane it is said to be on the sliding mode of operation.

To drive the system (3.1), in finite time, from any reaching state to the origin it is necessary to investigate the time-derivative of this new state:

$$\dot{\mathbf{s}} = \dot{\boldsymbol{\xi}} - \dot{\boldsymbol{\phi}}(\boldsymbol{\eta}) = \boldsymbol{f}_a(\boldsymbol{\eta},\boldsymbol{\xi}) + \boldsymbol{G}_a(\boldsymbol{\eta},\boldsymbol{\xi})\mathbf{u} - \frac{\partial \boldsymbol{\phi}}{\partial \boldsymbol{\eta}} \boldsymbol{f}(\boldsymbol{\eta},\boldsymbol{\xi}) \tag{3.4}$$

An intuitive choice of feedback law is to cancel all the dynamics from equation (3.4), a solution that guaranties the existence of the sliding mode if **s**=**0** but does not guarantee reaching. An alternative is to add an attractor term (**v**) to the feedback law:

$$\mathbf{u} = \boldsymbol{G}_a^{-1}(\boldsymbol{\eta},\boldsymbol{\xi})\left[-\boldsymbol{f}_a(\boldsymbol{\eta},\boldsymbol{\xi}) + \frac{\partial \boldsymbol{\phi}}{\partial \boldsymbol{\eta}} \boldsymbol{f}(\boldsymbol{\eta},\boldsymbol{\xi}) + \mathbf{v}\right] \tag{3.5}$$

where the superscript -1 indicates the inverse. It is of great importance for the application of the control law that such inverse exists.

The resulting reaching state dynamics is simply **v**. The attractor term can be chosen as a constant positive value (b_0) with the opposite signal of the reaching state, this choice monotonically drags the reaching state to its origin (proof C.1):

$$\mathbf{v} = -b_0 sign\left(\boldsymbol{\xi} - \boldsymbol{\phi}\right) \tag{3.6}$$

where *sign* is the Signum function.

Equation (3.6) is the choice of control structures to be implemented. It switches from a constant positive number to a negative one when the sliding manifold is crossed (from negative reaching state side to positive) and vice-versa.

3.2.2. Discretization of a nonlinear system using Taylor-Lie series

The digital implementation of control laws has several advantages when compared to analog laws, such as: noise rejection, high reliability and low overall cost [38]. All these advantages come with the addition of a sampling apparatus, which transform the continuous-time states of the dynamic system into a set of discrete values. Figure 1.5 illustrates the data sampling procedure from a continuous-time dynamic system and the resulting discrete dynamic system.

The system presented by equation (3.1) can be discretized expanded using Taylor series under the ZOH (zero-order hold) assumption:

$$\begin{aligned}\boldsymbol{\eta}^{k+1} &= \boldsymbol{\eta}^{k} + \sum_{\ell=1}^{\infty} \left.\frac{\partial^{\ell}\boldsymbol{\eta}}{\partial t^{\ell}}\right|_{k} \frac{T_s^{\ell}}{\ell!} \\ \boldsymbol{\xi}^{k+1} &= \boldsymbol{\xi}^{k} + \sum_{\ell=1}^{\infty} \left.\frac{\partial^{\ell}\boldsymbol{\xi}}{\partial t^{\ell}}\right|_{k} \frac{T_s^{\ell}}{\ell!}\end{aligned} \tag{3.7}$$

where the superscript k indicates that it is the property at the k^{th} time step. The next step is to convert the l order time-derivatives using Lie derivatives:

$$\begin{aligned}\boldsymbol{\eta}^{k+1} &= \eta^{k} + \boldsymbol{f}^{k} T_s + \sum_{\ell=2}^{\infty} L_{f^k}^{\ell-1}\left(\boldsymbol{f}^{k}\right)\frac{T_s^{\ell}}{\ell!} \\ \xi^{k+1} &= \xi^{k} + \left(\boldsymbol{f}_a^{k} + \boldsymbol{G}_a^{k}\mathbf{u}^{k}\right)T_s + \sum_{\ell=2}^{\infty} L_{\boldsymbol{f}_a^k + \boldsymbol{G}_a^k\mathbf{u}^k}^{\ell-1}\left(\boldsymbol{f}_a^{k} + \boldsymbol{G}_a^{k}\mathbf{u}^{k}\right)\frac{T_s^{\ell}}{\ell!}\end{aligned} \tag{3.8}$$

where $L^{l}_{\mathbf{g}}\mathbf{h}$ is the Lie derivative operator and it describes the flow of a vector (**h**) on a vector field (**g**). The superscript l indicates the number of nested operations, in other words, the Lie derivative operation of the resulting vector of a previous operation, l times.

The application of these two operations to the dynamics systems is known as Taylor-Lie series [88]. It is not possible to implement an infinite series into discrete processing devices. A usual approach to overcome this limitation is to truncate the series at a number of elements (N), resulting in an approximate discretized model:

$$\begin{aligned}\boldsymbol{\eta}^{k+1} &= \eta^{k} + \boldsymbol{f}^{k} T_s + \sum_{\ell=2}^{N} L_{f^k}^{\ell-1}\left(\boldsymbol{f}^{k}\right)\frac{T_s^{\ell}}{\ell!} \\ \xi^{k+1} &= \xi^{k} + \left(\boldsymbol{f}_a^{k} + \boldsymbol{G}_a^{k}\mathbf{u}^{k}\right)T_s + \sum_{\ell=2}^{N} L_{\boldsymbol{f}_a^k + \boldsymbol{G}_a^k\mathbf{u}^k}^{\ell-1}\left(\boldsymbol{f}_a^{k} + \boldsymbol{G}_a^{k}\mathbf{u}^{k}\right)\frac{T_s^{\ell}}{\ell!}\end{aligned} \tag{3.9}$$

It is important to mention that N and T_s have to be appropriately selected in order to capture all the relevant continuous system dynamics. After rearranging all terms and grouping, one can write the discrete dynamics for the system in the following form:

$$\begin{aligned}\boldsymbol{\eta}^{k+1} &= \eta^{k} + \boldsymbol{f}^{D}(\eta^{k}, \xi^{k}, T_s) \\ \xi^{k+1} &= \xi^{k} + \boldsymbol{f}_a^{D}(\eta^{k}, \xi^{k}, T_s) + \boldsymbol{H}^{D}(\eta^{k}, \xi^{k}, T_s, \mathbf{u}^{k})\end{aligned} \tag{3.10}$$

where the discrete vector fields are identified by the superscript D and are described as:

$$
\begin{aligned}
\boldsymbol{f}^D(\eta^k,\xi^k,T_s) &= T_s\boldsymbol{f}^k + \sum_{\ell=2}^{N} L_f^{\ell-1}\boldsymbol{f}\frac{T_s^\ell}{\ell!} \\
\boldsymbol{f}_a^D(\eta^k,\xi^k,T_s) &= T_s\boldsymbol{f}_a^k + \sum_{\ell=2}^{N} L_{f_a^k}^{\ell-1}\boldsymbol{f}_a^k\frac{T_s^\ell}{\ell!} \\
\mathbf{H}^D(\eta^k,\xi^k,\mathbf{u}^k,T_s) &= T_s\boldsymbol{G}_a^k\mathbf{u}^k + \sum_{\ell=2}^{N}\left[L_{\boldsymbol{G}_a^k\mathbf{u}^k}^{\ell-1}\left(\boldsymbol{f}_a^k+\boldsymbol{G}_a^k\mathbf{u}^k\right)+L_{f_a^k}^{\ell-1}\left(\boldsymbol{G}_a^k\mathbf{u}^k\right)\right]\frac{T_s^\ell}{\ell!}
\end{aligned}
\tag{3.11}
$$

A useful simplification is to assume that the input matrix ($\boldsymbol{G}_a$) is independent of the ξ–state; this property will allow significant simplification on the discrete input term ($\mathbf{H}^D$):

$$
\begin{aligned}
\eta^{k+1} &= \eta^k + \boldsymbol{f}^D(\eta^k,\xi^k,T_s) \\
\xi^{k+1} &= \xi^k + \boldsymbol{f}_a^D(\eta^k,\xi^k,T_s) + \boldsymbol{G}_a^D(\eta^k,T_s)\mathbf{u}^k
\end{aligned}
\tag{3.12}
$$

where:

$$
\boldsymbol{G}_a^D(\eta^k,T_s) = T_s\boldsymbol{G}_a^k + \sum_{\ell=2}^{\infty} L_{\boldsymbol{G}_a^k}^{\ell-1}\boldsymbol{f}_a^k\frac{T_s^\ell}{\ell!} \tag{3.13}
$$

The approximate representation of the continuous-time model as an appropriate set of difference equations (equations 3.11, 3.12 and 3.13) is a necessary step in order to define the digital sliding mode controller. This discretization process and rearrangement has not previously been presented in the literature.

3.2.3. Digital (discrete-time) sliding mode controller design

Although the discrete system being considered in this subsection, eq. (3.12), is quite similar to the continuous system, eq. (3.1), the design of a sliding mode controller is different. The distinction is because a difference equation is describing the system behavior instead of a differential equation. The two-step design process is analogous for the discrete system, first design a sliding manifold and then define the control structure. The main difference is in the technique used to guarantee both the existence and reachability of the stable hyperplane. The concept proposed by Furuta [83] for linear systems is extended for nonlinear systems, where a Lyapunov-type of function is defined and the difference between future and current value of the function has to be negative (proof C.2):

$$V_\eta^k = \left(\boldsymbol{\eta}^k\right)^T \boldsymbol{\eta}^k$$
$$V_\eta^{k+1} - V_\eta^k < 0 \tag{3.14}$$

The condition (3.14) is sufficient to guarantee the existence of a sliding manifold and it has not been presented previously in literature for a multivariable nonlinear system. The proof of such is given in appendix C.2, which also can be expressed as the following inequality, assuming that $\boldsymbol{\xi}^k = \boldsymbol{\phi}^k$ (proof C.2):

$$\boldsymbol{f}^D(\boldsymbol{\eta}^k, \boldsymbol{\phi}^k(\boldsymbol{\eta}^k), T_s)^T \left[2\boldsymbol{\eta}^k + \boldsymbol{f}^D(\boldsymbol{\eta}^k, \boldsymbol{\phi}^k(\boldsymbol{\eta}^k), T_s)\right] < 0 \tag{3.15}$$

In order for condition (15) to be true the discrete $\boldsymbol{\eta}^k$ dynamics ($\boldsymbol{f}^D$) has to negative and its magnitude must be smaller then $2\boldsymbol{\eta}^k$. This latter constrain corresponds to a magnitude upper bound restriction, an inexistent limitation in the ASMC design process but a requirement for the DSMC being proposed here. A definition of a discrete reaching state is also necessary in order to activate each control structure and consequently attract the system to the stable hyperplane:

$$\mathbf{s}^k = \boldsymbol{\xi}^k - \boldsymbol{\phi}^k(\boldsymbol{\eta}^k, T_s) \tag{3.16}$$

The future step (k+1) of the discrete reaching state is easily defined:

$$\mathbf{s}^{k+1} = \boldsymbol{\xi}^{k+1} - \boldsymbol{\phi}^{k+1}(\boldsymbol{\eta}^{k+1}, T_s) = \boldsymbol{\xi}^k + \boldsymbol{f}_a^D(\boldsymbol{\eta}^k, \boldsymbol{\xi}^k) + \boldsymbol{G}_a^D(\boldsymbol{\eta}^k, T_s)\mathbf{u}^k - \boldsymbol{\phi}^{k+1}(\boldsymbol{\eta}^k + \boldsymbol{f}(\boldsymbol{\eta}^k, \boldsymbol{\xi}^k), T_s) \tag{3.17}$$

Similar to the procedure done for continuous systems an adequate choice of feedback input that cancels all the terms on equation (3.17) and introduces an attractor term ($\mathbf{v}^k$) to the reaching dynamics, is:

$$\mathbf{u}^k = \boldsymbol{G}_a^D(\boldsymbol{\eta}^k, T_s)^{-1}\left[-\boldsymbol{f}_a^D(\boldsymbol{\eta}^k, \boldsymbol{\xi}^k, T_s) - \boldsymbol{\phi}^k(\boldsymbol{\eta}^k, T_s) + \boldsymbol{\phi}^{k+1}(\boldsymbol{\eta}^k + \boldsymbol{f}(\boldsymbol{\eta}^k, \boldsymbol{\xi}^k), T_s) + \mathbf{v}^k\right] \tag{3.18}$$

Once again the existence of the inverse of the discrete input matrix ($\boldsymbol{G}_a^D$) for all states is key for the existence of a control law. The resulting future reaching state is a sum of the previous state ($\mathbf{s}^k$) plus $\mathbf{v}^k$. To drag the reaching state to its origin one can choose the following form for the discrete attractor term (proof C.3):

$$\mathbf{v}^k = -b_0\left[\boldsymbol{\xi}^k - \boldsymbol{\phi}^k(\boldsymbol{\eta}^k, T_s)\right] \tag{3.19}$$

where b_0 is strictly positive real value from in following interval (0,2). The fact that the attractor term has an upper limit is a necessary constrain to avoid over actuation during the sampling period T_s. The mathematical reasoning behind this value is given in proof C.3.

Comparing the proposed DSMC law (equations 3.18 and 3.19) to the traditional ASMC (equations 3.5 and 3.6) the difference between the two approaches is clear. Not only the format of the equations are different but they fundamentally differ in the attractor term. While the analog attractor can have a constant magnitude the discrete one has to be proportional to $\mathbf{s}^k$.

3.3. Robustness considerations

Equation (3.1) can be modified to accommodate structured uncertainties. Such action would allow taking them into account on the controller design even though they are not precisely known:

$$\begin{aligned}\dot{\boldsymbol{\eta}} &= \boldsymbol{f}(\boldsymbol{\eta},\boldsymbol{\xi}) + \delta_{\boldsymbol{\eta}}(\boldsymbol{\eta},\boldsymbol{\xi}) \\ \dot{\boldsymbol{\xi}} &= \boldsymbol{f}_a(\boldsymbol{\eta},\boldsymbol{\xi}) + \boldsymbol{G}_a(\boldsymbol{\eta},\boldsymbol{\xi})\left[\mathbf{u} + \delta_{\boldsymbol{\xi}}(\boldsymbol{\eta},\boldsymbol{\xi},\mathbf{u})\right]\end{aligned} \tag{3.20}$$

where $\boldsymbol{\delta}$ represents a structured uncertainty, *e.g.* model parameter error or input disturbances, that could be present in either the $\boldsymbol{\eta}$ or $\boldsymbol{\xi}$ dynamics.

Also for discrete systems the uncertainties can be incorporated in the difference equations. By following the exact same procedure described in the subsection 3.2, equation (3.12) will become the following under the presence of uncertainties:

$$\begin{aligned}\boldsymbol{\eta}^{k+1} &= \boldsymbol{\eta}^k + \boldsymbol{f}^D(\boldsymbol{\eta}^k,\boldsymbol{\xi}^k,T_s) + \boldsymbol{\delta}_{\boldsymbol{\eta}}^D(\boldsymbol{\eta}^k,\boldsymbol{\xi}^k,T_s) \\ \boldsymbol{\xi}^{k+1} &= \boldsymbol{\xi}^k + \boldsymbol{f}_a^D(\boldsymbol{\eta}^k,\boldsymbol{\xi}^k,T_s) + \boldsymbol{G}_a^D(\boldsymbol{\eta}^k,T_s)\left[\mathbf{u}^k + \boldsymbol{\delta}_{\boldsymbol{\xi}}^k(\boldsymbol{\eta}^k,\boldsymbol{\xi}^k,\mathbf{u}^k)\right] + \boldsymbol{\delta}^D(\boldsymbol{\eta}^k,\boldsymbol{\xi}^k,\mathbf{u}^k,T_s)\end{aligned} \tag{3.21}$$

where:

$$\begin{aligned}\boldsymbol{\delta}_{\boldsymbol{\eta}}^D(\boldsymbol{\eta}^k,\boldsymbol{\xi}^k,T_s) &= T_s\boldsymbol{\delta}_{\boldsymbol{\eta}} + \sum_{\ell=2}^{\infty}\left[L_{f+\delta_{\boldsymbol{\eta}}}^{\ell-1}\boldsymbol{\delta}_{\boldsymbol{\eta}} + L_{\delta_{\boldsymbol{\eta}}}^{\ell-1}\boldsymbol{f}\right]\frac{T_s^{\ell}}{\ell!} \\ \boldsymbol{\delta}_{\boldsymbol{\xi}}^k &= \boldsymbol{\delta}_{\boldsymbol{\xi}}(\boldsymbol{\eta}^k,\boldsymbol{\xi}^k,\mathbf{u}^k,T_s) \\ \boldsymbol{\delta}^D(\boldsymbol{\eta}^k,\boldsymbol{\xi}^k,\mathbf{u}^k,T_s) &= \sum_{\ell=2}^{\infty}L_{f_a+G_a(\mathbf{u}+\delta_{\boldsymbol{\xi}})}^{\ell-1}\boldsymbol{G}_a\boldsymbol{\delta}_{\boldsymbol{\xi}}\frac{T_s^{\ell}}{\ell!}\end{aligned} \tag{3.22}$$

While designing the SMC for both systems, the bounds of the uncertainties have to known. They will still use the same procedure as described earlier, but now the uncertainties will impose lower bounds, both to the sliding mode design and to the switching surface. These lower bounds guarantee that the system will reach the sliding manifold and will oscillate around it while sliding down to the origin.

3.3.1. Robust analog sliding mode controller design

Each one of the two step design processes will be modified by the presence of uncertainties, first the design of the sliding manifold, *i.e.* condition (3.2), has to take into account the $\boldsymbol{\delta}$ term, which can be translated to a choice of $\boldsymbol{\phi}(\boldsymbol{\eta})$ that satisfies:

$$\boldsymbol{\eta}^T \left[f(\boldsymbol{\eta}, \boldsymbol{\phi}(\boldsymbol{\eta})) + \delta_{\eta}(\boldsymbol{\eta}, \boldsymbol{\phi}(\boldsymbol{\eta})) \right] < 0 \tag{3.23}$$

Accomplishing this task requires the knowledge of the δ_{η} boundaries. Also the resulting reaching differential dynamics under the presence of uncertainties and using the same input format, eq. (3.5), will be:

$$\dot{\mathbf{s}} = \mathbf{v} + \delta_{\xi}(\boldsymbol{\eta}, \boldsymbol{\xi}, \mathbf{u}) - \frac{\partial \boldsymbol{\phi}}{\partial \boldsymbol{\eta}} \delta_{\eta}(\boldsymbol{\eta}, \boldsymbol{\xi}) \tag{3.24}$$

To asymptotically stabilize the reaching differential dynamics $\mathbf{v}$ could take the following form (proof C.4):

$$\mathbf{v} = -\frac{\left(\rho(\boldsymbol{\eta}, \boldsymbol{\xi}) + b_0\right)}{1 - \lambda} sign\left(\boldsymbol{\xi} - \boldsymbol{\phi}\right) \tag{3.25}$$

where λ belongs to the semi-closed interval [0,1) and ρ is a positive defined scalar function. Both are boundaries to the uncertainties on the reaching dynamics:

$$\left\| \delta_{\xi}(\boldsymbol{\eta}, \boldsymbol{\xi}, \mathbf{u}) - \frac{\partial \boldsymbol{\phi}}{\partial \boldsymbol{\eta}} \delta_{\eta}(\boldsymbol{\eta}, \boldsymbol{\xi}) \right\| < \rho(\boldsymbol{\eta}, \boldsymbol{\xi}) + \lambda \|\mathbf{v}\| \tag{3.26}$$

Notice that the switching function $\mathbf{v}$ now has a lower gain bound due to the uncertainties in the system dynamics. A similar derivation has already been presented in previous literature [32] and was given here for comparison reasons.

3.3.2. Robust digital sliding mode controller design

The necessary condition for the existence of a discrete sliding manifold, equation (3.15), has to incorporate the presence of uncertainties in the model. As a result a robust stable hyperplane, $\boldsymbol{\phi}^k(\boldsymbol{\eta})$, has a lower bound to overcome any effects of the structured uncertainties in the $\boldsymbol{\eta}$ discrete dynamics:

$$\left[f^D(\boldsymbol{\eta}^k, \boldsymbol{\xi}^k, T_s) + \delta_{\eta}^D(\boldsymbol{\eta}^k, \boldsymbol{\xi}^k, T_s) \right]^T \left[2\boldsymbol{\eta}^k + f^D(\boldsymbol{\eta}^k, \boldsymbol{\xi}^k, T_s) + \delta_{\eta}^D(\boldsymbol{\eta}^k, \boldsymbol{\xi}^k, T_s) \right] < 0 \tag{3.27}$$

For the continuous-time systems the dynamics of the sliding manifold could be expressed in terms of the $\boldsymbol{\eta}$ dynamics by using the chain rule, but this mathematical tool does not apply for difference equations. An alternative is to break down the sliding manifold discrete dynamics, $\boldsymbol{\phi}^{k+1}(\boldsymbol{\eta}^{k+1})$, into a known component ($\boldsymbol{\phi}_f^{k+1}$) plus an uncertainty component ($\boldsymbol{\phi}_s^{k+1}$). The feedback law (3.18) has to be modified to incorporate this change:

$$\mathbf{u}^k = \boldsymbol{G}_a^D(\boldsymbol{\eta}^k, T_s)^{-1}\left[-\boldsymbol{f}_a^D(\boldsymbol{\eta}^k,\boldsymbol{\xi}^k,T_s) - \boldsymbol{\phi}^k(\boldsymbol{\eta}^k,T_s) + \boldsymbol{\phi}_f^{k+1}(\boldsymbol{\eta}^k + \boldsymbol{f}(\boldsymbol{\eta}^k,\boldsymbol{\xi}^k),T_s) + \mathbf{v}^k\right] \quad (3.28)$$

The resulting reaching difference dynamics after incorporating the feedback $\mathbf{u}^k$ will be:

$$\mathbf{s}^{k+1} = \mathbf{s}^k + \mathbf{v}^k + \boldsymbol{G}_a^D(\boldsymbol{\eta}^k,T_s)\boldsymbol{\delta}_{\boldsymbol{\xi}}(\boldsymbol{\eta}^k,\boldsymbol{\xi}^k,\mathbf{u}^k) + \boldsymbol{\delta}^D(\boldsymbol{\eta}^k,\boldsymbol{\xi}^k,\mathbf{u}^k,T_s) - \boldsymbol{\phi}_{\boldsymbol{\delta}}^{k+1}(\boldsymbol{\eta}^{k+1},T_s) \quad (3.29)$$

The discrete attractor term ($\mathbf{v}^k$) has to be chosen to robustly drag the reaching difference dynamics to the origin. A similar sufficient condition as equation (3.27) can be stated for the **s** discrete dynamics (proof C.5):

$$\left[\mathbf{v}^k + \boldsymbol{\Delta}^k(\boldsymbol{\eta}^k,\boldsymbol{\xi}^k,\mathbf{u}^k,T_s)\right]^T\left[2\mathbf{s}^k + \mathbf{v}^k + \boldsymbol{\Delta}^k(\boldsymbol{\eta}^k,\boldsymbol{\xi}^k,\mathbf{u}^k,T_s)\right] < 0 \quad (3.30)$$

where:

$$\boldsymbol{\Delta}^k = \boldsymbol{G}_a^D(\boldsymbol{\eta}^k,T_s)\boldsymbol{\delta}_{\boldsymbol{\xi}}(\boldsymbol{\eta}^k,\boldsymbol{\xi}^k,\mathbf{u}^k) + \boldsymbol{\delta}^D(\boldsymbol{\eta}^k,\boldsymbol{\xi}^k,\mathbf{u}^k,T_s) - \boldsymbol{\phi}_{\boldsymbol{\delta}}^{k+1}(\boldsymbol{\eta}^{k+1},T_s) \quad (3.31)$$

Because the discretization introduces an upper bound and the uncertainties a lower bound it is not easy to create an attractor that satisfies both simultaneously. Su *et al.* [85] has an interesting solution to this problem: a reconstruction of the disturbances based on previous state measurements. This information could be used to define the behavior of $\boldsymbol{\Delta}^k$ and consequently find an appropriate attractor function ($\mathbf{v}^k$) that satisfies equation (3.30).

In case the discrete attractor for the uncertainty-free system is applied to the system, stability is mathematically guaranteed until the system reaches a region close to the sliding manifold, an operating mode called quasi-sliding [81]. This effect is demonstrated in proof C.5.

3.4. Case Study of a benchmark example

In this section a benchmark autonomous nonlinear system will be investigated to illustrate the theory proposed in this paper. Khalil [32] has investigated this system as an example in his book and has already designed the ASMC for the problem. The differential equation of interest is defined by the following:

$$\begin{aligned} \dot{x}_1 &= c_1 x_1^3 + c_2 x_1 x_2 \\ \dot{x}_2 &= c_3 u \end{aligned} \tag{3.32}$$

where c_i (i=1,2,3) are strictly positive scalars.

The origin of the system is an unstable equilibrium point, that is, any perturbation to that condition will drive the system away from that point. It is desirable to develop a control law (that chooses values for the input u) that asymptotically stabilizes the origin. Equation (3.32) is already the regular form and it is quite trivial to realize the similarity:

$$\begin{aligned} \boldsymbol{\eta} &= x_1 \\ \boldsymbol{\xi} &= x_2 \\ \boldsymbol{f}(\boldsymbol{\eta},\boldsymbol{\xi}) &= c_1 x_1^3 + c_2 x_1 x_2 \\ \boldsymbol{f}_a(\boldsymbol{\eta},\boldsymbol{\xi}) &= 0 \\ \boldsymbol{G}_a(\boldsymbol{\eta},\boldsymbol{\xi}) &= c_3 \\ \boldsymbol{u} &= u \end{aligned} \tag{3.33}$$

In the proposed example a simple discretized model will be explored, *i.e.* just the first term of the series will be used (N=1). This approximation is commonly known as Euler discretization method. Applying the method described by eqs. (3.7) to (3.13) to the dynamic system (3.32) one can get:

$$\begin{aligned} x_1^{k+1} &= x_1^k + T_s\left[c_1\left(x_1^k\right)^3 + c_2 x_1^k x_2^k\right] \\ x_2^{k+1} &= x_2^k + T_s c_3\left\{u^k\right\} \end{aligned} \tag{3.34}$$

It is relevant to notice that eq. (3.32) is differential and eq. (3.34) is a difference, which implies that distinct sets of mathematical tools operate over each system. Also, due to the simplicity of the discrete model being considered here, the time step used has to be sufficiently small to allow the model to capture the dynamic behavior of the original system.

3.4.1. Continuous controller design

The design of a sliding mode controller for this specific example have been explored in other literature [32] but it will be presented here once again to provide a direct comparison to the discrete method proposed in this paper. The goal in this example is to asymptotically stabilize the origin of the system described by equation (3.32).

The feedback law described by (3.5) requires the definition of a function ϕ that corresponds to a trajectory of ξ which asymptotically stabilizes the η dynamics. This trajectory is also known as the sliding manifold. A Lyapunov based technique is used to find such hyperplane, given in equation (3.2). One possible choice is:

$$\phi = -\alpha x_1^2 \tag{3.35}$$

where:

$$\alpha > \frac{c_1}{c_2} \tag{3.36}$$

Substituting (3.33) and (3.35) into (3.5) and (3.6) the analogic feedback law is:

$$\begin{aligned} u &= \frac{1}{c_3}\left[-2\alpha\left(c_1 x_1^4 + c_2 x_1^2 x_2\right) + \mathrm{v}\right] \\ \mathrm{v} &= -b_0 sign\left(x_2 + \alpha x_1^2\right) \end{aligned} \tag{3.37}$$

3.4.2. Discrete controller design

The design of a discrete sliding mode controller for the benchmark example starts from the application of the difference model equation (3.34) into the sufficient condition for the existence of the sliding manifold (eq. 3.15). A possible choice for such plane is the following:

$$\phi^k = -\alpha\left(x_1^k\right)^2 \tag{3.38}$$

To satisfy the sufficient condition (3.15) the follow constraints have to hold:

$$\begin{aligned} &2 + T_s\left[c_1 - \alpha c_2\right]\left(x_1^k\right)^2 > 0 \\ &c_1 - \alpha c_2 < 0 \end{aligned} \tag{3.39}$$

Equation (3.39) is a set of upper and lower boundaries for the sliding manifold design (selection of α). It is important to notice that both the state and the sampling time play a role in the upper bound, an incorporation of the discretization's effects into the

stability of the discrete control strategy. The discrete feedback control law for the this example is:

$$u^k = \frac{1}{T_s c_3}\begin{bmatrix} v^k - 2\alpha T_s\left[c_1\left(x_1^k\right)^4 + c_2\left(x_1^k\right)^2 x_2^k\right] - \\ \alpha T_s^2\left[c_1^2\left(x_1^k\right)^6 + 2c_1c_2\left(x_1^k\right)^4 x_2^k + c_2^2\left(x_1^k\right)^2\left(x_2^k\right)^2\right] \end{bmatrix} \qquad (3.40)$$

$$v^k = -b_0\left[x_2^k + \alpha\left(x_1^k\right)^2\right]$$

In the limit, where the sampling time (T_s) tends to zero, the discrete feedback law (u^k) tends to the continuous-time feedback law (u). The fundamental difference between the two control laws is in the attractor terms, where the continuous term (v) is a constant magnitude term while the discrete term (v^k) is proportional to the distance between the x^k_2 state and the sliding manifold.

3.4.3. Simulations

To perform numerical simulation using the example described in the previous section it is necessary to define a set of system parameters to determine the equations of motion. These properties are presented in table 3.1 as well as used in the system's initial conditions used to simulate the response, *i.e.* equation (3.1).

Table 3.1. System properties and initial conditions.

$c_1 = 1$	$c_2 = 1$	$c_3 = 3$
$x_1(0) = 1$	$x_2(0) = 1$	

Based on the condition presented by equation (3.36) one can choose a sliding manifold. In this simulation it was selected to be four (α=4), a value that satisfy condition (3.36). The controller gain was also chosen to be an arbitrary positive number (b_0=0.1). Simulations were done using MATLAB® numerical ordinary differential equation solver (ode45) with the default error tolerance and a time step of $1e^{-6}$ seconds. The resulting state evolution in time for the nonlinear system using the ASMC technique is presented in figure 3.3.

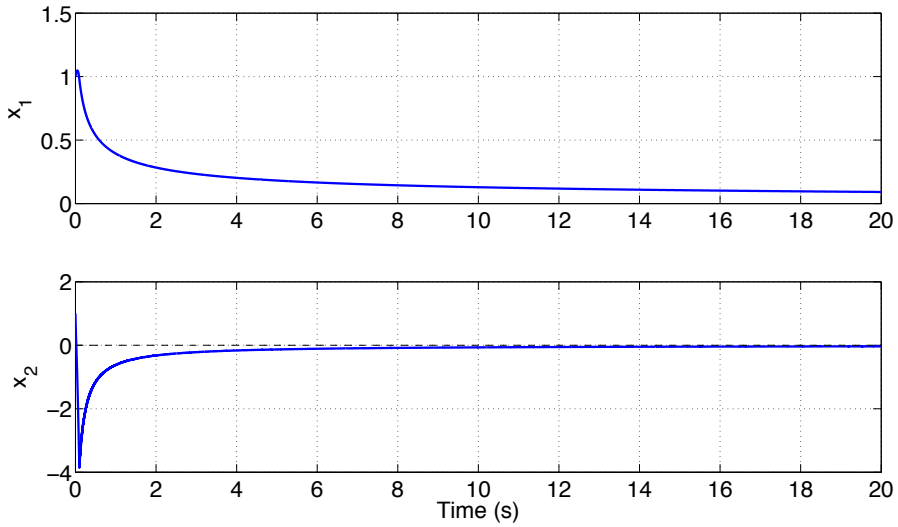

Figure 3.3. Analog sliding mode controlled (ASMC) states of equation (3.32).

Both states asymptotically converged to the origin (point indicated by the dashed line in the plot). The state x_2 was immediately driven to the negative region so that the x_1 could converge to zero, a behavior required due to specific characteristics of the dynamic system itself. The control action that drove the system to that point is the one described by equation (3.37) and is illustrated in figure 3.4.

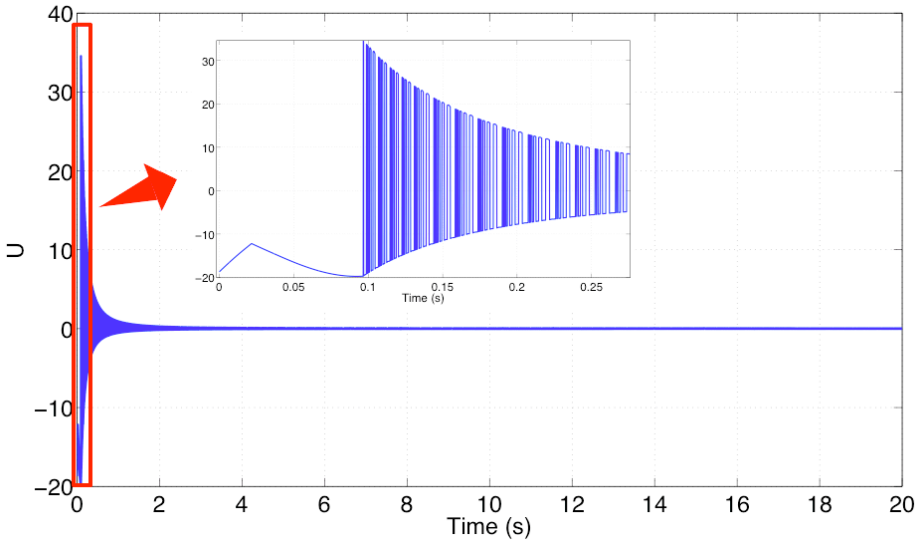

Figure 3.4. Control effort of an analog SMC (detail over the initial input behavior).

The control action starts with a high-gain input to quickly change the state's gradient and immediately respond to the current location of the states, operating in the reaching mode. After this fast response period, the state crosses the switching plane and activates different control structures. This behavior is expressed by the input chattering. The overall amplitude of this switching behavior is asymptotically decaying as the state reaches the equilibrium which represents a typical stable performance.

In order to evaluate the discrete controller approach proposed in this paper the same set of model parameters and initial conditions were used in simulation (table 3.1). It is important to mention that the choice of sliding manifold satisfies the constraints imposed by equation (3.39). The sampling time (T_s) used was $1e^{-3}$ seconds and the control gain was defined as one-tenth (b_0=0.1), which also satisfies the upper bound condition of the attractor defined by equation (3.19). Figure 3.5 presents the time evolution of the continuous system state under the DSMC feedback.

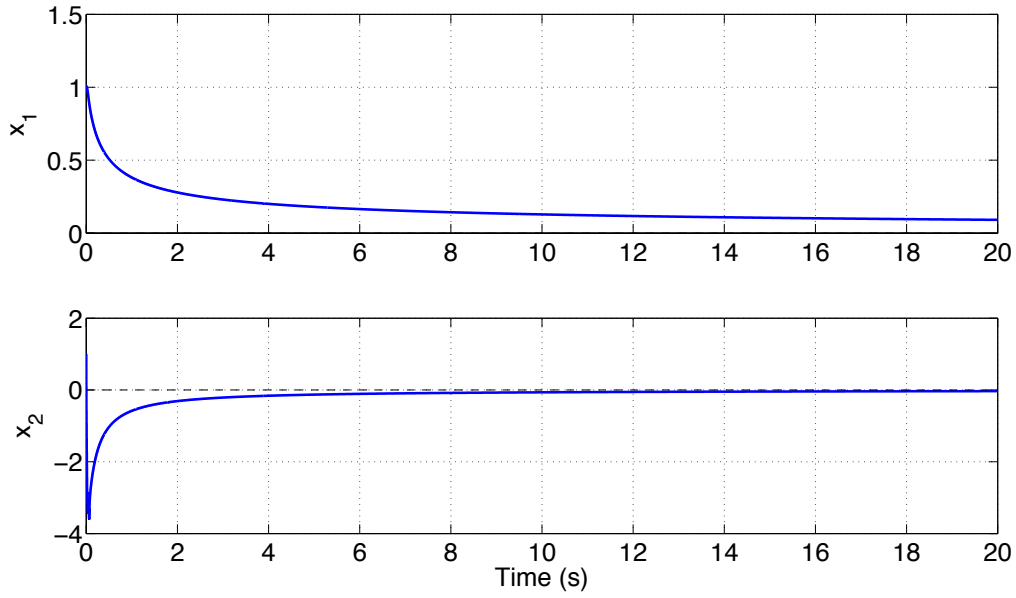

Figure 3.5. Digital sliding mode controlled (DSMC) states of equation (3.32).

Both states are asymptotically converging to the origin demonstrating that stability has been achieved. The continuous-time system was fed back with discrete control actions, defined by equation (3.40), over the sampling period T_s.

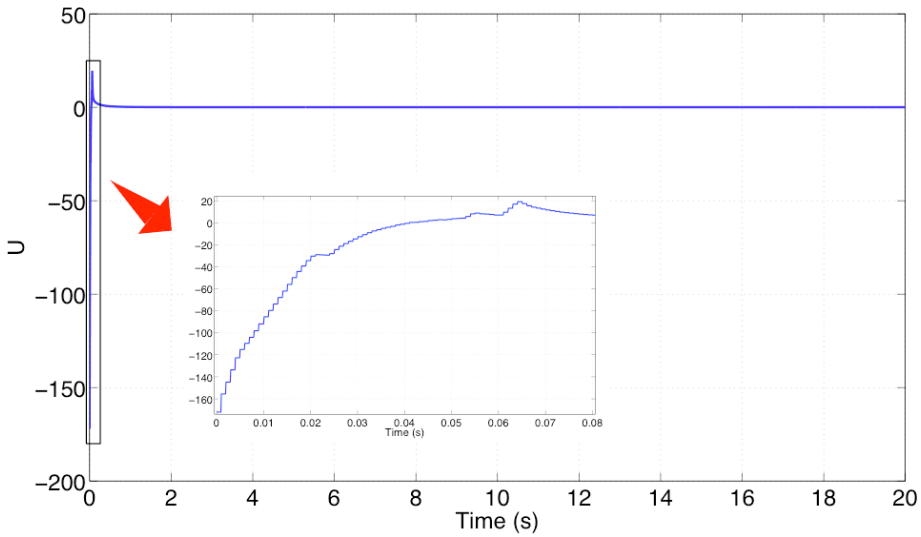

Figure 3.6. Resulting control action of a digital SMC with detail on the discrete input behavior.

The initial control action (figure 3.6) is a high negative gain, a necessary action to force the x_1 state to the origin. Rapidly after the input significantly reduces its magnitude and switches sign to drive the x_2 state to the equilibrium point.

The state trajectory for both controller design methods are quite similar but the input applied by each one is quite different. While the DSMC applied a high initial negative gain and rapidly decayed to a near zero input the ASMC applied a moderate initial input and started to chatter around the zero input.

The proposed DSMC technique for continuous-time nonlinear systems can be described in three steps: first, a Taylor-Lie discretization of the continuous-time system; second, a choice of an appropriate sliding manifold that satisfies the sufficient condition (3.15); and finally, a choice of attractor, equation (3.19). This systematic procedure and the concept development required to achieve this DSMC law are a major scientific contribution of this research.

This discrete nonlinear controller design tool (DSMC) has a wide range of applications, particularly for bio-inspired autonomous underwater vehicle, where the use of microprocessor combined with the structured uncertainties of the system's model poses an ideal problem for the use of the DSMC technique.

4. Jellyfish-Inspired Autonomous Underwater Vehicle Example

Autonomous Underwater Vehicles or AUV's are battery powered propulsive systems that operate and navigate underwater to perform a wide range of tasks and missions. These robotic devices differ from Remotely Operated Vehicles (ROV's) because they lack a tether that provides a direct line for information and energy transfer between the device and a host station. The fact that there is no linkage between the AUV and the base is a huge hydrodynamic advantage once there is no need for the vehicle to compensate for the dynamic influence of the cable. On the other hand communication and energy become critical issues for AUV's. Yuh [89] provides a complete survey on the design and control challenges for AUV's as well a very interesting list of projects and vehicles that have been developed during the past decade.

In order to improve upon the current AUV design, researchers are taking inspiration from nature by looking at how animals solved underwater locomotion challenges [90][91]. This bio-inspired approach has gained even more traction with the advancements in smart material actuators, such as shape memory alloys (SMAs) [92], ionic polymer-metal composite (IPMC) [93] and micro-fiber composite [94]. The reasoning behind imitating nature relies on the notion that nature has perfected its systems over millions of years of evolution, an optimization process that led to sequential improvements throughout generations of animals. This optimization process provides the capability for a given species to efficiently adapt itself to the underwater environment. By learning this cycle of improvements, researchers can not only achieve efficient AUV platform but also overcome survivability challenges.

Bio-inspired autonomous underwater vehicles (BIAUV) are fundamentally characterized by oscillatory motions of the vehicle's body (or portions of it) that produces a net thrust in a desired direction. The nature of this propelling force is periodic and its creation also affects the dynamics of the entire vehicle once it is required to actively deform or move a significant portion of the body. These intrinsic characteristics should be taken into account while designing the system's controller. Both chapters 2 and 3

present tools and discussions on the design of a controller that can efficiently drive the bio-inspired systems.

The goal of this chapter is to apply the tools and concepts previously described in this dissertation to a jellyfish-inspired autonomous underwater vehicle (JIAUV). It should be intuitive to the reader that jellyfish undergo large body deformations over each swimming pulsation, which is a fairly good representation of the basic feature of a BIAUV. Jellyfish also provide a simple oscillatory propulsive system model to understand the role of kinematic and morphological parameters towards thrust generation and maneuverability[16] [95].

Jellyfish with larger diameter tend to utilize rowing propulsion that involves periodic contraction and expansion of the bell with flexible margin generating large starting and stopping vortices. The interaction of these vortices provides thrust for swimming and determines the efficiency of propulsion [96]. Rowers are not proficient swimmers because they are not able to achieve high speeds or high maneuverability but they are efficient, that is, they use little energy to propel themselves and take advantage of the naturally occurring sea currents.

Villanueva *et. al.* [16] have demonstrated the biomimetic *Aureila aurita* robotic vehicles utilizing the bio-inspired shape memory alloy composite (BISMAC) fiber muscles. One of the significant findings of this study was the role of passive bell margins that provide greater than 1350% thrust production. However, this study also illustrated the challenges in finding the artificial muscles that can replicate the rhythmic contraction – expansion cycle with high electrical efficiency. Najem *et. al.* [95] have investigated a jellyfish-like underwater vehicle using IPMCs with the goal of reducing the magnitude of power consumed by muscles but that reduced the stroke achieved by the bell. The low frequency operation of IPMCs was matched to the kinematics of *aequorea victoria* species. There are several other studies reported in literature on development of jellyfish-inspired vehicles with variety of different actuation mechanisms and morphology [97][98][99][100].

Jellyfish inspired underwater vehicles is a reality and therefore can be used as very illustrative example of a bio-inspired system. A hypothetical JIAUV mathematical model will be derived and used in this chapter as means to develop a control strategy

suitable for this type of system. This virtual test bed allows for the design of some control architectures making use of the sliding mode control theory presented in chapter 3.

Section 4.1 of this chapter proposes and simulates a kinematic, dynamic and thrust generation model that captures the essential features of a generic bio-inspired system. Section 4.2 details the execution control architectures to be implemented in this JIAUV example. The derivation of the control laws, for both analog and digital SMC are given in section 4.3. Finally the control architectures are tested and directly compared in the final section of this chapter.

4.1. Modeling of JIAUV

Prior literature on jellyfish-inspired autonomous underwater vehicles (JIAUV) has been on understanding of the basic propulsion mechanism and in mimicking the kinematic performance [97][98][99][100]. Little attention has been paid towards the description of an appropriate vehicle dynamic and kinematic model. For fish-like undulating structures, dynamic modeling has been pursued [101] that has resulted in creation of a simulation tool, which simplifies the design of robotic vehicles.

This section is dedicated to providing a simple mathematical model for the JIAUV that captures the most basic features of the systems, such as, pulsate swimming behavior and stable orientation when the vehicle is not being actuated. As a final result this model provides a map between the swimming amplitude of the vehicle and its displacement/attitude. The modeling process was divided into three steps: kinematics, dynamics and thrust modeling. Each step is presented and discussed in the following subsections.

4.1.1. Kinematic modeling

The first step in the development of the kinematic model is to define the relevant frame of reference. Figure 4.1 is an illustration of a jellyfish-inspired autonomous underwater vehicle (JIAUV) with a body-fixed reference frame. It is important to notice that the origin of the body-fixed frame is located at the center of buoyancy, *i.e.* the geometrical center of the vehicle volume. It is also represented in the inertial frame which has its z-axis aligned with the gravitational field of earth in the opposite direction.

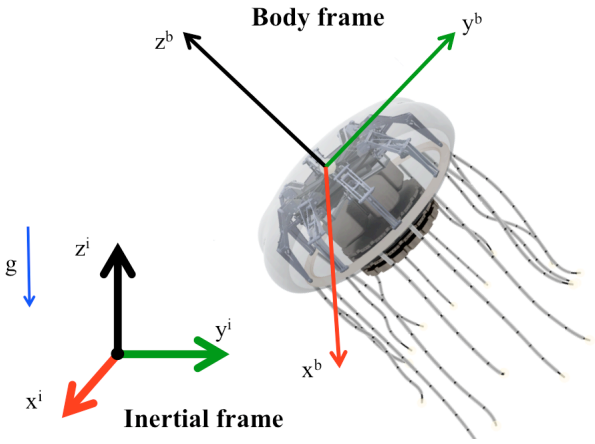

Figure 4.1. Illustration of a biomimetic JIAUV with the body and inertial reference frames representation.

A rotation is a mathematical operation that converts a vector described in one frame of reference to another. Such an operation is also known as coordinate transformation and can be written to convert any physical vector property (velocity, rotation speed, etc.) from the body frame of reference to the inertial frame of reference. In this paper it is defined using the quaternion notation as described in detail elsewhere [103]:

$$\mathbf{R}_{\mathrm{i}}^{\mathrm{b}} = \mathbf{I} + 2q_0\mathbf{S}(\mathbf{q}_n) + 2\mathbf{S}^2(\mathbf{q}_n) \tag{4.1}$$

where q_0 corresponds to the angle of rotation, $\mathbf{q}_n$ is the axis of rotation and $\mathbf{S(e)}$ is the cross product operator, defined as:

$$\mathbf{S}(\mathbf{e}) = \begin{bmatrix} 0 & -e_3 & e_2 \\ e_3 & 0 & -e_1 \\ -e_2 & e_1 & 0 \end{bmatrix} \tag{4.2}$$

The Euler parameter vector (quaternions) can then be described by a fourth order vector that is a composition of the magnitude of rotation q_0 and the axis of rotation $\mathbf{q}_n$:

$$\mathbf{q} = \begin{Bmatrix} q_0 \\ \mathbf{q}_n \end{Bmatrix} = \begin{Bmatrix} q_0 \\ q_1 \\ q_2 \\ q_3 \end{Bmatrix} \tag{4.3}$$

One important characteristic imposed on the quaternion representation is that they satisfy the unitary condition, that is:

$$q_0^2 + \mathbf{q}_n^T \mathbf{q}_n = 1 \tag{4.4}$$

An inverse rotation, in quaternion notation, is simply represented by a negative sign in the rotation axis. This simply implies that the rotation is by same magnitude in the opposite direction. This Euler parameter is also known as the conjugate and is denoted by a superscript (-1). Using the inverse Euler parameter one can also define the inverse coordinate transformation:

$$\mathbf{R}_{\mathrm{b}}^{\mathrm{i}} = \left(\mathbf{R}_{\mathrm{i}}^{\mathrm{b}}\right)^{\mathrm{T}} = \mathbf{I} + 2q_0\mathbf{S}(-\mathbf{q}_n) + 2\mathbf{S}^2(-\mathbf{q}_n) \tag{4.5}$$

The rate at which quaternions change due to a relative rotation between the frames is given as [103]:

$$\begin{aligned} \dot{q}_0 &= -\frac{1}{2}\mathbf{q}_n^{\mathrm{T}}\boldsymbol{\omega}_{\mathrm{ib}}^{\mathrm{b}} \\ \dot{\mathbf{q}}_n &= \frac{1}{2}\left[q_0\mathbf{I} + \mathbf{S}(\mathbf{q}_n)\right]\boldsymbol{\omega}_{\mathrm{ib}}^{\mathrm{b}} \end{aligned} \tag{4.6}$$

where $\boldsymbol{\omega}_{\mathrm{ib}}{}^{\mathrm{b}}$ are the rotations between inertial and body frame described in the body reference frame. It is important to notice that that the superscript dot indicates the derivative with respect to time.

The rotational matrix (4.1) can also be used to transform the body frame velocities into inertial frame velocities as:

$$\mathbf{v}^{\mathrm{i}} = \mathbf{R}_{\mathrm{i}}^{\mathrm{b}}\mathbf{v}^{\mathrm{b}} \tag{4.7}$$

Equations (4.6) and (4.7) provide the vehicle kinematics. If a time history of body rotations and velocities is considered, the integration of both equations over this path will describe the position in space and vehicle orientation over time.

4.1.2. Dynamic modeling

The source of body velocities and rotations are forces and torques applied to the body. Forces and torques can be classified in two groups: external force/torque if it is caused by an uncontrollable phenomenon and input force/torque if we can control (or adjust) the source. For the JIAUV, a typical external force/torque arises from gravitational (subscript g) and buoyancy (subscript B) forces. Figure 4.2 shows the

schematic representation where each force on the vehicle is applied and defines two important points, the gravity and the buoyancy centers, CG and CB, respectively.

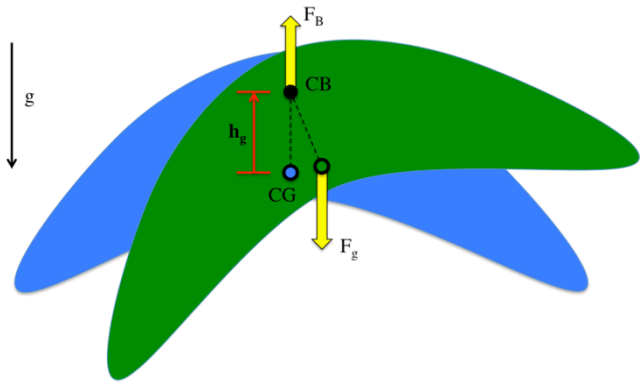

Figure 4.2. Position of the center of gravity (CG) and center of buoyancy (CB) as well as the external forces applied on those points.

The vehicle rigid-body dynamics can be approximated by the following set of equations [89]:

$$\dot{\mathbf{v}}^{b} = \mathbf{M}^{-1}\left(\mathbf{S}(\mathbf{M}\mathbf{v}^{b})\boldsymbol{\omega}_{ib}^{b} - \mathbf{D}_{v}\mathbf{v}^{b} + \mathbf{R}_{b}^{i}(\mathbf{F}_{g} + \mathbf{F}_{B}) + \mathbf{F}\right) \tag{4.8}$$

$$\dot{\boldsymbol{\omega}}_{ib}^{b} = \mathbf{J}^{-1}\left(\mathbf{S}(\mathbf{J}\boldsymbol{\omega}_{ib}^{b})\boldsymbol{\omega}_{ib}^{b} + \mathbf{S}(\mathbf{M}\mathbf{v}^{b})\mathbf{v}^{b} - \mathbf{D}_{\omega}\boldsymbol{\omega}_{ib}^{b} + \mathbf{S}(\mathbf{R}_{b}^{i}(\mathbf{F}_{g} - \mathbf{F}_{B}))\mathbf{h}_{g} + \mathbf{T}\right) \tag{4.9}$$

where $\mathbf{M}$ is the mass matrix, $\mathbf{D}_{v}$ is the linear damping matrix, $\mathbf{h}_{g}$ is the distance from CG to CB, $\mathbf{J}$ is the inertia matrix, $\mathbf{D}_{\omega}$ is the rotational damping matrix, $\mathbf{F}$ is the force vector and $\mathbf{T}$ is the torque vector. The superscript (-1) indicates the inverse matrix. It is important to notice that each one of the equations above is three dimensional, resulting in a set of 6 differential equations.

A critical issue with equations (4.8) and (4.9) is the fact that they would not capture the change in body shape (and consequently body properties) of the JIAUV. Figure 4.3 exemplifies these changes by showing the JIAUV Cyro® developed at Virginia Tech in two configurations, open and closed bell. It is required, in order to the vehicle produce thrust, that at least one section of the bell cycles between both configurations.

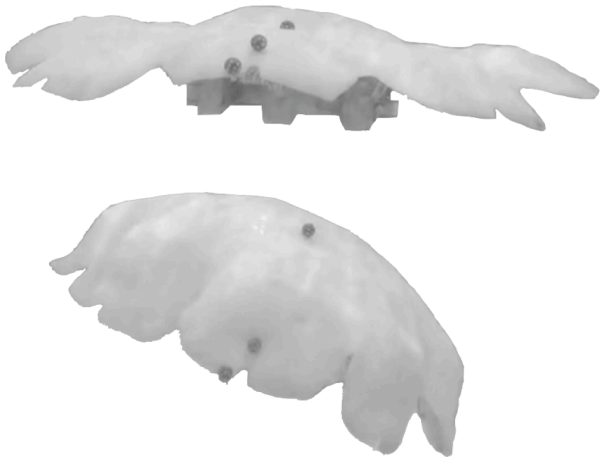

Figure 4.3. Cyro® is JIAUV develop at Virginia Tech. This robot has eight independent bell sections that can contract and relax independently. In the top the JIAUV is in the open (or relaxed) bell configuration. Bottom image shows the vehicle in the closed (contracted) configuration.

Simple static experimental tests can be conducted to evaluate the change in behavior of the JIAUV in each configuration (fully open and fully closed bell). Figure 4.4 displays the result of two simple tests. The upper plot corresponds to sinking test, where the vehicle is set inside the pool in a fixed configuration and its depth is recorded. The bottom plot corresponds to the tilt-and-release test, in which the JIAUV is set at an starting angle and is released to achieve its stable orientation (in this case upwards aligned with the gravitational field). Each test was performed for both relaxed and contracted configurations.

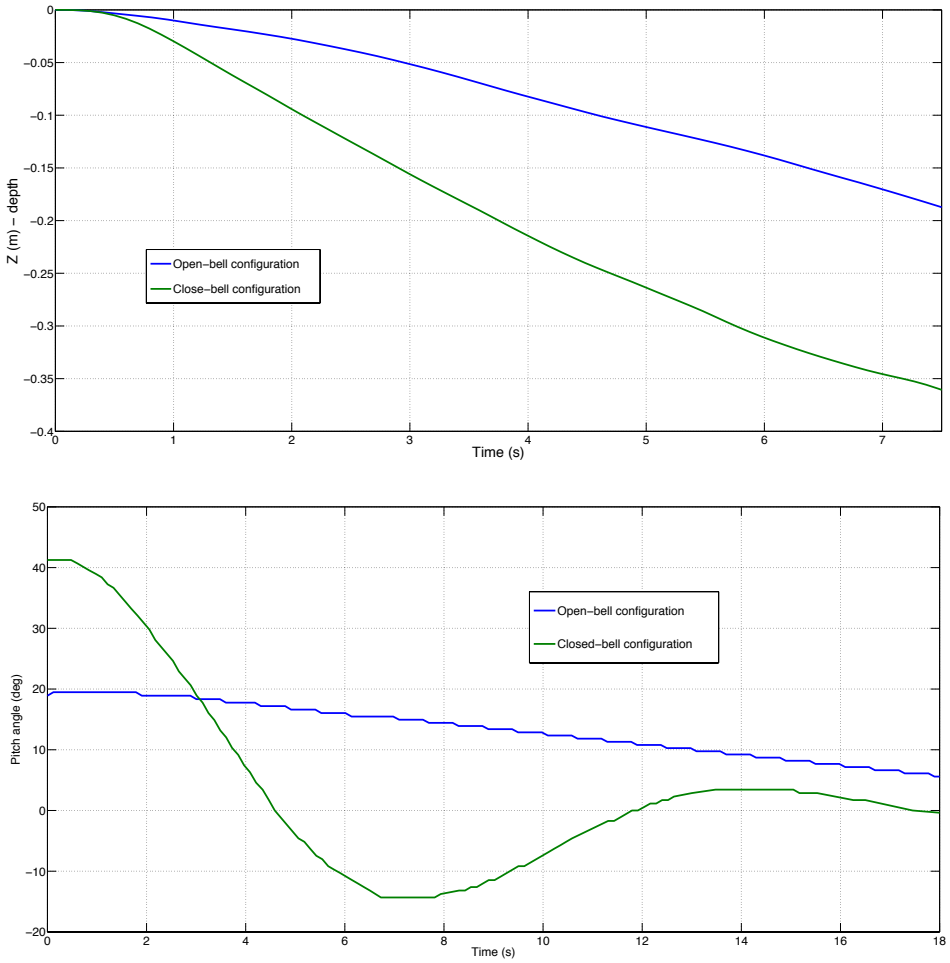

Figure 4.4. Upper plot: Sinking test; Bottom plot: tilt-and-release test.

For each test it is possible to fit the dynamic model described by equation (4.8) and 4.9) to match the experimental data obtained. If one does so, it is conceivable that the model properties for each configuration are going to be different. For example, the higher sinking rate for the closed-bell configuration (when to compared to the open-bell), is captured by the model as a decrease in the linear damping matrix ($\mathbf{D}_v$).

An alternative is to transform the dynamic model properties into time-dependent variables that changes its values in the same rate in which the vehicle is being pulsated. It implies that the mass matrix, the linear damping matrix, the distance from CG to CB, the inertia matrix and the rotational damping matrix are non-autonomous model parameters with boundary values defined by the open and closed bell configurations.

It is important to notice that the author recognizes the implications of assuming, for example, a time-varying mass matrix which would produce additional dynamic terms due to the fact that the linear momentum of the system changes due to the mass change over time. These new dynamic terms are being ignored in this analysis in order to keep the overall analysis simple enough to just capture the basic dynamic behavior.

The differential equations, from eq. (4.6) to eq. (4.9), represent the kinematic and dynamic equation of the vehicle. By solving this set of 13 differential equations for a time history of applied forces and torques and initial conditions, the trajectory in space and vehicle orientation is determined.

4.1.3. Thrust modeling

A jellyfish in an aquatic environment is able to propel itself and maneuver by performing periodic body contractions that result in generation of starting and stopping vortices. Interaction of these vortices results in the thrust production in a given direction. The major section of the jellyfish body, also known as bell, has embedded collagen fiber based muscles mainly oriented in circular and radial directions. Radial muscles are capable of creating asymmetric bell contractions resulting in animal maneuvering in water [19]. Since it is fairly complex to replicate the exact actuation mechanism of the animal itself, research has focused on an alternative approach where the bell is divided into sections that are discretely actuated. The bell segmentation is a natural phenomenon that occurs in some species of jellyfish, *e.g. Cyanea Capillata,* and eliminates the folding phenomenon that occurs in all the artificial bells.

In ideal conditions, the model should be able to take into account individual actuation of each bell segment to independently determine the force and torque acting on the vehicle body. The expressions below provide the forces and torques applied on the vehicle by the controlled action:

$$\mathbf{F} = \sum_{i=1}^{n} \mathbf{F}_i \tag{4.10}$$

$$\mathbf{T} = \sum_{i=1}^{n} \mathbf{S}(-\mathbf{h}_i)\mathbf{F}_i \tag{4.11}$$

where $\mathbf{F}_i$ is the total force produced by each segment of the bell, $\mathbf{h}_i$ is the point where it is applied on the body and n is the number of bell segments in the JIAUV (number of actuators).

The force created by each bell segment of the JIV is highly nonlinear and is resultant of the two-way complex fluid-structure interaction process. Thus, the exact modeling of this force would require detailed computational fluid dynamic simulations that integrate the hyperselastic structural model with the nonlinear Navier-Stokes expressions. For the purposes of this study, we simplified the problem as described below without lack of any important physics.

The actuation of one bell segment is composed of two stages: a contraction followed by a relaxation. In the contraction period (also known as power stroke) the force is created in the desired direction that propels the animal forward. In order to perform another power stroke the vehicle has to bring the bell segment back to its original position with a passive relaxation. This action creates a negative force with lower amplitude when compared to the contraction period. The overall cycle can be described as the average force in the desired direction combined with a pulsating (periodic) component. The control action does not affect the period of the contraction but increases the amplitude of both average and pulsating forces. Mathematically the model of the bell segment actuator force is described as:

$$\mathbf{F}_i = \left[\mathbf{F}_i^{avg} + \mathbf{F}_i^{pul}(T)\right] u_i \tag{4.12}$$

where u_i is the controlled parameter, $\mathbf{F}_i^{avg}$ is the net force produced by a swimming cycle, $\mathbf{F}_i^{pul}$ is pulsating force produced in the swimming cycle (it is a time-varying component of the thrust) and T is the swimming period (inverse of the frequency) of the vehicle.

It is important to mention that the control input described here follows the findings presented in chapter 2, where it suggests that the BIAUV should operate in its resonant frequency and only tune/control the amplitude of the oscillatory force. The swimming period (T) should, by this logic, be appropriately selected to guarantee that the vehicle will be operating in its propulsion resonance.

By combining equations (4.10) and (4.11) to the dynamics model, *i.e.* equations (4.8) and (4.9), a set of six nonlinear time-varying differential equation are obtained.

4.1.4. Model simulation

To demonstrate the capabilities of the modeling approach in representing a JIAUV series of numerical simulations were performed. The time-varying model properties we described of superscript *Hi* and *Low* properties and oscillates according to the following relation:

$$p = p^{Low} + \left(p^{Hi} - p^{Low}\right)\frac{\left[\cos\left(2\pi t/T\right)+1\right]}{2} \quad where \quad p = \mathbf{M},\mathbf{D}_{\mathbf{v}},\mathbf{J},\mathbf{D}_{\boldsymbol{\omega}},\mathbf{h}_{g} \tag{4.13}$$

The properties values used in the following simulated results and considered to represent a "real physical system" are given in appendix D. The first numerical test is similar to the tilt-and-release test previously described, where the vehicle is set to a certain orientation and it is freed to return to its stable orientation and sink. In this test the vehicle properties do not change since any swimming body motion is being performed by the JIAUV. Figure 4.5 presents the results of such simulation.

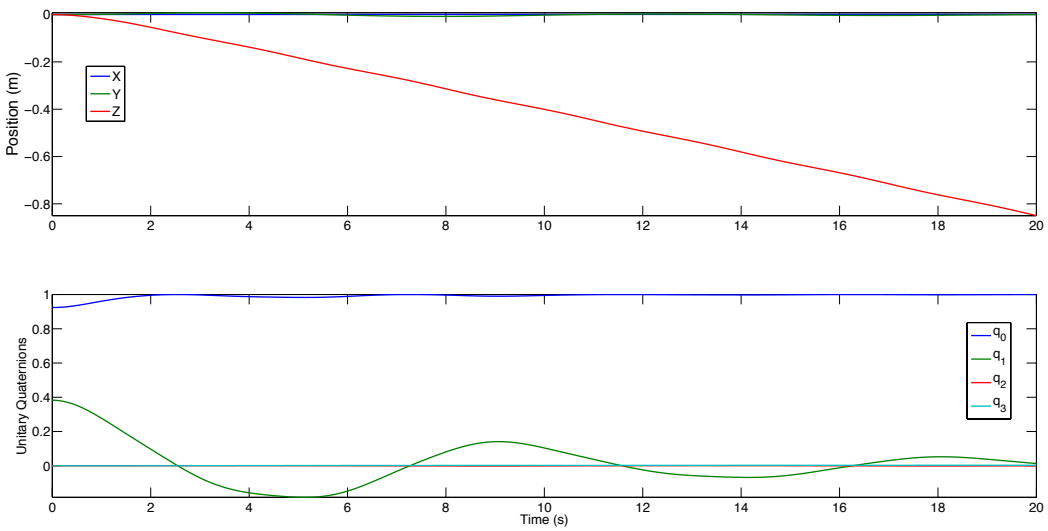

Figure 4.5. Tilt-and-release simulation of the non actuated JIAUV.

The next simulation test is a homogeneous (or full) contraction of the JIAUV, such that the same amplitude of contraction is input at each one of the bell's segments. The vehicle being simulated here has 4 bell segments precisely aligned with the body axis coordinates, *i.e.* two at the *x*-axis and two at the y-axis. Each actuator (bell segment) produces force only in the positive z^b-direction and the oscillatory component of the force

is 80% of the amplitude commanded to the average one. Figure 4.6 plots the forward swimming behavior for a JIAUV commanded with input amplitude of 2 for all bell sections.

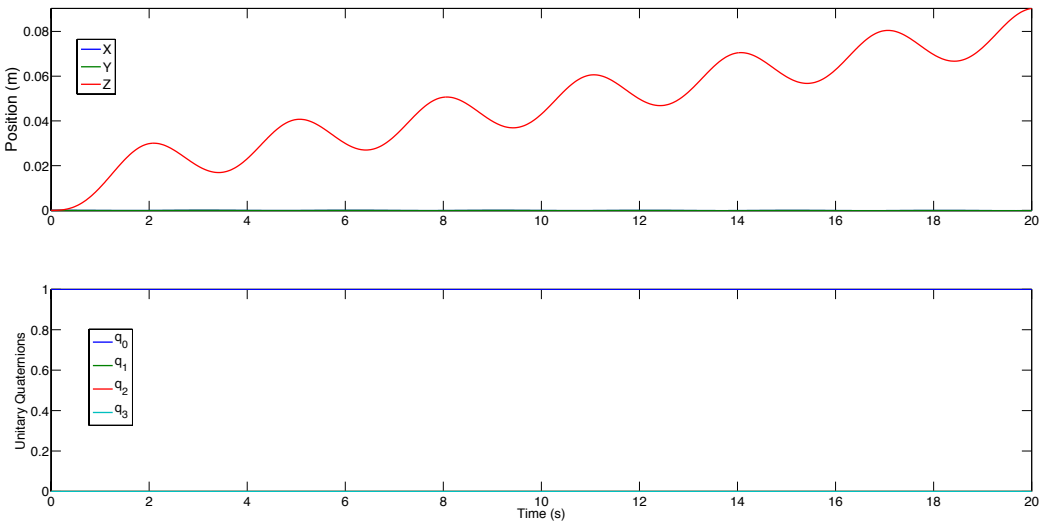

Figure 4.6. Forward swimming behavior of and homogeneous contraction of the all the bell section with input amplitude of 2.

It is clear from figure 4.6 that the JIAUV has a beating period of 3 seconds. Also a pair of bell segments that is aligned with an axis (either x^b or y^b) has each of its elements opposing each other equidistance from the origin of the reference frame, corresponding to the same norm of $\mathbf{h}_i$. All this information is presented in more detail in appendix D.

Because of the eccentricity of the bell segments a torque is produced in the vehicles body when a segment is contracted. This moment of the force can be used to turn the JIAUV about its center of buoyancy permitting and adjustment in the vehicle orientation. Figure 4.7 is the model simulation of the JIAUV when only one of the bells segments is being actuated, in this case the one localized in the positive x^b direction, which produce a rotation about the y^b axis. This numerical test demonstrates the turning capabilities of the vehicle.

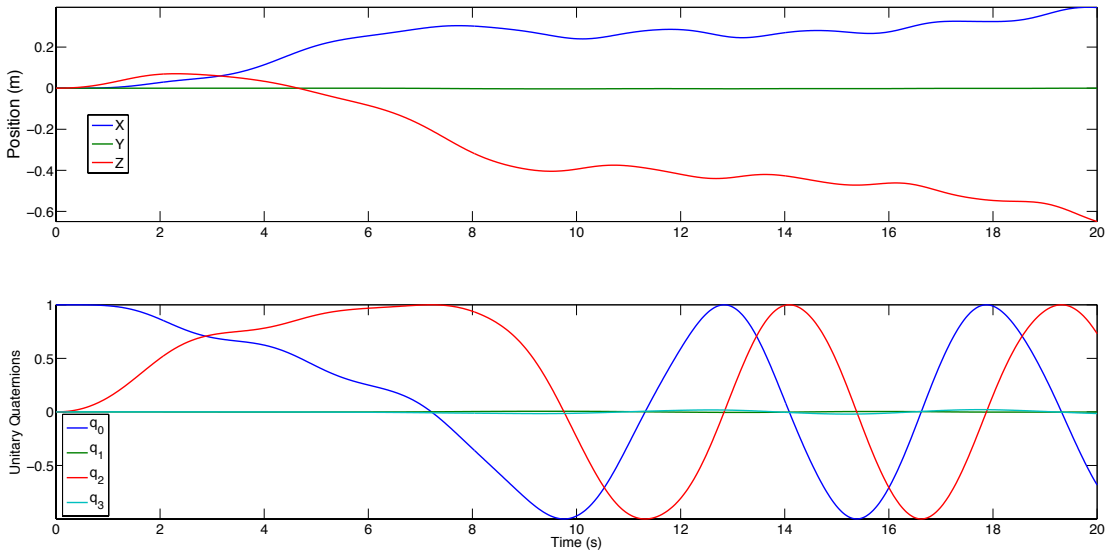

Figure 4.7. Turning test of the JIAUV with actuation on the bell segment located in the positive x^b direction with input amplitude of 12.

These numerical simulations of the "virtual" JIAUV were crucial to prove that the mathematical model being used can, indeed, capture the most basic features of a physical vehicles, such as, existence of a stable orientation, pulsating swimming behavior and turning capabilities.

4.2. Execution control architectures

One important aspect to consider while designing the controller for JIAUV is to have an understanding of the limitations of rowing propulsion mechanism. Since the animal/vehicle can only propel itself in one direction (positive z^b) the control algorithm has to take that fact into account. One possible solution is to have two routines embedded in the vehicle electronics: the first one points the vehicle in the desired direction while the second one propels the vehicle forward when the first condition is satisfied. Figure 4.8 illustrates one of the possible realization schemes for this uncoupled solution, which will be named here the turn-and-go strategy.

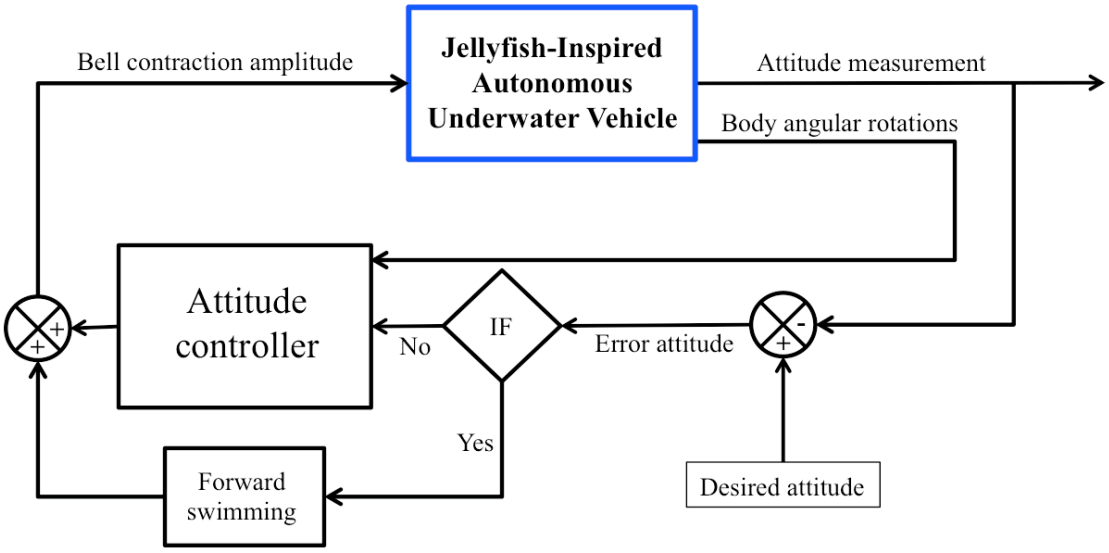

Figure 4.8. Realization of the turn-and-go control strategy for the JIAUV

The inner loop in figure 4.8 corresponds to an attitude controller that is responsible to drive the vehicle to the desired orientation in case the IF statement fails. Once the vehicle achieves the commanded attitude the forward swimming routine is activated to drive the vehicle to the desired location. It is important to notice that the position of the vehicle is not being considered as an output of the system due to the challenges in properly measuring global inertial coordinates in the x^i-y^i plane while operating underwater. The control strategy presented here would allow, for example, following a nearby target or reaching the source of a beam signal detected by the vehicle.

The great challenge for the turn-and-go strategy is to make sure that the inner loop satisfies its requirement and reach the desired orientation. It then becomes crucial to understand and properly define each element of the block diagram presented by figure 4.8. The vehicle attitude corresponds to its orientation when compared to the reference inertial frame. The attitude deviation corresponds to a relative orientation between the actual attitude and the desired one. It can also be understood as an error attitude and will be defined in this section. First, we define the product operation between two quaternions (it is a non-commutative operation) as:

$$\mathbf{q}^1 \otimes \mathbf{q}^2 = \begin{bmatrix} q_0^1 q_0^2 - \left(\mathbf{q}_n^1\right)^{\mathrm{T}} \mathbf{q}_n^2 \\ q_0^1 \mathbf{q}_n^2 + q_0^2 \mathbf{q}_n^1 + \mathbf{S}\left(\mathbf{q}_n^1\right)\mathbf{q}_n^2 \end{bmatrix} \tag{4.14}$$

The quaternion deviation is based on the product operation described earlier, where $\mathbf{q}^d$ is the desired unitary orientation:

$$\tilde{\mathbf{q}} = \begin{Bmatrix} \tilde{q}_0 \\ \tilde{\mathbf{q}}_n \end{Bmatrix} = \mathbf{q}^d \otimes \mathbf{q} = \begin{bmatrix} q_0^d q_0 - \left(\mathbf{q}_n^d\right)^{\mathrm{T}} \mathbf{q}_n \\ q_0^d \mathbf{q}_n + q_0 \mathbf{q}_n^d + \mathbf{S}\left(\mathbf{q}_n^d\right)\mathbf{q}_n \end{bmatrix} \tag{4.15}$$

It is important to notice that this definition satisfies the unitary condition. The kinematics of the quaternion deviation are given as:

$$\begin{aligned} \dot{\tilde{q}}_0 &= -\frac{1}{2}\tilde{\mathbf{q}}_n^{\mathrm{T}}\tilde{\boldsymbol{\omega}} \\ \dot{\tilde{\mathbf{q}}}_n &= \frac{1}{2}\left[\tilde{q}_0\mathbf{I} + \mathbf{S}(\tilde{\mathbf{q}}_n)\right]\tilde{\boldsymbol{\omega}} \end{aligned} \tag{4.16}$$

where the relative rotation is defined, assuming a rotation of the desired orientation ($\boldsymbol{\omega}_{\mathrm{id}}^{\mathrm{b}}$) as:

$$\tilde{\boldsymbol{\omega}} = \boldsymbol{\omega}_{\mathrm{id}}^{\mathrm{b}} - \boldsymbol{\omega}_{\mathrm{ib}}^{\mathrm{b}} \tag{4.17}$$

When the quaternion deviation is $[1\ 0\ 0\ 0]^{\mathrm{T}}$ this means that the actual quaternion matches the desired orientation. A simple change of variables can shift the matching condition to a point at the origin $[0\ 0\ 0\ 0\ ]^{\mathrm{T}}$.

$$\mathbf{z}_1 = \begin{Bmatrix} \tilde{q}_0 - 1 \\ \tilde{\mathbf{q}}_n \end{Bmatrix} \tag{4.18}$$

Because of the simplicity of the change of variables described above, the time derivative of the $\mathbf{z}_1$ variable is identical to eq. (4.16).

The next and most important step is the turn-and-go control scheme is to actually design the attitude controller. As discussed in the first chapter of this dissertation, the use a model-based technique, in particular sliding mode controllers, can provide a reliable law that will drive the system to the desired orientation. In the example being carried out here three different controllers will be derived and implemented. The first two approaches makes use of the analog sliding mode control (ASMC) law, previously described in chapter 3, to describe which input should be applied to the vehicle based on

the current attitude error. While the first controller continuously modifies the input to the JIAUV the second can only choose a new input to the system after waiting a sampling period (T_s), which corresponds to a discrete implementation of the ASMC law. The third controller to be applied is the digital sliding mode controller (DSMC), a law specifically designed for the discrete implementation. The following sections derive the control laws and simulate the response of the mathematical model presented in section 4.1 when controlled by these three strategies.

4.3. Design of sliding mode controllers

Before commencing the design of the control laws it is necessary to pose the problem in the correct format, *i.e.* expressing the model in its normal form with an equilibrium point at the origin. The first step is to describe the vehicle dynamic and error attitude kinematic (4.16) equations in the proper format. In order to do so some simplifications are required: (i) the desired body rotations ($\boldsymbol{\omega}_{id}^{b}$) will be ignored which implies that the relative rotation is equal to the negative body rotation, (ii) the dynamic term that is related to linear body velocities on equation (4.9) will be dropped, and (iii) the dynamic equation is written in terms of known estimates of the model properties denoted by an over-bar. The seven differential equations used in the attitude controller design are:

$$\dot{\mathbf{z}}_1 = \begin{Bmatrix} \dot{\tilde{q}}_0 \\ \dot{\tilde{\mathbf{q}}}_n \end{Bmatrix} = -\frac{1}{2}\begin{bmatrix} \tilde{\mathbf{q}}_n^{\mathrm{T}} \\ -\left[\tilde{q}_0\mathbf{I} + \mathbf{S}(\tilde{\mathbf{q}}_n)\right] \end{bmatrix}\left(\boldsymbol{\phi}_{id}^{b} - \boldsymbol{\omega}_{ib}^{b}\right) = \frac{1}{2}\begin{bmatrix} \tilde{\mathbf{q}}_n^{\mathrm{T}} \\ -\left[\tilde{q}_0\mathbf{I} + \mathbf{S}(\tilde{\mathbf{q}}_n)\right] \end{bmatrix}\boldsymbol{\omega}_{ib}^{b} \quad (4.19)$$

$$\dot{\boldsymbol{\omega}}_{ib}^{b} = \dot{\boldsymbol{\phi}}_{id}^{b} - \dot{\tilde{\boldsymbol{\omega}}} = \bar{\mathbf{J}}^{-1}\left(\mathbf{S}(\bar{\mathbf{J}}\boldsymbol{\omega}_{ib}^{b})\boldsymbol{\omega}_{ib}^{b} - \bar{\mathbf{D}}_{\boldsymbol{\omega}}\boldsymbol{\omega}_{ib}^{b} + \mathbf{S}(\mathbf{R}_b^i(\mathbf{F}_g - \mathbf{F}_B))\bar{\mathbf{h}}_g\right) + \bar{\mathbf{J}}^{-1}\bar{\boldsymbol{\Phi}}\left(\mathbf{u} + \boldsymbol{\delta}\right) \quad (4.20)$$

where $\mathbf{u}$ is the input vector (the stack of the u_i controlled parameters), $\boldsymbol{\Phi}$ is the input coefficient matrix and $\boldsymbol{\delta}$ is the model uncertainties term. The last two term are mathematically described as:

$$\begin{aligned} \boldsymbol{\Phi} &= \left[\boldsymbol{\Phi}_1 \;\; \boldsymbol{\Phi}_2 \;\; \boldsymbol{\Phi}_3 \;\; \boldsymbol{\Phi}_4\right] \\ \boldsymbol{\Phi}_i &= \mathbf{S}(-\mathbf{h}_i)\left[\bar{\mathbf{F}}_i + \tilde{\mathbf{F}}_i \sin(\alpha t)\right] \quad i = 1,2,3,4 \end{aligned} \quad (4.21)$$

$$\begin{aligned} \boldsymbol{\delta} &= -\bar{\boldsymbol{\Phi}}^{-1}\left(\mathbf{S}(\bar{\mathbf{J}}\boldsymbol{\omega}_{ib}^{b})\boldsymbol{\omega}_{ib}^{b} - \bar{\mathbf{D}}_{\omega}\boldsymbol{\omega}_{ib}^{b} + \mathbf{S}(\mathbf{R}_b^i\mathbf{F}_g)\bar{\mathbf{h}}_g\right) \\ &+ \bar{\boldsymbol{\Phi}}^{-1}\bar{\mathbf{J}}\mathbf{J}^{-1}\left(\mathbf{S}(\mathbf{J}\boldsymbol{\omega}_{ib}^{b})\boldsymbol{\omega}_{ib}^{b} - \mathbf{D}_{\omega}\boldsymbol{\omega}_{ib}^{b} + \mathbf{S}(\mathbf{R}_b^i\mathbf{F}_g)\mathbf{h}_g\right) + \left(\bar{\boldsymbol{\Phi}}^{-1}\bar{\mathbf{J}}\mathbf{J}^{-1}\boldsymbol{\Phi} - \mathbf{I}\right)\mathbf{u} \end{aligned} \quad (4.22)$$

where $\boldsymbol{\Phi}^{-1}$ is the pseudo inverse of the estimated input coefficient matrix. It is extremely important for all derivations that follow that this matrix exists for all time t.

In this controller design the model is assumed to behave in a similar manner as the physical system, but the model parameters are not accurate, resulting in a mismatch. In such situation, controllers designed with model-based techniques, *e.g.* backstepping, could not drive the system to a stable configuration, if the theory is based on dynamics cancelation (which might not occur). Considering the same kinematic and dynamic system for the deviation attitude described by equations (4.19) and (4.20), one can assume the following change of variables:

$$
\begin{aligned}
&\boldsymbol{\eta} = \mathbf{z}_1 \quad ; \quad \boldsymbol{\xi} = \boldsymbol{\omega}_{ib}^{b} \quad ; \quad \mathbf{u} = \mathbf{u} \\
&\mathbf{f}(\boldsymbol{\eta},\boldsymbol{\xi}) = \frac{1}{2}\begin{bmatrix} \tilde{\mathbf{q}}_n^{T} \\ -\left(\tilde{q}_0\mathbf{I} + \mathbf{S}(\tilde{\mathbf{q}}_n)\right) \end{bmatrix}\boldsymbol{\omega}_{ib}^{b} \\
&\boldsymbol{\delta}_{\eta}(\boldsymbol{\eta},\boldsymbol{\xi}) = 0 \\
&\mathbf{f}_a(\boldsymbol{\eta},\boldsymbol{\xi}) = \bar{\mathbf{J}}^{-1}\left(\mathbf{S}(\bar{\mathbf{J}}\boldsymbol{\omega}_{ib}^{b})\boldsymbol{\omega}_{ib}^{b} - \bar{\mathbf{D}}_{\boldsymbol{\omega}}\boldsymbol{\omega}_{ib}^{b} + \mathbf{S}(\mathbf{R}_b^i\mathbf{F}_g)\bar{\mathbf{h}}_g\right) \\
&\mathbf{G}_a(\boldsymbol{\eta},\boldsymbol{\xi}) = \bar{\mathbf{J}}^{-1}\bar{\boldsymbol{\Phi}} \\
&\boldsymbol{\delta}_{\xi}(\boldsymbol{\eta},\boldsymbol{\xi},\mathbf{u}) = \boldsymbol{\delta}
\end{aligned}
\tag{4.23}
$$

The bar on the top of a term denotes an estimate of the property; this is the known value of model parameter but not necessarily the real value. The resulting kinematics and dynamics of the system with this new notation will be:

$$
\begin{aligned}
&\dot{\boldsymbol{\eta}} = \mathbf{f}(\boldsymbol{\eta},\boldsymbol{\xi}) + \boldsymbol{\delta}_{\eta}(\boldsymbol{\eta},\boldsymbol{\xi}) \\
&\dot{\boldsymbol{\xi}} = \mathbf{f}_a(\boldsymbol{\eta},\boldsymbol{\xi}) + \mathbf{G}_a(\boldsymbol{\eta},\boldsymbol{\xi})\left[\mathbf{u} + \boldsymbol{\delta}_{\xi}(\boldsymbol{\eta},\boldsymbol{\xi},\mathbf{u})\right]
\end{aligned}
\tag{4.24}
$$

Notice that the origin of the dynamic system (4.24) occurs when the vehicle has the desired body orientation ($\mathbf{q}^d$) and zero angular body velocity ($\boldsymbol{\omega}_{ib}{}^{b}$). It is trivial to conclude that (4.24) indeed matches equations (3.1) and (3.20), which were used to derive the ASMC and DSMC control laws in the previous chapter of this dissertation.

4.3.1. Analog sliding mode controller (ASMC)

Starting from a system written in its normal form, such as (4.24), the design of a robust analog sliding mode controller has three fundamental steps: choice of a robust

sliding manifold; describe the input that cancels the known dynamics of the system; and finally, define the upper boundaries for the model uncertainties that will be used as a lower bound for the attractor term of the input. This design procedure for the ASMC has already been presented in the previous chapter but will be given here using the JIAUV model.

We are interested in choosing a set of deviatory rotations that drive the $\mathbf{z_1}$ variable to its origin. Choosing a Lyapunov candidate function, as in (3.2), with the following form:

$$V = \mathbf{z}_1^T \mathbf{z}_1 \tag{4.25}$$

After differentiating (4.25) with respect to time one can obtain:

$$\dot{V} = 2\mathbf{z}_1^T \dot{\mathbf{z}}_1 = -\tilde{\mathbf{q}}_n^T \left(\mathbf{I} + \mathbf{S}(\tilde{\mathbf{q}}_n)\right) \boldsymbol{\omega}_{ib}^b \tag{4.26}$$

By assuming that the body rotation ($\boldsymbol{\omega}_{ib}{}^b$) could be chosen to be, with $\mathbf{K_1}$ being a diagonal gain matrix positive-definite:

$$\boldsymbol{\phi} = \boldsymbol{\omega}_{ib}^b = \left(\mathbf{I} + \mathbf{S}(\tilde{\mathbf{q}}_n)\right)^T \mathbf{K}_1 \tilde{\mathbf{q}}_n \tag{4.27}$$

The rate of the candidate Lyapunov function would then be:

$$\dot{V} = -\mathbf{K}_1 \tilde{\mathbf{q}}_n^T \tilde{\mathbf{q}}_n \leq 0 \tag{4.28}$$

The chosen form for the body rotation drives the system to stability. Asymptotic stability is not proven since the deviatory angle of rotation is unbounded by the Lyapunov rate. The boundedness of such a term arises from the unitary condition imposed on such vector. As a result, the relative angle of rotation could assume two possible values, plus or minus. In other words, the prescribed relation for the relative rotation would take the system to be oriented according to its desired orientation (plus) or according to the conjugate of the desired orientation (minus).

Based on such findings one can conclude that there is a region sufficiently close to the $\mathbf{z_1}$ origin ($[0\ 0\ 0\ 0]^T$) domain in which the system is asymptotically stable. At the same time there is another set of initial conditions that drives the system to another equilibrium position at $\mathbf{z_1} = [-2\ 0\ 0\ 0]^T$.

It was proved (eq. 4.27) that the choice of body rotation, based on deviatory quaternion feedback, stabilized the vehicle in the desired direction (but not necessarily in the desired orientation). This stable manifold will be considered for design purposes the

stable sliding hyperplane of this particular problem, *i.e.* the $\boldsymbol{\xi}$ trajectory that robustly stabilized the $\boldsymbol{\eta}$ dynamics as defined in chapter 3.

The variable (**s**) that tracks the difference between the stable manifold and the actual body rotations was defined by equation (3.3) and will be defined for this example as:

$$\mathbf{s} = \boldsymbol{\omega}_{ib}^{b} - \left(\mathbf{I} + \mathbf{S}(\tilde{\mathbf{q}}_{n})\right)^{T} \mathbf{K}_{1} \tilde{\mathbf{q}}_{n} \tag{4.29}$$

The time derivative of (4.29) can be expressed as in equation (3.24), which will correspond to the following:

$$\begin{aligned} \dot{\mathbf{s}} &= \bar{\mathbf{J}}^{-1}\left(\mathbf{S}(\bar{\mathbf{J}}\boldsymbol{\omega}_{ib}^{b})\boldsymbol{\omega}_{ib}^{b} - \bar{\mathbf{D}}_{\boldsymbol{\omega}}\boldsymbol{\omega}_{ib}^{b} + \mathbf{S}(\mathbf{R}_{b}^{i}\mathbf{F}_{g})\bar{\mathbf{h}}_{g}\right) \\ &+ \frac{1}{2}\left\{\left[(\mathbf{I} - \mathbf{S}(\tilde{\mathbf{q}}_{n}))\mathbf{K}_{1} + \mathbf{S}(\mathbf{K}_{1}\tilde{\mathbf{q}}_{n})\right]\left[\tilde{q}_{0}\mathbf{I} + \mathbf{S}(\tilde{\mathbf{q}}_{n})\right]\boldsymbol{\omega}_{ib}^{b}\right\} + \bar{\mathbf{J}}^{-1}\bar{\boldsymbol{\Phi}}\left(\mathbf{u} + \boldsymbol{\delta}\right) \end{aligned} \tag{4.30}$$

Choosing the following form for the input, as in (3.5):

$$\mathbf{u} = \left(\bar{\mathbf{J}}^{-1}\bar{\boldsymbol{\Phi}}\right)^{-1}\left\{\begin{array}{l} \mathbf{v} - \bar{\mathbf{J}}^{-1}\left(\mathbf{S}(\bar{\mathbf{J}}\boldsymbol{\omega}_{ib}^{b})\boldsymbol{\omega}_{ib}^{b} - \bar{\mathbf{D}}_{\boldsymbol{\omega}}\boldsymbol{\omega}_{ib}^{b} + \mathbf{S}(\mathbf{R}_{b}^{i}\mathbf{F}_{g})\bar{\mathbf{h}}_{g}\right) \\ -\frac{1}{2}\left\{\left[(\mathbf{I} - \mathbf{S}(\tilde{\mathbf{q}}_{n}))\mathbf{K}_{1} + \mathbf{S}(\mathbf{K}_{1}\tilde{\mathbf{q}}_{n})\right]\left[\tilde{q}_{0}\mathbf{I} + \mathbf{S}(\tilde{\mathbf{q}}_{n})\right]\boldsymbol{\omega}_{ib}^{b}\right\} \end{array}\right\} \tag{4.31}$$

Which results in the following tracking dynamics:

$$\dot{\mathbf{s}} = \mathbf{v} + \bar{\mathbf{J}}^{-1}\bar{\boldsymbol{\Phi}}\ \boldsymbol{\delta} = \mathbf{v} + \boldsymbol{\Delta} \tag{4.32}$$

The choice of input (**v**) that stabilizes the **s** dynamics takes the form described by equation (3.25) and will be:

$$\mathbf{v} = \frac{-\left(a_{1} + a_{2}\left\|\boldsymbol{\omega}_{ib}^{b}\right\|^{2} + a_{3}\left\|\boldsymbol{\omega}_{ib}^{b}\right\| + a_{0}\right)}{1 - \boldsymbol{\lambda}} sign\left(\boldsymbol{\omega}_{ib}^{b} - \left(\mathbf{I} + \mathbf{S}(\tilde{\mathbf{q}}_{n})\right)^{T}\mathbf{K}_{1}\tilde{\mathbf{q}}_{n}\right) \tag{4.33}$$

where a_0 is a positive scalar gain, λ belong to the interval [0,1) and together with a_i coefficients they are defined as:

$$\begin{aligned} a_{1} &\geq \left\|\mathbf{J}^{-1}\right\|_{\infty}\left\|\mathbf{F}_{g}\right\|_{\infty}\left|\left[\left\|\mathbf{h}_{g}\right\|_{\infty} - \left\|\boldsymbol{\Phi}\bar{\boldsymbol{\Phi}}^{-1}\right\|_{\infty}\left\|\bar{\mathbf{h}}_{g}\right\|_{\infty}\right]\right| \\ a_{2} &\geq \left\|\mathbf{J}^{-1}\right\|_{\infty}\left|\left[\left\|\mathbf{J}\right\|_{\infty} - \left\|\boldsymbol{\Phi}\bar{\boldsymbol{\Phi}}^{-1}\right\|_{\infty}\left\|\bar{\mathbf{J}}\right\|_{\infty}\right]\right| \\ a_{3} &\geq \left\|\mathbf{J}^{-1}\right\|_{\infty}\left|\left[\left\|\mathbf{D}_{\boldsymbol{\omega}}\right\|_{\infty} - \left\|\boldsymbol{\Phi}\bar{\boldsymbol{\Phi}}^{-1}\right\|_{\infty}\left\|\bar{\mathbf{D}}_{\boldsymbol{\omega}}\right\|_{\infty} - \frac{1}{2}\right]\right| \\ 0 \leq \boldsymbol{\lambda} &= \left|\left[\left\|\mathbf{J}^{-1}\right\|_{\infty}\left\|\boldsymbol{\Phi}\bar{\boldsymbol{\Phi}}^{-1}\right\|_{\infty}\left\|\bar{\mathbf{J}}\right\|_{\infty} - 1\right]\right| < 1 \end{aligned} \tag{4.34}$$

The definitions given by equation (4.34) are a result of the upper boundary defined by the uncertainties in equation (3.26), which correspond to the p-∞ norm of the uncertainties vector (**Δ**). An improvement on this control law is achieved by substituting the signum function on eq. (4.33) by the saturation function. Such function is represented by figure 4.9.

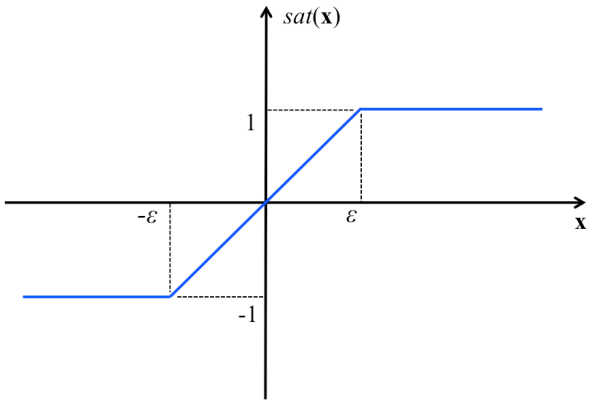

Figure 4.9. Illustration of the saturation function, where ε is a positive real number. The operation of this function on a vector corresponds the operation over each element.

This saturation function introduces the boundary layer effect when transitioning between the different sliding mode controller structures as described by [69] eliminating the chattering.

4.3.2. Digital sliding mode controller (DSMC)

In this subsection, not only the discrete sliding mode controller will be derived for the JIAUV model being dealt with, but also the system itself will be presented in a discrete format. The entire process requires the application of Taylor-Lie discretization procedure, followed by the choice of a robust discrete sliding hyperplane with both lower and upper bound restrictions. The final steps in the procedure is to choose the feedback law to cancel all the known discrete dynamics and choose an attractor term to drive the system to a quasi-sliding mode of operation.

Starting from the system (4.24) one can apply the Taylor-Lie discretization procedure as described in section 3.2 and 3.3 in the last chapter and obtain the discrete model:

$$\begin{aligned}\boldsymbol{\eta}^{k+1} &= \boldsymbol{\eta}^{k} + \mathbf{f}^{D}(\boldsymbol{\eta}^{k},\boldsymbol{\xi}^{k},T_s) + \boldsymbol{\delta}_{\boldsymbol{\eta}}^{D}(\boldsymbol{\eta}^{k},\boldsymbol{\xi}^{k},T_s)\\ \boldsymbol{\xi}^{k+1} &= \boldsymbol{\xi}^{k} + \mathbf{f}_{a}^{D}(\boldsymbol{\eta}^{k},\boldsymbol{\xi}^{k},T_s) + \mathbf{G}_{a}^{D}(\boldsymbol{\eta}^{k},T_s)\left[\mathbf{u}^{k} + \boldsymbol{\delta}_{\boldsymbol{\xi}}^{k}(\boldsymbol{\eta}^{k},\boldsymbol{\xi}^{k},\mathbf{u}^{k})\right] + \boldsymbol{\delta}^{D}(\boldsymbol{\eta}^{k},\boldsymbol{\xi}^{k},\mathbf{u}^{k},T_s)\end{aligned} \tag{4.35}$$

where, for a second order discrete approximation (N=2) each term is defined as:

$$\begin{aligned}&\boldsymbol{\eta}^{k} = \mathbf{z}_1^{k};\quad \boldsymbol{\xi}^{k} = \boldsymbol{\omega}_{\mathrm{ib}}^{\mathrm{b}^k};\quad \mathbf{u}^{k} = \mathbf{u}^{k}\\ &\mathbf{f}^{D}(\boldsymbol{\eta}^{k},\boldsymbol{\xi}^{k},T_s) = T_s\mathbf{f}^{k} + L_{\mathbf{f}}\mathbf{f}^{k}\frac{T_s^2}{2!}\\ &\boldsymbol{\delta}_{\boldsymbol{\eta}}^{D}(\boldsymbol{\eta}^{k},\boldsymbol{\xi}^{k},T_s) = 0\\ &\mathbf{f}_{\mathrm{a}}^{D}(\boldsymbol{\eta}^{k},\boldsymbol{\xi}^{k},T_s) = T_s\mathbf{f}_{a}^{k} + L_{\mathbf{f}_a}\mathbf{f}_{a}^{k}\frac{T_s^2}{2!}\\ &\mathbf{G}_{\mathrm{a}}^{D}(\boldsymbol{\eta}^{k},T_s) = T_s\mathbf{G}_{a}^{k} + L_{\mathbf{G}_a^k}\mathbf{f}_{a}^{k}\frac{T_s^2}{2!}\\ &\boldsymbol{\delta}^{D}(\boldsymbol{\eta}^{k},\boldsymbol{\xi}^{k},\mathbf{u}^{k},T_s) = L_{\mathbf{f}_a+\mathbf{G}_a^k(\mathbf{u}^k+\boldsymbol{\delta}_{\boldsymbol{\xi}}^k)}\mathbf{G}_{a}^{k}\boldsymbol{\delta}_{\boldsymbol{\xi}}^{k}\frac{T_s^2}{2!}\end{aligned} \tag{4.36}$$

The vector/matrix properties masked with a superscript k are the same as the ones described equation (4.23) but evaluated at the k^{th} time step. The operator L corresponds to a Lie derivative. These derivatives were computed to be:

$$L_{\mathbf{f}}\mathbf{f}^{k} = \frac{\partial\mathbf{f}^{k}}{\partial\mathbf{z}_1}\mathbf{f}^{k} = \frac{\partial\mathbf{f}^{k}}{\partial\mathbf{z}_1}\frac{1}{2}\begin{bmatrix}\left(\tilde{\mathbf{q}}_n^{k}\right)^{\mathrm{T}}\boldsymbol{\omega}_{\mathrm{ib}}^{\mathrm{b}^k}\\ -\left[\tilde{q}_0^{k}\mathbf{I} + \mathbf{S}(\tilde{\mathbf{q}}_n^{k})\right]\boldsymbol{\omega}_{\mathrm{ib}}^{\mathrm{b}^k}\end{bmatrix} \tag{4.37.a}$$

$$\frac{\partial\mathbf{f}^{k}}{\partial\mathbf{z}_1} = \frac{1}{2}\begin{bmatrix}0 & \left(\boldsymbol{\omega}_{\mathrm{ib}}^{\mathrm{b}^k}\right)^{\mathrm{T}}\\ -\boldsymbol{\omega}_{\mathrm{ib}}^{\mathrm{b}^k} & \mathbf{S}(\boldsymbol{\omega}_{\mathrm{ib}}^{\mathrm{b}^k})\end{bmatrix}_{4\times4} \tag{4.37.b}$$

$$L_{\mathbf{f}_a}\mathbf{f}_{a}^{k} = \frac{\partial\mathbf{f}_{a}^{k}}{\partial\boldsymbol{\omega}_{\mathrm{ib}}^{\mathrm{b}^k}}\mathbf{f}_{a}^{k} = \frac{\partial\mathbf{f}_{a}^{k}}{\partial\boldsymbol{\omega}_{\mathrm{ib}}^{\mathrm{b}^k}}\bar{\mathbf{J}}^{-1}\left(\mathbf{S}(\bar{\mathbf{J}}\boldsymbol{\omega}_{\mathrm{ib}}^{\mathrm{b}})\boldsymbol{\omega}_{\mathrm{ib}}^{\mathrm{b}} - \bar{\mathbf{D}}_{\boldsymbol{\omega}}\boldsymbol{\omega}_{\mathrm{ib}}^{\mathrm{b}} + \mathbf{S}(\mathbf{R}_{\mathrm{b}}^{\mathrm{i}}\mathbf{F}_{\mathrm{g}})\bar{\mathbf{h}}_{g}\right) \tag{4.38.a}$$

$$\frac{\partial\mathbf{f}_{a}^{k}}{\partial\boldsymbol{\omega}_{\mathrm{ib}}^{\mathrm{b}}} = \bar{\mathbf{J}}^{-1}\left(\mathbf{S}(-\boldsymbol{\omega}_{\mathrm{ib}}^{\mathrm{b}})\bar{\mathbf{J}} + \mathbf{S}(\bar{\mathbf{J}}\boldsymbol{\omega}_{\mathrm{ib}}^{\mathrm{b}}) - \bar{\mathbf{D}}_{\boldsymbol{\omega}}\right) \tag{4.38.b}$$

$$L_{\mathbf{f}_a+\mathbf{G}_a^k(\mathbf{u}^k+\boldsymbol{\delta}_{\boldsymbol{\xi}}^k)}\mathbf{G}_{a}^{k}\boldsymbol{\delta}_{\boldsymbol{\xi}} = \frac{\partial\mathbf{G}_{a}^{k}\boldsymbol{\delta}_{\boldsymbol{\xi}}}{\partial\boldsymbol{\omega}_{\mathrm{ib}}^{\mathrm{b}^k}}\mathbf{f}_{a} + \mathbf{G}_{a}^{k}(\mathbf{u}^{k} + \boldsymbol{\delta}_{\boldsymbol{\xi}}^{k}) \tag{4.39.a}$$

$$\frac{\partial\mathbf{G}_{a}^{k}\boldsymbol{\delta}_{\boldsymbol{\xi}}}{\partial\boldsymbol{\omega}_{\mathrm{ib}}^{\mathrm{b}^k}} = -\bar{\mathbf{J}}^{-1}\left(\mathbf{S}(-\boldsymbol{\omega}_{\mathrm{ib}}^{\mathrm{b}})\bar{\mathbf{J}} + \mathbf{S}(\bar{\mathbf{J}}\boldsymbol{\omega}_{\mathrm{ib}}^{\mathrm{b}}) - \bar{\mathbf{D}}_{\boldsymbol{\omega}}\right) + \mathbf{J}^{-1}\left(\mathbf{S}(-\boldsymbol{\omega}_{\mathrm{ib}}^{\mathrm{b}})\mathbf{J} + \mathbf{S}(\mathbf{J}\boldsymbol{\omega}_{\mathrm{ib}}^{\mathrm{b}}) - \mathbf{D}_{\boldsymbol{\omega}}\right) \tag{4.39.b}$$

Finally condition (3.15) for the stability of the discrete system can be written as:

$$\mathbf{f}^{D^{\mathrm{T}}}\left[2\mathbf{z}_1^k+\mathbf{f}^D\right]<0 \tag{4.40}$$

Substituting the discrete dynamic vector (**f**) described in eq. (4.36) into this previous relation one can get (recalling the unity condition for quaternions defined by eq. (4.4):

$$T_s\left[\left(\boldsymbol{\omega}_{\mathrm{ib}}^{\mathrm{b}}\right)^{\mathrm{T}}\boldsymbol{\omega}_{\mathrm{ib}}^{\mathrm{b}}\right]\left[T_s^2\left(\boldsymbol{\omega}_{\mathrm{ib}}^{\mathrm{b}}\right)^{\mathrm{T}}\boldsymbol{\omega}_{\mathrm{ib}}^{\mathrm{b}}+16\tilde{q}_0\right]<64\tilde{\mathbf{q}}_n^{\mathrm{T}}\boldsymbol{\omega}_{\mathrm{ib}}^{\mathrm{b}} \tag{4.41}$$

Choosing the following feedback relation to the body rotations:

$$\boldsymbol{\phi}^k=\boldsymbol{\omega}_{\mathrm{ib}}^{\mathrm{b}^k}=\frac{b_1}{T_s}\left(\mathbf{I}+\mathbf{S}(\tilde{\mathbf{q}}_n^k)\right)^{\mathrm{T}}\tilde{\mathbf{q}}_n^k \tag{4.42}$$

As a result the gain b_1 has to satisfy the following relation:

$$\left(1-\left(\tilde{q}_0^k\right)^2\right)\left[b_1^3\left(1-\left(\tilde{q}_0^k\right)^2\right)+16b_1\tilde{q}_0^k-64\right]<0 \tag{4.43}$$

Equation (4.43) is always satisfied if b_1 is smaller then 4. This result reflects the upper bound limit for the sliding manifold imposed by the system discretization, as discussed in chapter 3 of this dissertation. It is critical to notice that such upper bound on the design of the sliding manifold does not exist for the ASMC case.

The variable ($\mathbf{s}^k$) that tracks the difference between the stable manifold and the actual body rotations was defined by equation (3.16) and will be defined for this example as:

$$\mathbf{s}^k=\boldsymbol{\omega}_{\mathrm{ib}}^{\mathrm{b}^k}-\frac{b_1}{T_s}\left(\mathbf{I}+\mathbf{S}(\tilde{\mathbf{q}}_n^k)\right)^{\mathrm{T}}\tilde{\mathbf{q}}_n^k \tag{4.44}$$

The future difference (k+1) from the $\boldsymbol{\xi}^k$ state and the sliding manifold ($\boldsymbol{\phi}^k$) can be calculated as:

$$\mathbf{s}^{k+1}=\boldsymbol{\omega}_{\mathrm{ib}}^{\mathrm{b}^{k+1}}-\boldsymbol{\phi}^{k+1}=\boldsymbol{\xi}^k+\mathbf{f}_a^D+\mathbf{G}_a^D\left[\mathbf{u}^k+\boldsymbol{\delta}_{\boldsymbol{\xi}}^k\right]+\boldsymbol{\delta}^D-\frac{b_1}{T_s}\left(\mathbf{I}+\mathbf{S}(\tilde{\mathbf{q}}_n^{k+1})\right)^{\mathrm{T}}\tilde{\mathbf{q}}_n^{k+1} \tag{4.45}$$

Following equation (3.18) the control law that eliminates the known terms in the discrete system is:

$$\mathbf{u}^k=\mathbf{G}_a^D(\boldsymbol{\eta}^k,T_s)^{-1}\left[-\mathbf{f}_a^D(\boldsymbol{\eta}^k,\boldsymbol{\xi}^k,T_s)-\boldsymbol{\phi}^k(\boldsymbol{\eta}^k,T_s)+\boldsymbol{\phi}^{k+1}(\boldsymbol{\eta}^k+\mathbf{f}(\boldsymbol{\eta}^k,\boldsymbol{\xi}^k),T_s)+\mathbf{v}^k\right] \tag{4.46}$$

After substituting (4.46) into (4.45) one can get:

$$\mathbf{s}^{k+1}=\mathbf{s}^k+\mathbf{v}^k+\mathbf{G}_a^D\boldsymbol{\delta}_{\boldsymbol{\xi}}^k+\boldsymbol{\delta}^D=\mathbf{s}^k+\mathbf{v}^k+\boldsymbol{\Delta}^k \tag{4.47}$$

Notice that because the system being dealt with is simpler then the one presented in chapter 3 the form of the discrete uncertainties vector is much simpler then the one presented by (3.31). The goal is to define an input $\mathbf{v}^k$ that satisfy condition (3.30). Since no generic form for the discrete attractor term can be derived without knowledge on the uncertainty the one proposed by (3.19) will be used:

$$\mathbf{v}^k = -b_0 \mathbf{s}^k = -b_0 \left[\boldsymbol{\omega}_{\mathrm{ib}}^{\mathrm{b}^k} - \frac{b_1}{T_s} \left(\mathbf{I} + \mathbf{S}(\tilde{\mathbf{q}}_n^k) \right)^{\mathrm{T}} \tilde{\mathbf{q}}_n^k \right] \tag{4.48}$$

where b_0 is positive scalar number that is less then 2.

The use of equation (4.48) as the attractor term by the DSMC admits the existence of a quasi-sliding mode on the dynamic system, that is, it only guarantees the reaching of a neighboring region of the sliding manifold, as demonstrated in appendix C.5.

4.4. Simulations and comparison between different control architectures

This section focuses on the numerical simulation of a jellyfish-inspired autonomous underwater vehicle under the influence of different attitude controllers. The block diagram given by figure 4.8 is a close representation of the feedback being implemented (the forward swimming portion was dropped out to simplify the analysis of the attitude controller performance).

Three different control architectures are being directly tested and compared in this section of the dissertation: ASMC with continuous implementation; ASMC with discrete implementation; and DSMC (specifically designed controller for discrete implementation). All feedback relationships are based on the measured attitude and body angular velocity and where described in detail in the previous section of this chapter.

The goal in all simulation is to start from a straight attitude (with the z^b axis matching the z^i) and achieve an orientation of 45º-pitch angle, *i.e.* a rotation of 45º around the y^b axis in the clock-wise direction. All the controllers are given a mathematical model that has slightly different model parameter then the actual model being controlled. This procedure allows the simulations to infer the robustness of the control strategy being implemented for JIAUV. The properties given to the controllers are described in detail by appendix D.

The first virtual test assumes that the vehicle input can continuously be changed based on the analog measurements of the vehicle's angular states (orientation and body angular rotations). The analog sliding mode control law is the one used to drive the vehicle, *i.e.* choose the input based on the angular states. Figure 4.10 presents the resulting attitude of the vehicle and the choice of inputs created by the controller that drove the system. The controller gains are: $\mathbf{K_1}=2\mathbf{I}$, $a_0=1$, $a_i=0.001$ ($i=1,2,3$), $\lambda=0.05$ and $\varepsilon=0.01$.

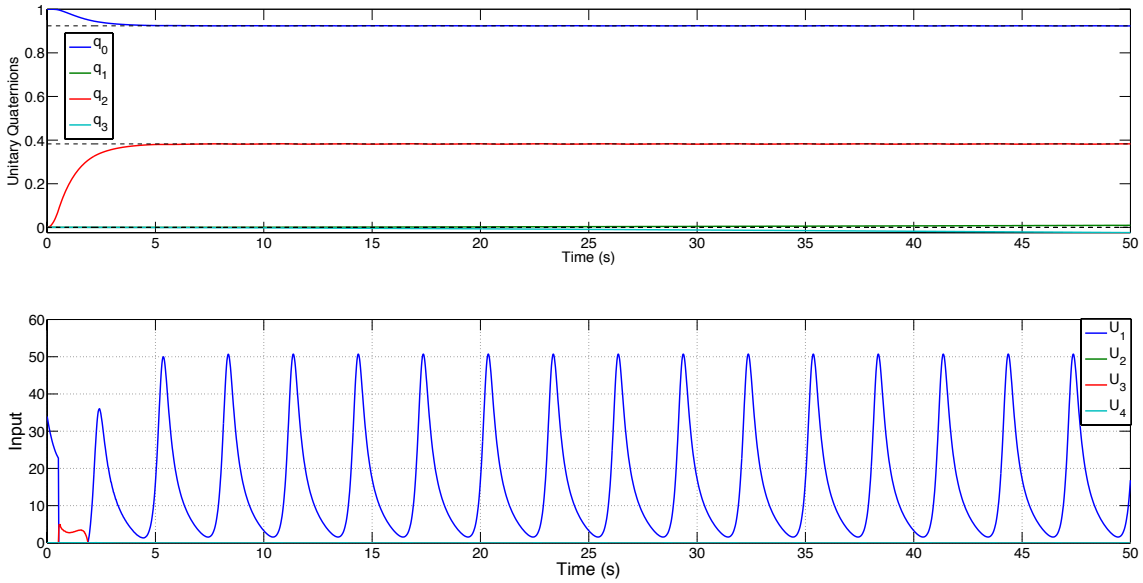

Figure 4.10. JIAUV response and input under ASMC with continuous implementation.

Because the mathematical model used in the controller design incorporates the pulsating behavior of the JIAUV the resulting input also follows this T-periodic motion. The resulting attitude obtained matched the desired orientation very well despite the fact that the model given to the controller has slightly different model parameters then the one being simulated. Figure 4.10 is the demonstration that an ASMC controller under continuous-time implementation can, indeed, drive the JIAUV to any desired orientation.

Commonly these control laws are implemented using a microcontroller, a system that only allows for a discrete implementation, due to the need of sampling and processing of the data in the digital domain. A common practice among engineers is to ignore this discretization process and implement the laws derived for a continuous system

and implement them in a discrete fashion. Figure 4.11 is the discrete implementation of the same ASMC law. In the discrete implementation a new input can only be applied to the system after waiting a sampling period (T_s), meanwhile the same input is still applied to the system. The controller gains are kept the same as the ones used in the previous example.

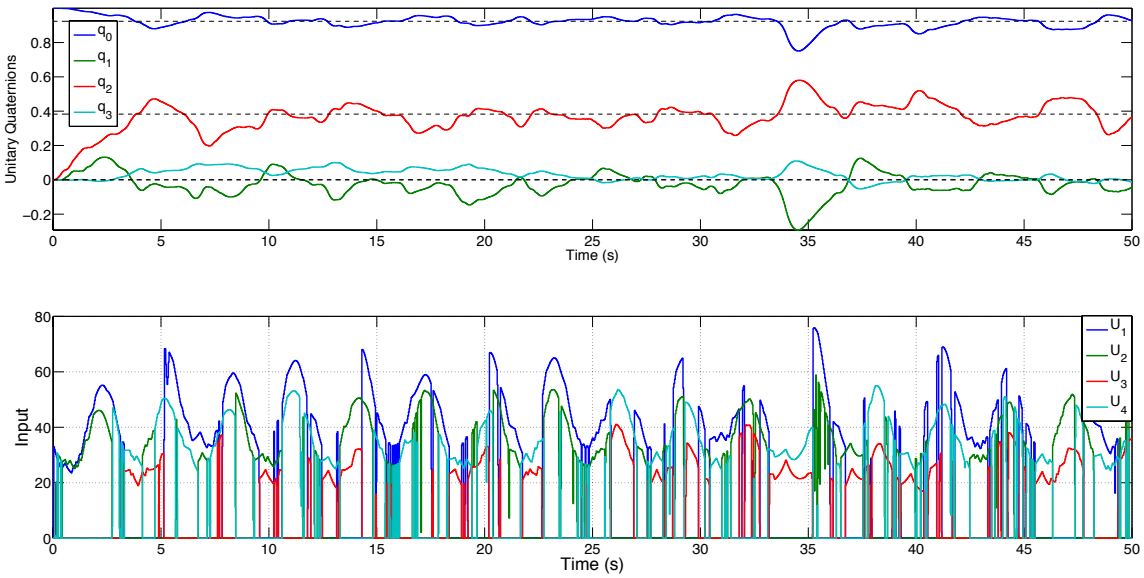

Figure 4.11. JIAUV response and input under ASMC with discrete implementation (sampling period of 0.03 s) – with same gains as in figure 4.10.

It is evident the decay in the controller performance although one can still say that the vehicle reached the vicinity of the desired orientation and is oscillating about it. The input itself also presents chattering, even though the saturation function is being used to smooth the transition between different control structures. A simple solution is to adjust the controller gains, particularly the a_0 gain that drives the attractor component of the control law. Figure 4.12 has the controlled system response of the discrete implementation of the ASMC law only reducing the attractor gain (a_0) in two orders of magnitude, to 0.01.

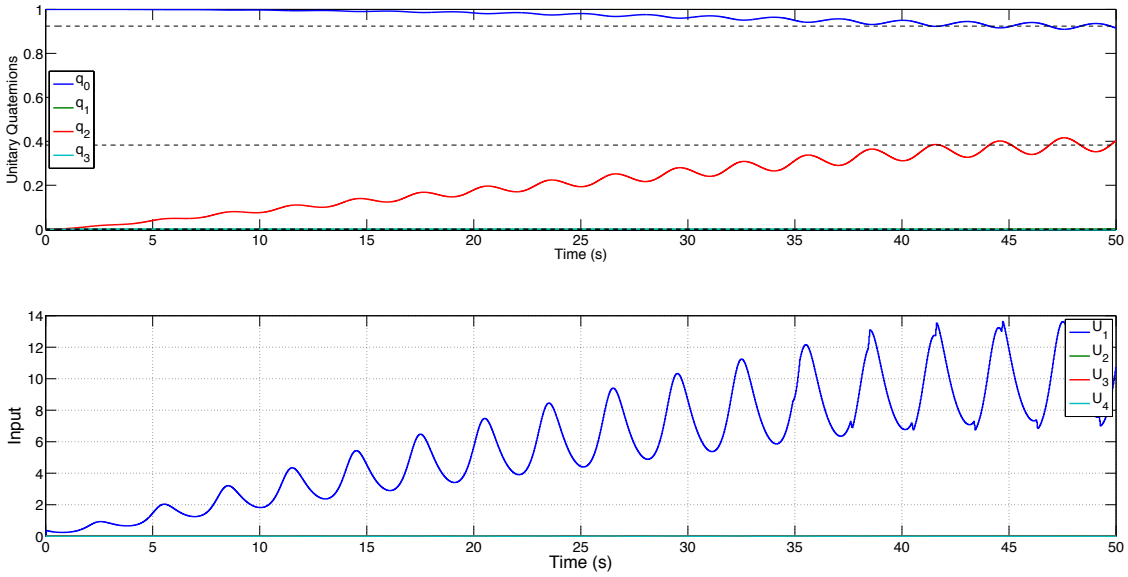

Figure 4.12. JIAUV response and input under ASMC with discrete implementation (sampling period of 0.03 s) – with a_0=0.01.

For the discrete implementation of the ASMC law shown above the desired attitude was reached, but it is evident that the performance of the controller decayed when compared to the analog implementation (figure 4.11), not only did it take longer to achieve the desired orientation but also more importantly the vehicle oscillated about that angular position. On the other hand the magnitude of the control inputs is much lower, which can be directly related to the amount of the energy that has to be supplied to the system. It is evident that the magnitude of the controller gains plays a significant role in the stability of the ASMC control law when discretely implemented and such fact is not evident in the design of the control law.

Even for low gains the ASMC can drive the JIAUV to instability if the sampling time is large enough. Figure 4.13 corresponds to a control simulation identical to the one performed for figure 4.12 but with a sampling time of 0.3 seconds.

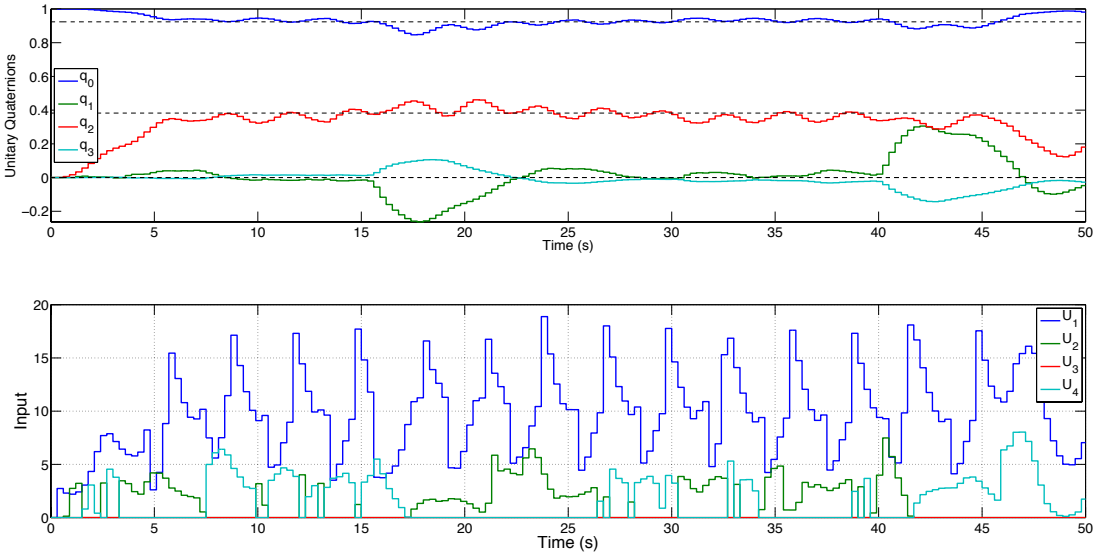

Figure 4.13. JIAUV response and input under ASMC with discrete implementation (sampling period of 0.3 s) – with a_0=0.01.

Although the desired attitude was obtained in the beginning (from 5 to 10 s), soon the control law created some unstable behavior (from 15 to 20 s), which after a while drove the system to complete instability (after 40 s). It should be clear at this point that the discrete implementation of a control law derived for a continuous system can drive the system to an unstable behavior. Hence, it is necessary to develop appropriate design tools for the discrete systems to avoid poor controller performance as demonstrated by figure 4.13.

The digital sliding mode control law proposed by this dissertation addresses this issue by presenting a controller design methodology that incorporates the effects of the discretization which directly results in upper bound limits for the controller gains. Figure 4.14 is the resulting attitude and the input history created by a DSMC on a JIAUV using a second order approximation of the discrete model. The controller gains used are: b_1=0.1 and b_0=0.2.

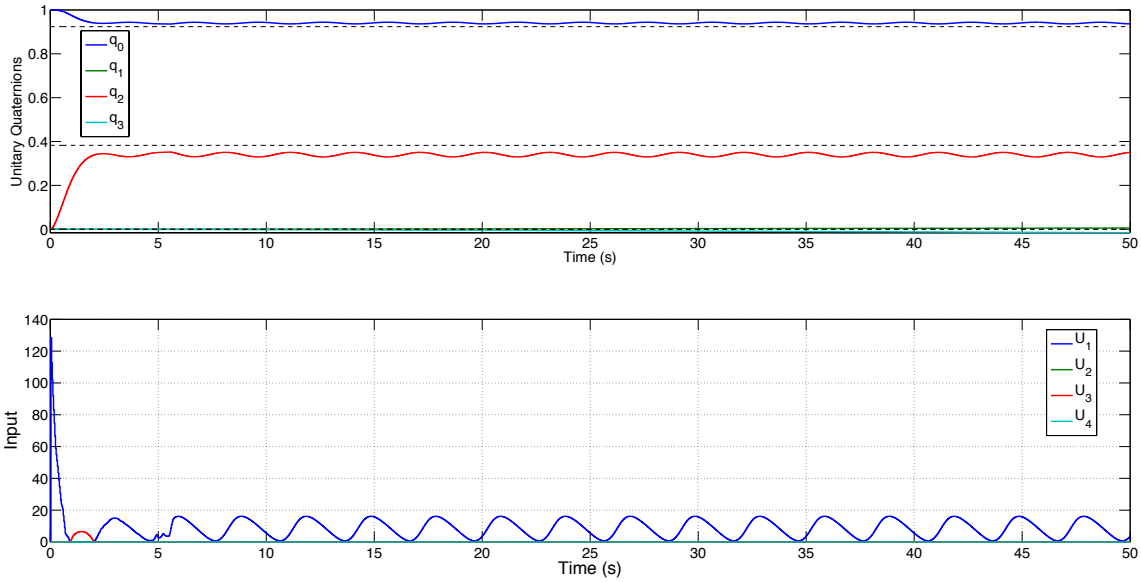

Figure 4.14. JIAUV response and input under DSMC (sampling period of 0.03 s).

The controller is indeed capable of driving the system to an orientation near the one specified (marked by the dotted lines). By comparing the response of the DSMC (figure 4.14) and the ASMC with discrete implementation and the same sampling time (figure 4.12) it is possible to state that both reaching and residual oscillation of the controlled attitude were improved by the use of the DSMC. Also the amplitude of the input when the desired position is reached is much smaller for the DSMC when compared to the ASMC with continuous time implementation. This last statement has implication on the energy required by the controller to keep the vehicle at a certain orientation, which for the DSMC is smaller.

It is also important to notice that there is a steady-state error between desired and final attitude on figure 4.14. This small mismatch is being caused by the approximations made during the discretization step of the design process. As presented in the previous section of this chapter a second order discrete model was used in the derivations of the control law. A simple verification of such phenomenon is to repeat the same DSMC simulation with a higher sampling period, this should increase this steady-state error of the controller, and figure 4.15 presents such test.

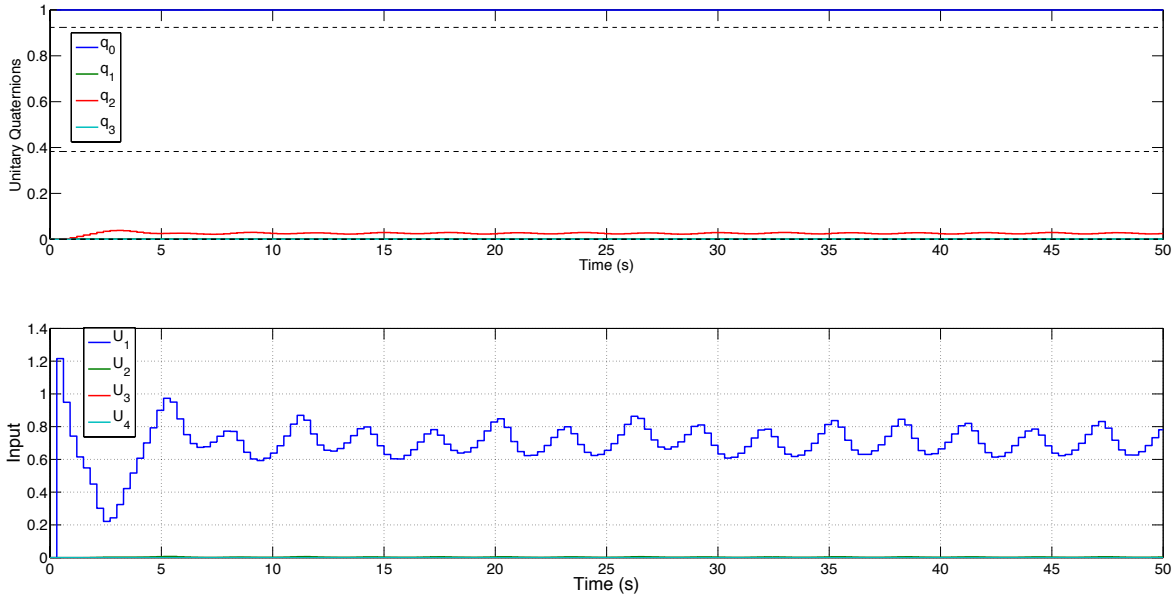

Figure 4.15. JIAUV response and input under DSMC (sampling period of 0.3 s).

The increase in sampling time for the DSMC indeed increased the steady-state error of the controller, revealing that the second order discrete approximation of the model is not sufficient to capture the dynamics of the system at such sampling period. Based on the desired sampling period the order of the discrete model must be chosen to accurately represent the system dynamics that will ultimately improve the DSMC performance.

While the increase in the sampling period caused system instabilities for the ASMC approach (figure 4.13) for the DSMC this unstable behavior was not observed (figure 4.15). By eliminating the possibility of attitude instabilities the designer increases the system reliability since no energy will be wasted in driving the vehicle.

A very interesting application for the DSMC is to match the controller sampling time with the resonant beating frequency of the vehicle itself, which would implicate (mathematically) in the cancelation of all time-varying components of the model. This matching DSMC application would also require a periodic function generator to drive the vehicle in between sampling times (the amplitude of this function at every period is determined by the control law). Such approach would result in a reduction o processing

by the onboard microcontroller since sensor data sampling and controller calculations would only occur at the beginning of each beating period.

Energy storage is a recurring issue in any AUV application and a controller that performs more efficiently is desired. In that sense, the DSMC proved it to be a better choice then the ASMC (with continuous implementation), since the amplitude of the input chosen by the controller is significantly smaller, a parameter that can be directly correlated to the power used consumed by the system.

In summary, this chapter illustrated the application of feedback, model-based attitude controllers in a bio-inspired autonomous underwater vehicle (jellyfish-like). Besides exemplifying the use of the control theory presented in the third chapter the author also compared three different implementations: continuous ASMC, discrete ASMC and DSMC.

5. Conclusions

The purpose of this dissertation is to provide and discuss a generic framework for the control of bio-inspired autonomous underwater vehicle (BIAUV). These nature-inspired systems have been the focus of a large number of recent research efforts in order to improve the performance of underwater exploratory vessels. One of the most distinguished and generic characteristics of BIAUV is the use of body oscillation to produce a net thrust in a desired direction, *e.g.* a fish-like vehicle that oscillates its tail to move forward. It then becomes extremely important to incorporate and discuss this unique feature of a BIAUV into the controller design process in order to take full advantage of the higher capabilities of these bio-inspired systems.

The first chapter of this document presents a complete discussion on the terminology and techniques used in this dissertation by distinguishing, for example, a traditional autonomous underwater vehicle (AUV) design from a bio-inspired one or a model-based from a non-model-based controller, etc. This initial chapter presents the reasoning of why some research directions were pursued throughout this work while other very interesting and important research areas, such as more accurate fluid-structure interaction model, high-level controllers, other controller design techniques, where not considered.

When it comes to the control of these bio-inspired underwater vehicles there are many questions to be answered, but most of them are specific to the type of vehicle being dealt with and few are generic enough to be applied across an entire category of vessels. Among the few generic questions is one related to which variable on the oscillatory motion of the propulsor should one aim to control in order to maximize the vehicle efficiency? To answer such a question it is necessary to develop a model that is able to capture the most basic features of such physical phenomenon: the motion of a flexible structure immersed in water and the subsequent transfer of kinetic energy into the surrounding fluid which promotes an unsteady water flow.

The coupled fluid-structure model of a vibrating beam submersed into Newtonian fluid developed in the second chapter is a simple description of the basic features of a bio-inspired propulsor allowing engineers to make inferences over such a propulsion

mechanism. Along with several limitations imposed to the fluid behavior during modeling, the structural dynamics was also constrained, all to reveal the most basic physical principles that drive the energy exchange between both domains. The final coupled model assumes that the fluid is incompressible, Newtonian, two-dimensional (no flow velocities or gradients on the z-direction) and the flow velocity is the same as the beam's velocity in the interface between domains. Structurally a viscously damped Euler-Bernoulli beam is assumed to represent the mechanical system dynamics.

The single most important simplification carried throughout this chapter is that the structural vibration mode shapes, $X_i(x)$, are not affected by the interactions between domains. This hypothesis was experimentally tested and shown to be reasonable for the first three modes, as pointed out by figure 2.5. Besides being a common assumption throughout models in literature [58], there is experimental evidence that such hypothesis could be valid for lower mode shapes of beams [43].

In contrast to the coupled models presented in literature [47] [60] the approach taken here does not discard the damping like terms from the fluid momentum equation, *i.e.* Navies-Stokes equation. This approach allows for an understanding of how energy is permanently transferred between both domains. The model also capture's a cyclical energy exchange, in terms of an added inertia that reduced the combined system's natural frequency.

Interpreting this fluid-induced damping terms through a structural perspective is an intuitive way to interpret the resulting model. While mass and stiffness are conservative properties of a vibrating system, *i.e.* the energy flow between these properties without leaving the system, damping is a non-conservative property that changes the overall system energy. Commonly researchers are not interested in defining how the energy is leaving structural system or where it is going, an approach that leads to a lumped damping term that just captures the overall energy extraction/addition behavior. In contrast, the model proposed here, equations (2.11) and (2.12), has a breakdown of the energy extracted from the oscillatory solid structure into two new terms, one of which related to existence of an adjacent fluid media.

A deeper analysis on the fluid-induced energy transport sheds light on the most basic physical principles of this phenomenon and the role of each fluid property. For

instance, the damping term associated with fluid viscosity relies on velocity gradients to exist, a typical characteristic of a diffusion mechanism.

The fact that the resonant frequency is reduced when there is coupling between both domains is not just a conclusion based on the model but an experimental fact [43]. There are two possible explanations for this reduction: it is either caused by a stiffness reduction or by an inertia increase, the latter being the most plausible explanation. Equation (2.14) describes a key parameter in the model that represents the volume of fluid around the structure affected by the beam motion and, consequently, the added inertia. Experimental results in water show that this value is constant and independent of the mode shape.

Observation also suggests that the lower modes are responsible for higher energy transfers across domains due to the larger absolute fluid effect on damping ratio displayed on table 2.4. The data also suggest that the energy transmission is deeply related to the mode shape, increasing its relative impact for higher modes as illustrated on figure 2.7.

Considering that the experiments carried out provided sufficient proof that the proposed model can somehow capture the FSI phenomenon the fourth section of the second chapter introduces a calculation technique to predict the thrust (eq. 2.21) and lift (eq. 2.20) production by the oscillatory motion of the structure under a sinusoidal force input (eq. 2.22). Figure 2.9 illustrates the force profile produced by such mechanical excitation; it is interesting to notice that no average lift is being produced while there is a positive average thrust force created.

Now that an evaluation tool has been developed for a simple (representative) bio-inspired propulsor it is possible to investigate the effects of the different control variables over the resulting thrust forces produced. The input in such a model is given by the applied force, equation (2.22), indicating that there are three possible controllable parameters: the position x where the force is applied, the force amplitude (A_s) and the frequency (f). Because actively changing the position where the force is being applied would require a complex mechanism this variable will not be treated here as a control parameter. To illustrate such idea imagine a system the can actively reposition its actuator connections or have multiple actuators along the propulsor, such system would be highly

complex and would fall into a much more specific type of system then the generic one being dealt with in this dissertation.

By treating only the amplitude and frequency as control parameters, figure 2.10 plots the resulting thrust generated when both are changed. It is important to notice that the thrust force scales with the square of the input amplitude while, for the frequency, a complex scaling law is observed. Interestingly the peaks in thrust production occur at the natural frequencies of the FSI problem described, this fact is a result of the constructive interference between the force being applied and the coupled response of the fluid-structure system. The phenomenon previously described is commonly known in literature as resonance and it could be explored in order to maximize constructive interactions between input and response.

The fifth section on the second chapter presents the mathematical foundations for the existence of resonant behavior in an arbitrary dynamical system. By the presented definition there are three fundamental requirements: the dynamics system has to respond with a wave-like behavior, and the input has to match the frequency and format of the wave-like response. Although these conditions seem trivial they restrict in many ways the inputs to the system that can produce resonance. The nature of the system itself is also limited since it has to have wave-like response, but for bio-inspired propulsor this assumption is quite reasonable since in both the structural and fluids domain (disregarding turbulent flows) this is an expected comportment.

In order to improve the controlled system's performance it is crucial to keep it operating under resonance. This requirement constrains the choice of a control variable suitable to drive the BIAUV, thus for this type of system, amplitude will be the most adequate choice of control parameter since, as demonstrated by figure 2.10, the input frequency can directly affect the occurrence of resonance. Although the conclusion drawn here only applies directly to the FSI problem developed in chapter 2, they can somehow be extended to a generic BIAUV system due to the fact that everything was derived to capture the most basic underlying physical phenomena and it should represent (in a simplistic way) any other complex problem.

Now that a control variable was chosen in order to keep the BIAUV operating in resonance conditions it becomes necessary to move the discussion to another topic of interest while developing a control framework for BIAUV: the design of a model-based feedback law. This relationship between the current measured state of the vehicle and what action it should perform in order to achieve a desired state is a decision making process that relies on the designer knowledge of the system to guarantee that any given command will be properly executed. The knowledge of the system is interpreted as a mathematical model that describes the system behavior under the action of an arbitrary input and such model can be used in the process of designing the controller for the vehicle.

Among the model-based controller design techniques, sliding mode controller (SMC) is a very useful technique, since it allows for the design of control laws of a system that has nonlinearities and it is also characterized by its robustness, by making use of variable structure in the control law.

Two different sliding mode control techniques for continuous-time systems were presented in the third chapter, the analog and discrete version of the SMC. Although the analog sliding mode controller (ASMC) is a well-established concept in literature [71] [72], it was presented here so a direct comparison with the proposed discrete sliding mode controller (DSMC) technique could be made.

The definition of an appropriate discrete control law for the continuous nonlinear system (equation 3.1) starts by performing a Taylor-Lie series expansion of the original system followed by a mathematical manipulation that results in the discrete approximate representation of the original system (equation 3.12). Obtaining this representation of the dynamic system is the first step towards achieving a DSMC and it is an important contribution of this dissertation.

A sufficient condition for the stability of the sliding manifold in these discrete systems was proposed in this chapter (eq. 3.14), based on a Lypunov-type of functional. The use of this discrete stability analysis technique is key to guarantee the convergence of the state to the equilibrium point. This approach imposes a magnitude upper bound into the design of the stable manifold due to the discretization process (eq. 3.15). The

existence of this upper bound while designing a sliding mode controller in the discrete domain has not been presented in literature so far, being a concept of extreme importance while implementing these laws using a microcontroller.

A discrete feedback control law was proposed in order to guarantee the reaching and sliding on the stable hyperplane of the nonlinear dynamic system, the technique is referred to as digital sliding mode control (DSMC). The DSMC feedback law proposed here (equation 3.18) is clearly different than the traditional ASMC law (equation 3.5) specially when it comes to the attractor terms of each technique (equations 3.6 and 3.19).

Robustness considerations were addressed in section 3.3 by invoking model structured uncertainties. A lower bound restriction on the sliding manifold design was added into both analog and digital SMC laws to improve the controlled system robustness. A robust DSMC requires more information on the structured uncertainties once a lower and upper bound have to be satisfied simultaneously, equations (3.27) and (3.30).

An interesting observation is the growth of the uncertainties within the discretized model representation, such observation have been taken into account by other authors [70] and has been the reasoning behind using ASMC on discrete systems.

Finally a benchmark example used to illustrate the proposed approach. A second order nonlinear dynamic system was presented and both ASMC (eq. 3.37) and DSMC (eq. 3.40) were derived. Numerical simulations were conducted to ensure that the stability was achieved for both control strategies.

This study extends the work developed by Furuta [85] by proposing a discrete sliding mode control law for a multivariable nonlinear system. Although similar sufficient conditions have been derived for the existence of such a control law for nonlinear systems [88], the Lyapunov-based approach taken here allows for an easy extension of the concept to a multivariable system. The inclusion of the discretization effects on the controller design is another important contribution of the work presented here and so far has not been reported in literature for the SMC technique.

Finally the proposed DSMC technique for continuous-time nonlinear systems can be described in three steps: first, a Taylor-Lie discretization of the continuous-time system; second, a choice of an appropriate sliding manifold that satisfies the sufficient

condition (3.15); and finally, a choice of attractor, equation (3.19). This systematic procedure and the concept development required to achieve this DSMC law are a major scientific contribution of this dissertation.

To illustrate the concepts discussed in the first three chapters of this dissertation it becomes necessary to carryout an example that illustrates the concepts developed for BIAUV. The fourth chapter present kinematic, dynamic and thrust models to adequately represent a jellyfish-inspired autonomous underwater vehicle (JIAUV). By combining these models a complete mathematical relation is obtained between the inputs to the vehicle and the resulting position and orientation in the underwater environment. This complete vehicle model captures the most basic characteristics of the JIAUV, such as, stable orientation, positive relative weight (it sinks), pulsating swimming behavior, etc. The thrust model, equations (4.10) and (4.11), adds to the vehicle model a time-varying component that is characteristic of the BIAUV [27] and it is described in terms of an amplitude control variable in order to guarantee that the vehicle is operating in its propulsion resonant condition thus increasing the overall system efficiency.

Because of the nature of the JIAUV the control architecture has to be modified to take into account for the capabilities of the vehicle. To address the rowing propulsion limitations a turn-and-go strategy was proposed. The idea is to orient the vehicle (via an attitude controller) to a desired final destination and once the vehicle satisfies this desired orientation a forward swimming algorithm takes over and propels the vehicle into the z^b direction. A block diagram of the proposed architecture is given by figure 4.8. In order to track if the current attitude matches the commanded (desired) one, a new variable is described, called the deviatory attitude, and its dynamics is also given.

The design of the attitude sliding mode controllers for the JIAUV is given in the third section of the fourth chapter, where the complete dynamic model of the vehicle is properly manipulated to assume the form required by eq. (3.1) and (3.20) to start the design process. The analog design process starts by defining the stable sliding manifold (eq 4.27) and is followed by defining a feedback law that cancel the known dynamics (eq. 4.31). The last step is to design the SMC attractor that has to be greater then the leftover system uncertainties (eq. 4.33). The system attractor defined by eq. (4.33) is modified to

allow a smooth transition between different control structures by substituting the signum function for a saturation function.

The digital design process is slightly different than the analog one, since it starts by performing the Taylor-Lie discretization process of the complete vehicle model. In the example carried out in chapter four a second order approximation is used to represent the original system dynamics. This choice of approximation has direct implications on the final controlled performance. The choice of a stable sliding manifold (eq. 4.42) is immediately followed by the determination of an upper boundary for the manifold (eq. 4.43). A feedback law is also chosen to eliminate all the known dynamics of the systems (eq. 4.46) and the attractor term is also selected (eq. 4.48). Because there exists uncertainties the design of a discrete attractor becomes a real challenge once it has to satisfy simultaneously the upper bound (from the discretization process) and the lower bound (from the uncertainties). Since there is not a lot of knowledge on the uncertainties this lower bound is ignored, resulting in a quasi-sliding operating mode, a concept widely described and accepted for discrete implementation of sliding mode controllers [81].

To access the robustness of the control law derived the model parameters, provided to the attitude controller, were slightly different than the ones used in the simulation to represent the actual vehicle. Not only the time variation of these properties were dropped out, but also, all off-diagonal terms in the matrices were considered to be zero. The comparison between these properties can be found on appendix D of this document.

The continuous implementation of the ASMC law, figure 4.10, proved itself to be a robust controller to drive the system to a desired orientation. On the other hand this method requires a specific circuitry to sense and analogically drive the input to the vehicle. Such a law is commonly implemented in discrete time steps as illustrated by figure 4.11 and, in such condition, the controller performance significantly decays. A simple solution is to promote a gain reduction on the controller, a restriction that was not part of the analog theory of sliding mode controllers. Such action results in a satisfactory performance of the controller (figure 4.12) but is evident that it took longer for the system to reach the neighborhood of the desired orientation. A direct comparison between the inputs applied by the ASMC with continuous and discrete implementation reveals that in

the discrete case the overall input amplitude is much lower. In some sense the input amplitude can be directly correlated to the energy consumed by the system. By increasing the sampling time on the discrete implementation it is possible to observe some unstable behavior of the ASMC implementation. This phenomenon is undesirable since energy is spent driving the system away from the desired attitude.

To avoid the occurrence of instabilities while discretely driving the system the DSMC design technique was developed, derived and implemented in this dissertation. The result was presented by figure 4.14, where the reaching time was improved when compared to the discrete ASMC implementation and the overall input amplitude was significantly reduced when compared to the continuous ASMC implementation. One of the main drawbacks of the technique is the number of terms used in the Taylor-Lie series to approximate the discrete system, since they cause a steady-state error in the reaching performance of the DSMC. The existence of such effect is clearly seen when the sampling time is increased, figure 4.15, where the steady-state error significantly increases. There are two solutions for this problem, decrease the sampling time or increase the number of terms in the Taylor-Lie series.

Despite the steady-state error drawback the DSMC technique did not drive the system to unstable behavior and that is an important benefit of the proposed technique when compared to the to the established ASMC. Not only the reaching performance was superior (comparing figures 4.12 and 4.14) but no energy would be wasted with unstable behaviors (comparing figure 4.13 and 4.15).

In summary this dissertation provided a generic framework for the robust, model-based, nonlinear control of bio-inspired autonomous underwater vehicle by discussing and providing scientific contributions in three topics:

- The input variable should be chosen in such way that the BIAUV operates under its resonance condition to maximize thrust production.
- An appropriate nonlinear, model-based, robust, discrete design controller technique was proposed based on the sliding mode control theory.
- A jellyfish-inspired autonomous underwater vehicle was modeled and a controller was derived for such system allowing for the exemplification of the framework proposed.

References

[1] National Oceanic and Atmospheric Administration, *Ocean size*. <www.noaa.gov/ocean.html> Accessed in April 2013.

[2] National Oceanic and Atmospheric Administration, *Ocean depth*. <oceanservice.noaa.gov/facts/oceandepth.html> Accessed in April 2013.

[3] S.J. Dick, K.L. Cowing, *Risk and exploration earth, sea and the stars*. Technical report, NASA (2004).

[4] J. Heerwagen, *Bio-inspired design bio-inspired design. What can we learn from nature?* Technical report, HAWORTH (2010).

[5] A.J. Murphy, M. Haroutunian, *Using bio-inspiration to improve capabilities of underwater vehicles*. Technical report, School of Marine Science and Technology, Newcastle University (2011).

[6] J.P. Breslin, A. Poul, *Hydrodynamics of Ship Propellers*. Cambridge University Press, Cambridge (1993).

[7] F. Liu, K.-M. Lee, C.-J. Yang, *Hydrodynamics of an undulating fin for a wave-like locomotion system design*. IEEE/ASME Transactions on Mechatronics (2012), pp. 17(3):554–562.

[8] R.M. Berry, J.P. Armitage, *The bacterial flagella motor*. Advances in Microbial Physiology, Academic Press (1999), pp. 41:291–337.

[9] Autonomous Undersea Vehicle Application Center, *Comprehensive search on AUV platforms*. <auvac.org/explore-database/simple-search> Accessed in April 2013.

[10] M. Philen, W. Neu, *Hydrodynamic analysis, performance assessment, and actuator design of a flexible tail propulsor in an artificial alligator*. Smart Materials and Structures (2011), pp. 20(9):094015.

[11] D.S. Barrett, M.S. Triantafyllou, D.K.P. Yue, M.A. Grosenbaugh, M.J. Wolfgang, *Drag reduction in fish-like locomotion*. Journal of Fluid Mechanics (1999), pp. 392:183–212.

[12] M. Rufo, *Ghostswimmer: Tactically relevant, biomimetically inspired, silent, highly efficient and maneuverable autonomous underwater vehicle*. Technical report, Boston Engineering Corporation (2012).

[13] W. Stoll, *Aquapenguin*. Technical report, FESTO (2009).

[14] R.Y. Siegwart, *NARO tartaruga project and its technical description*, <http://www.naro.ethz.ch/p2/tartaruga.html> Accessed in April 2013.

[15] EvoLogics Bionic Laboratory, *Subsea glider with Fin-Ray Effect: overview and technical description*, <www.evologics.de/en/products/glider/index.html> Accessed in April 2013.

[16] A. Villanueva, C. Smith, S. Priya, *A biomimetic robotic jellyfish (robojelly) actuated by shape memory alloy composite actuators*. Bioinspiration and Biomimetics (2011), pp. 6(3):036004.

[17] K.T. Frandsen, H.U. Riisgard, *Size dependent respiration and growth of jellyfish, Aurelia aurita*. Sarsia (1997), pp. 82(4):307–312.

[18] J.O. Dabiri, S.P. Colin, J.H. Costello, M. Gharib, *Flow patterns generated by oblate medusan jellyfish: field measurements and laboratory analyses*. Journal of Experimental Biology (2005), pp. 208(7):1257–1265.

[19] A. Bjerrum, *Technology and Applications of Autonomous Underwater Vehicles: AUVs For Surveys In Complex Environments*. CRC press (2002), pp. 203–215.

[20] A.J. Healey, D. Lienard, *Multivariable sliding mode control for autonomous diving and steering of unmanned underwater vehicles*. IEEE Journal of Oceanic Engineering (1993), pp. 18(3):327–339.

[21] F. Garcia-Cordova, A. Guerrero-Gonzalez, *A biologically inspired neural network for autonomous underwater vehicles*. Advances in Computational Intelligence, Lecture Notes in Computer Science, Springer Berlin Heidelberg (2011), pp. 6691:166–173.

[22] S.M. Smith, G.J.S. Rae, D.T. Anderson, *Applications of fuzzy logic to the control of an autonomous underwater vehicle*. Second IEEE International Conference on Fuzzy Systems (1993), pp. 2:1099–1106.

[23] D.R. Yoerger, J.G. Cooke, J. J. E. Slotine, *The influence of thruster dynamics on underwater vehicle behavior and their incorporation into control system design*. IEEE Journal of Oceanic Engineering (1990), pp. 15(3):167–178.

[24] M. Loueipour, H. Hadian, *Effect of considering sensors and actuators modeling on the design of pid controllers for an autonomous underwater vehicle*. 2nd

International Conference on Control, Instrumentation and Automation (2011), pp. 582–587.

[25] J. Palmisano, J. Geder, R. Ramamurti, K.-J. Liu, J. Cohen, T. Menge-sha, J. Naciri, W. Sandberg, B. Ratna, *Design, development, and testing of flapping fins with actively controlled curvature for an unmanned underwater vehicle*. Bio-mechanisms of Swimming and Flying, Springer Japan (2008), pp. 283–294.

[26] G. Barbera, L. Pi, X. Deng, A*ttitude control for a pectoral fin actuated bio-inspired robotic fish*. IEEE International Conference on Robotics and Automation (2011), pp. 526–531.

[27] A.J. Ijspeert, A. Crespi, D. Ryczko, J.-M. Cabelguen, *From swimming to walking with a salamander robot driven by a spinal cord model*. Science (2007), pp. 315(5817):1416–1420.

[28] K. Seo, S.-J. Chung, J.-J. E. Slotine, *CPG-based control of a turtle-like underwater vehicle*. Autonomous Robots (2010), pp. 28(3):247–269.

[29] C. Zhou, K.H. Low, *Design and locomotion control of a biomimetic underwater vehicle with fin propulsion*. IEEE/ASME Transactions on Mechatronics (2012), pp. 17(1):25–35.

[30] E. Kartashova, *Nonlinear Resonance Analysis:. Theory, Computation, Applications*. Cambridge University Press (2010).

[31] M. Mchenry, C. Pell, J. Jr, *Mechanical control of swimming speed: stiffness and axial wave form in undulating fish models*. Journal of Experimental Biology (1995), pp. 198(11):2293–2305.

[32] H.K. Khalil, *Nonlinear systems*. Prentice Hall (2002).

[33] T.L.M. Bartelt, *Industrial Automated Systems: Instrumentation and Motion Control*. Delmar Cengage Learning (2010).

[34] S. Boyd, *Lecture notes from EE102: Introduction to signals and systems at Stanford university, 1993*. <http://www.stanford.edu/~boyd/ee102/> Accessed in April 2013.

[35] F. Dougherty, T. Sherman, G. Woolweaver, G. Lovell, *An autonomous underwater vehicle (AUV) flight control system using sliding mode control*.

Proceedings from the partnership of marine interests - OCEANS'88 (1988), pp. 4:1265–1270.

[36] P.-M. Lee, C.-M. Lee, B.-H. Jeon, S.-W. Hong, Y.-K. Lim, J.-W. Park, J.-S. Lee, *System design and quasi-sliding mode control of an AUV for ocean research and monitoring*. Proceedings of the 1998 International Symposium on Underwater Technology (1998), pp. 179–184.

[37] A.F. Filippov, *Differential equations with discontinuous right-hand side*. Matematicheskii Sbornik (1960), pp. 51(93):99–128.

[38] K. Craig, *Digital implementation of control – Online PDF*. <http://multimechatronics.com/images/uploads/mech_n/Digital_Implementation_of_Control.pdf> Accessed on February 2013.

[39] M.J. Lighthill, *Large-Amplitude Elongated-Body Theory of Fish Locomotion*. Proceedings of the Royal Society of London. Series B. Biological Sciences (1971), pp. 179:125-138.

[40] Lord Rayleigh, *Theory of Sound (volume I)*. Dover Publications, New York (1877).

[41] Lord Rayleigh, *Theory of Sound (volume II)*. Dover Publications, New York (1878).

[42] T.Y.-T. Wu, *Swimming of a waving plate*. Journal of Fluid Mechanics (1961), pp. 10:321-344.

[43] U.S. Lindholm, D.D. Kana, W.H. Chu, H.N. Abramson, *Elastic Vibration Characteristics of Cantilever Plates in Water*. Journal of Ship Research (1965), pp. 9:11-22.

[44] T.L. Geers, *Residual potential and approximate methods for three-dimensional fluid-structure interaction problems*. Journal of the Acoustic society of America (1971), pp. 49:1505–1510.

[45] M.G. Chopra, *Large amplitude lunate-tail theory of fish locomotion*. Journal of Fluid Mechanics (1976), pp. 74:161–182.

[46] J. Katz, D. Weihs, *Hydrodynamic propulsion by large amplitude oscillation of an airfoil with chordwise flexibility*. Journal of Fluid Mechanics (1978), pp. 88:485–497.

[47] M.R. Haddara, S. Cao, *A study of the dynamic response of submerged rectangular flat plates*. Journal of Marine Structures (1996), pp. 9:913–933.

[48] Y. Fu, W.G. Price, *Interactions between a partially or totally immersed vibrating cantilever plate and the surrounding fluid*. Journal of Sound and Vibration (1987), pp. 118:495–513.

[49] D. Maity, S.K. Bhattacharyya, *A parametric study on fluid-structure interaction problems*. Journal of Sound and Vibration (2003), pp. 263:917–935.

[50] G.J. Dong, X.Y. Lu, *Numerical analysis on the propulsive performance and vortex shedding of fish-like travelling wavy plate*. International Journal for Numerical Methods in Fluids (2005), pp. 48:1351–1373.

[51] T. Tezduyar, S. Sathe, K. Stein, L. Aureli, *Modeling of Fluid-Structure Interactions with the Space-Time Techniques*. Lecture Notes in Computational Science and Engineering (2006), pp. 53:50–81.

[52] S. Alben, *Simulating the dynamics of flexible bodies and vortex sheets*. Journal of Computational Physics (2009), pp. 228:2587–2603.

[53] B. Ugurlo, A. Ergin, *A hydroelasticity method for vibrating structures containing and/or submerged in flowing fluid*. Journal of Sound and Vibration (2006), pp. 290:572–596.

[54] C. Atkinson, M. Manrique de Lara, *The frequency response of a rectangular cantilever plate vibrating in a viscous fluid*. Journal of Sound and Vibration (2007), pp. 300:352–367.

[55] Y. Kerboua, A.A. Lakis, M. Thomas, L. Marcouiller, *Vibration analysis of rectangular plates coupled with fluid*. Applied Mathematical Modeling (2008), pp. 32:2570–2586.

[56] W. Zhao, M.P. Paidoussis, L. Tang, M. Liu, J. Jiang, *Theoretical and experimental investigations of the dynamics of cantilevered flexible plates subjected to axial flow*. Journal of Sound and Vibration (2012), pp. 331:575–587.

[57] L. Tang, M. P. Paidoussis, J. Jiang, *Cantilevered flexible plates in axial flow: Energy transfer and the concept of flutter-mill*. Journal of Sound and Vibration (2009), pp. 326:263–276.

[58] A. Ergin, B. Ugurlo, *Linear vibration analysis of cantilever plates partially submerged in fluid*. Journal of Fluids and Structures (2003), pp. 17:927–939.

[59] D.J. Inman, *Engineering Vibration*, Prentice Hall, Upper Saddle River, NJ, 3rd edition (2008).

[60] R.P.S. Han, H. Xu, *A simple and accurate added mass model for hydrodynamic fluid-Structure interaction analysis*. Journal of the Franklin Institute (1996), pp. 333:929–945.

[61] C.P. Vendhan, Y.C. Das, *Application of Rayleigh-Ritz and Galerkin methods to non-linear vibration of plates*. Journal of Sound and Vibration (1975), pp. 39:147–157.

[62] D.J. Ewins, *Modal Testing: Theory, Practice, and Application*. Research Studies Press, Philadelphia, PA, 2nd edition (2000).

[63] L. Ott, M. Longnecker, *An Introduction to Statistical Methods and Data Analysis*. Duxbury Press, Pacific Groove, CA. 6th edition (2008).

[64] V.I. Utkin, *Variable structure systems with sliding modes*. IEEE Transactions on Automatic Control (1977), pp. 22(2):212-222.

[65] V.I. Utkin, *Sliding mode and its application to variable structure systems*. Moscow: Mir (in Russian) (1978).

[66] A. Pisano, E. Usai, *Sliding mode control: A survey with applications in math*. Mathematics and Computers in Simulation (2011), pp. 81(5):954-979.

[67] P.A. Karnazes, R.D. Bonnell, *Variable structure control of linear systems*. IEEE Southeastcon Region 3 Conference on Electricity and Expanding Technology, New York, USA (1975).

[68] U. Itkis, *Control systems of variable structure*. John Wiley & Sons, 1st ed., Manchester (1976).

[69] J.-J.E. Slotine, S.S. Sastry, *Tracking control of non-linear systems using sliding surfaces, with application to robot manipulators*. International Journal of Control (1983), pp. 38(2):465-492.

[70] J.-J.E. Slotine, *Sliding controller design for non-linear systems*. International Journal of Control (1984), pp. 40(2):421-434.

[71] J.-J.E. Slotine, W. Li, *Applied Nonlinear Control*. Prentice Hall, 1st ed. New Jersey (1991).

[72] A.S.I. Zinober, *Variable structure and Lyapunov control*. Springer-Verlag, 1st ed., London (1994).

[73] H. Elmali, N. Olgac, *Satellite attitude control via sliding mode with perturbation estimation*. IEEE Proceedings of Control Theory and Applications (1996), pp. 276-282.

[74] R. Martinez-Guerra, R. Aguilar, A. Poznyak, *A new robust sliding-mode observer design for monitoring in chemical reactors*. Journal of Dynamic Systems, Measurement and Control (2004), pp. 126(3):473-478.

[75] X. Li, W. Yu, *Neural sliding mode control for magnetic levitation systems*. Proceedings of the IEEE International Conference on Control Applications, (2010), pp. 615-619.

[76] G. Ping, J.-C. Li, X.-H. Liu, *Fuzzy sliding mode control of the arc furnace electrode regulator system*. Proceedings of the World Congress on Intelligent Control and Automation (2010), pp. 4932-4936.

[77] H. Liu, T. Zhang, *Fuzzy sliding mode control of robotic manipulators with kinematic and dynamic uncertainties*. Journal of Dynamic Systems, Measurement and Control (2012), pp. 134(6):1-10.

[78] T. Madani, A. Benallegue, *Sliding mode observer and backstepping control for a quadrotor unmanned aerial vehicles*. Proceedings of the American Control Conference (2007), pp. 5887-5892.

[79] D. Jiang, Z. Zhao, F. Wang, *A Sliding Mode Observer for PMSM speed and rotor position considering saliency*. Power Electronics Specialists Conference (2008), pp. 809-814.

[80] H. Hashimoto, K. Maruyama, F. Harashima, *A Microprocessor-Based Robot Manipulator Control with Sliding Mode*. IEEE Transactions on Industrial Electronics (1987), pp. 11-18.

[81] C. Milosavljevic, *General conditions for the existence of a quasi-sliding mode on the switching hyperplane in discrete variable structure systems*. Automatic Remote Control (1985), pp. 46(3):307-314.

[82] S. Sarpturk, Y. Istefanopulos, O. Kaynak, *On the stability of discrete-time sliding mode control systems*. IEEE Transactions on Automatic Control (1987), pp. 32(10):930-932.

[83] K. Furuta, *Sliding mode control of a discrete system*. Systems and Amp Control Letters (1990), pp. 14(2):145-152.

[84] W. Gao, Y. Wang, A. Homaifa, *Discrete-time variable structure control systems*. IEEE Transactions on Industrial Electronics (1995), pp. 42(2):117-122.

[85] W.-C. Su, S.V. Drakunov, U. Ozguner, *An O(T2) boundary layer in sliding mode for sampled-data systems*. IEEE Transactions on Automatic Control (2000), pp. 45(3):482-485.

[86] Y. Zheng, G.M. Dimirovski, Y. Jing, M. Yang, *Discrete-Time Sliding Mode Control of Nonlinear Systems*. American Control Conference (2007) pp.3825- 3830.

[87] H. Sira-Ramirez, *Non-linear discrete variable structure systems in quasi-sliding mode*. International Journal of Control (1992), pp. 54(5):1171-1187.

[88] N. Kazantzis, K.T. Chong, J.H. Park, A.G. Parlos, *Control-Relevant Discretization of Nonlinear Systems With Time-Delay Using Taylor-Lie Series*. Journal of Dynamic Systems, Measurement, and Control (2005), pp. 127(1):153-159.

[89] J. Yuh, *Design and control of autonomous underwater robots: a survey*. Autonomous Robots (2000), pp. 8:7-24.

[90] B.P. Epps, P. Valdivia y Alvarado, K. Youcef-Toumi, A.H. Techet, *Swimming performance of a biomimetic compliant fish-like robot*. Experiments in Fluids (2009), pp. 47(6):927-939.

[91] J. Palmisano, R. Ramamurti, K.J. Lu, J. Cohen, W. Sandberg, B. Ratna, *Design of a biomimetic controlled-curvature robotic pectoral fin*. IEEE International Conference on Robotics and Automation (2007), pp.966-973.

[92] T. Fukuda, H. Hosokai, I. Kikuchi, *Distributed type of actuators by shape memory alloy and its application to underwater mobile robotic mechanism*. IEEE International Conference on Robotics and Automation (1990), pp. 2:1316-1321.

[93] S. Guo, T. Fukuda, N. Kato, K. Oguro, *Development of underwater microrobot using ICPF actuator*. IEEE International Conference on Robotics and Automation (1998), pp. 2:1829-1834.

[94] Y. Nagata, P. Seokyong, M. Aiguo, M. Shimojo, *Development of underwater robot using Macro Fiber Composite*. IEEE/ASME International Conference on Advanced Intelligent Mechatronics (2008), pp. 955-960.

[95] J. Najem, S.A. Sarles, B. Akle, D.J. Leo, *Biomimetic jellyfish-inspired underwater vehicle actuated by ionic polymer metal composite actuators*. Smart Materials and Structures (2012), pp. 21(9):094026-094037.

[96] M.J. McHenry, J. Jed, *The ontogenetic scaling of hydrodynamics and swimming performance in jellyfish (Aurelia aurita)*. The Journal of Experimental Biology (2003), pp. 206:4125-4137.

[97] S. Guo, L. Shi, X. Ye, L. Li, *A New Jellyfish Type of Underwater Microrobot*. International Conference on Mechatronics and Automation (2007), pp. 509-514.

[98] FESTO, *AquaJelly: An artificial jellyfish with electric drive unit, 2008*. <http://www.festo.com/cms/en_corp/9772_10378.htm#id_10378> Accessed on February 2013.

[99] S.-W. Yeom, I.-K. Oh, *A biomimetic jellyfish robot based on ionic polymer metal composite actuators*. Smart Materials and Structures (2009), pp. 18(8):085002-085012.

[100] S. Nir, I. Ruchaevski, S. Shraga, T. Shteinberg, B. Moshe, *A jellyfish-like robot for mimicking jet propulsion*. Convention of Electrical Electronics Engineers in Israel (2012), pp. 1-5.

[101] F.-C. Chiu, J. Guo, J.-G. Chen, Y.-H. Lin, *Dynamic characteristic of a biomimetic underwater vehicle*. International Symposium on Underwater Technology (2002), pp. 172-177.

[102] D.P. Brutzman, *A virtual world for an autonomous underwater vehicle*. PhD dissertation, Naval Postgraduate School (1994).

[103] R. Kristiansen, P.J. Nicklasson, J.T. Gravdahl, *Satellite Attitude Control by Quaternion-Based Backstepping*. Transactions on Control Systems Technology (2009), pp. 17(1):227-232.

Appendix A

Assuming that the beam motion could be represented using separation of variables as described by equation (2.1). The beam velocity is easily calculated by applying a time derivative over the beam displacement:

$$\frac{\partial y_b(x,t)}{\partial t} = X_i(x)\frac{\partial T_i(t)}{\partial t} = X_i(x)\dot{T}_i(t) \tag{A.1}$$

The boundary conditions chosen consider that the flow around the beam will have the beam *y*-velocity over the interface and at infinity the beam does not affect the flow velocity. These boundary conditions where illustrated in figure 2.2 and are mathematically described as:

$$\begin{aligned} v(x,0,t) &= \frac{\partial y_b}{\partial t} \\ v(x,+\infty,t) &= 0 \\ v(x,-\infty,t) &= 0 \end{aligned} \tag{A.2}$$

Each side of the beam is classified as a region: an upper region on the positive side of the y-axis (denoted by a superscript plus sign) and a lower region on the negative y-axis (denoted by a superscript minus sign). Assuming that the flow y-velocity over the beam has an exponential form as described by equation (2.2) and applying the boundary conditions at each side of the beam the resulting velocity fields are given by equation (2.3). Now that the vertical velocity field is defined for the problem, the horizontal velocity can be determined by using the continuity equation defined by equation (2.4). Knowing the vertical velocity field and assuming that the partial derivatives can be converted to full derivatives due to the separation of variables assumption, the following equation has to be solved:

$$\int_{-\infty}^{x} du = \int_{-\infty}^{x} \frac{\partial v}{\partial y} dx \tag{A.3}$$

Assuming that an infinite distance before the leading edge the flow is not affected by the beam and integrating to an arbitrary point *x* in the fluid field one can have for each fluid region the horizontal velocities as described by equations (2.5). By knowing the velocity fields the balance of momentum (Navier-Stokes equation) can be applied for the *y*-direction, *i.e.* equation (2.6). For the upper side of the beam (positive *y*-region) the balance becomes:

$$\rho\left[X_i\ddot{T}_i e^{-\sigma y}+\left(\sigma\dot{T}_i e^{-\sigma y}\int_{-\infty}^{x}X_i\,dx\right)X'_i\dot{T}_i e^{-\sigma y}-\sigma\left(X_i\dot{T}_i e^{-\sigma y}\right)^2\right]=\frac{-\partial P^+}{\partial y}+\mu\left(X''_i+\sigma^2X_i\right)\dot{T}_i e^{-\sigma y}$$

$$\frac{\partial P^+}{\partial y}=\left\{\left[\mu\left(X''_i+\sigma^2X_i\right)\right]\dot{T}_i-\rho X_i\ddot{T}_i\right\}e^{-\sigma y}-\rho\sigma\dot{T}_i^2\left(X'_i\int_{-\infty}^{x}X_i\,dx-X_i^2\right)e^{-2\sigma y}$$

$$\frac{\partial P^+}{\partial y}=f(x,t)e^{-\sigma y}-g(x,t)e^{-2\sigma y} \tag{A.4}$$

Applying the same procedure to the lower side of the beam:

$$\rho\left[X_i\ddot{T}_i e^{\sigma y}+\left(-\sigma\dot{T}_i e^{-\sigma y}\int_{-\infty}^{x}X_i\,dx\right)X'_i\dot{T}_i e^{-\sigma y}+\sigma\left(X_i\dot{T}_i e^{-\sigma y}\right)^2\right]=\frac{-\partial P^-}{\partial y}+\mu\left(X''_i+\sigma^2X_i\right)\dot{T}_i e^{\sigma y}$$

$$\frac{\partial P^-}{\partial y}=\left\{\left[\mu\left(X''_i+\sigma^2X_i\right)\right]\dot{T}_i-\rho X_i\ddot{T}_i\right\}e^{\sigma y}+\rho\sigma\dot{T}_i^2\left(X'_i\int_{-\infty}^{x}X_i\,dx-X_i^2\right)e^{2\sigma y}$$

$$\frac{\partial P^-}{\partial y}=f(x,t)e^{\sigma y}+g(x,t)e^{2\sigma y} \tag{A.5}$$

Now assuming that in both sides of the beam there is an equal "ambient" pressure at an infinite distance:

$$P_\infty=P_\infty^+=P_\infty^+ \tag{A.6}$$

Converting the pressure gradient described in eqs. (A.4) to a total derivative and integrating over the domain one can get the following for the upper side of the beam:

$$\int_{P^+}^{P_\infty}dP=f(x,t)\int_{0^+}^{+\infty}e^{-\sigma y}\,dy-g(x,t)\int_{0^+}^{+\infty}e^{-2\sigma y}\,dy$$

$$P_\infty=P^++f(x,t)\frac{1}{\sigma}-g(x,t)\frac{1}{2\sigma} \tag{A.7}$$

Again the same operation can be done for the lower side:

$$\int_{P^-}^{P_\infty}dP=f(x,t)\int_{0^-}^{-\infty}e^{\sigma y}\,dy-g(x,t)\int_{0^-}^{-\infty}e^{2\sigma y}\,dy$$

$$P_\infty=P^--f(x,t)\frac{1}{\sigma}-g(x,t)\frac{1}{2\sigma} \tag{A.8}$$

Applying equations (A.7) and (A.8) back into (A.6) yields:

$$P^--f(x,t)\frac{1}{\sigma}-g(x,t)\frac{1}{2\sigma}=P^++f(x,t)\frac{1}{\sigma}-g(x,t)\frac{1}{2\sigma}$$

$$P^- - P^+ = f(x,t)\frac{2}{\sigma}$$

$$P^- - P^+ = \Delta P = \frac{2}{\sigma}\left[\mu\left(X''_i + \sigma^2 X_i\right)\right]\dot{T}_i - \frac{2\rho}{\sigma}X_i\ddot{T}_i \tag{A.9}$$

Equation (A.9) corresponds to the pressure gradient across the beam thickness, and is the same relationship presented by equation (2.7).

Appendix B

Starting from equation (2.8) one can apply the displacement definition (2.16). Also considering a generic forcing function acting on the beam and recalling relations (2.10) and (2.13) the dynamics of the structure can be written as:

$$\sum_{i=1}^{N}\left\{X_i\ddot{T}_i + 2\lambda^2\left[\frac{D_i}{2\rho^*} - \frac{\mu}{\sigma h\rho^*}\left(\frac{X_i''}{X_i} + \sigma^2\right)\right]X_i\dot{T}_i + \lambda^2 c^2 X_i''''T_i\right\} = \frac{\lambda^2}{hw\rho^*}\mathrm{f}\left(x,t\right) \tag{B.1}$$

The orthogonality property of mode shapes can be used to uncouple the equation, *i.e.* multiply equation (B.1) by the j^{th} mode shape and integrate over the beam length, resulting in the following:

$$\mathbf{M}\ddot{\mathbf{T}} + \mathbf{C}\dot{\mathbf{T}} + \mathbf{K}\mathbf{T} = \mathbf{B} \tag{B.2}$$

where:

$$\mathbf{T} = \begin{bmatrix} T_1 \\ \vdots \\ T_N \end{bmatrix} \tag{B.3.a}$$

$$\mathbf{M} = \begin{bmatrix} \int_0^L X_1 X_1\,dx & \cdots & \int_0^L X_1 X_N\,dx \\ \vdots & \ddots & \vdots \\ \int_0^L X_N X_1\,dx & \cdots & \int_0^L X_N X_N\,dx \end{bmatrix} \tag{B.3.b}$$

$$\mathbf{C} = 2\lambda^2 \begin{bmatrix} \left(\frac{D_1}{2\rho^*} - \frac{\mu\sigma}{h\rho^*}\right)\int_0^L X_1 X_1\, dx & \cdots & \left(\frac{D_1}{2\rho^*} - \frac{\mu\sigma}{h\rho^*}\right)\int_0^L X_1 X_N\, dx \\ \vdots & \ddots & \vdots \\ \left(\frac{D_N}{2\rho^*} - \frac{\mu\sigma}{h\rho^*}\right)\int_0^L X_N X_1\, dx & \cdots & \left(\frac{D_N}{2\rho^*} - \frac{\mu\sigma}{h\rho^*}\right)\int_0^L X_N X_N\, dx \end{bmatrix} - \frac{2\lambda^2\mu}{\sigma h\rho^*} \begin{bmatrix} \int_0^L X_1 X''_1\, dx & \cdots & \int_0^L X_1 X''_N\, dx \\ \vdots & \ddots & \vdots \\ \int_0^L X_N X''_1\, dx & \cdots & \int_0^L X_N X''_N\, dx \end{bmatrix} \tag{B.3.c}$$

$$\mathbf{K} = \lambda^2 c^2 \begin{bmatrix} \int_0^L X_1 X_1''''\, dx & \cdots & \int_0^L X_1 X_N''''\, dx \\ \vdots & \ddots & \vdots \\ \int_0^L X_N X_1''''\, dx & \cdots & \int_0^L X_N X_N''''\, dx \end{bmatrix} \tag{B.3.d}$$

$$\mathbf{B} = \frac{\lambda^2}{hw\rho^*} \begin{bmatrix} \int_0^L X_1 \mathrm{f}(x,t)\, dx \\ \vdots \\ \int_0^L X_N \mathrm{f}(x,t)\, dx \end{bmatrix} \tag{B.3.e}$$

The orthogonality property of mode shapes is given by:

$$\int_0^L X_j X_i\, dx = \begin{cases} 0 \;\; if \;\; i \neq j \\ L \;\; if \;\; i = j \end{cases} \qquad i, j \in [1,2,...,N] \tag{B.4}$$

Also using the relation described by eq. (2.10) one can also write:

$$\int_0^L X_j X_i''''\, dx = \beta_i \int_0^L X_j X_i\, dx \tag{B.5}$$

Using relations (B.4) and (B.5) matrices **M**,**C** and **K** can be simplified to:

$$\mathbf{M} = L \begin{bmatrix} 1 & \cdots & 0 \\ \vdots & \ddots & \vdots \\ 0 & \cdots & 1 \end{bmatrix} \tag{B.6.a}$$

$$\mathbf{C} = 2\lambda^2 L \begin{bmatrix} \left(\frac{D_1}{2\rho^*} - \frac{\mu\sigma}{h\rho^*}\right) & \cdots & 0 \\ \vdots & \ddots & \vdots \\ 0 & \cdots & \left(\frac{D_N}{2\rho^*} - \frac{\mu\sigma}{h\rho^*}\right) \end{bmatrix} - \frac{2\lambda^2\mu}{\sigma h\rho^*} \begin{bmatrix} \int_0^L X_1 X''_1\, dx & \cdots & \int_0^L X_1 X''_N\, dx \\ \vdots & \ddots & \vdots \\ \int_0^L X_N X''_1\, dx & \cdots & \int_0^L X_N X''_N\, dx \end{bmatrix} \tag{B.6.b}$$

$$\mathbf{K} = \boldsymbol{\lambda}^2 c^2 L \begin{bmatrix} \beta_1^4 & \cdots & 0 \\ \vdots & \ddots & \vdots \\ 0 & \cdots & \beta_N^4 \end{bmatrix} \tag{B.6.c}$$

By transforming equation (B.2) into a state space representation a numerical method (*e.g.* Runge-Kutta) can be used to find the temporal solutions, $T_i(t)$, and consequentially determine the beam motion under a forced response.

$$\begin{bmatrix} \dot{\mathbf{T}} \\ \ddot{\mathbf{T}} \end{bmatrix} = \begin{bmatrix} \mathbf{0} & \mathbf{I} \\ -\mathbf{M}^{-1}\mathbf{K} & -\mathbf{M}^{-1}\mathbf{C} \end{bmatrix} \begin{bmatrix} \mathbf{T} \\ \dot{\mathbf{T}} \end{bmatrix} + \begin{bmatrix} \mathbf{0} \\ \mathbf{M}^{-1}\mathbf{B} \end{bmatrix} \tag{B.7}$$

Equation (B.7) also requires a set of initial conditions to determine the temporal function.

Appendix C

C.1. ASMC switching structures

Consider the following reaching state Lyapunov function:

$$\mathrm{V}_s = \frac{1}{2}\mathbf{s}^T\mathbf{s} \tag{C.1}$$

The time derivative of the reaching state Lyapunov function (V_s) is:

$$\dot{\mathrm{V}}_s = \mathbf{s}^T\dot{\mathbf{s}} = \mathbf{s}^T\mathbf{v} \tag{C.2}$$

An appropriate choice of reaching attractor input (**v**) has to satisfy the Lyapunov stability condition of a strictly negative time-derivative of the Lyapunov function. Equation (3.6) can be applied to (C.2) resulting in the following:

$$-\mathbf{s}^T b_0 sign(\mathbf{s}) = -b_0 \|\mathbf{s}\|^T < 0 \tag{C.3}$$

Because b_0 is strictly positive the choice of reaching attractor asymptotically stabilize the reaching dynamics.

C.2. Discrete sliding manifold

Equation (3.14) defines a Lyapunov-type of function for the current discrete state $\boldsymbol{\eta}$. The future $\boldsymbol{\eta}$ state can be easily written as:

$$V_{\eta}^{k+1} = \left(\boldsymbol{\eta}^{k+1}\right)^{T} \boldsymbol{\eta}^{k+1} \tag{C.4}$$

Condition (3.14) can also be expressed as the following:

$$V_{\eta}^{k+1} < V_{\eta}^{k} \tag{C.5}$$

Because both Lypunov-type equations, V_{η}^{k} and V_{η}^{k+1}, are smooth continuous functions the condition (C.5) could only be true if the H2 norm of the $\boldsymbol{\eta}^{k}$ state is bigger then the $\boldsymbol{\eta}^{k+1}$. In other words, if this condition holds the overall state magnitude is decreasing towards the origin. For a multi-dimensional state it is quite possible that one state diverges while the others are converging. This local instability is time-finite because once the other states reach the origin (or its vicinity) this unstable state will also start converging.

Condition (3.14) or (C.5) is a sufficient condition for the stability of the nonlinear difference system because if it holds true it enforces an overall decay of all states towards the origin. One interesting form of sufficient condition (C.5) is found by substituting the $\boldsymbol{\eta}$ discrete dynamics (equation 3.12) back into (C.5):

$$\left[\boldsymbol{\eta}^{k} + \boldsymbol{f}^{D}\right]^{T} \left[\boldsymbol{\eta}^{k} + \boldsymbol{f}^{D}\right] < \left(\boldsymbol{\eta}^{k}\right)^{T} \boldsymbol{\eta}^{k} \tag{C.6}$$

This later expression can be further simplified to assume the form given by equation (3.15).

C.3. DSMC switching structures

The resulting discrete reaching state dynamics after applying the feedback described by equation (3.18) will be:

$$\mathbf{s}^{k+1} = \mathbf{s}^{k} + \mathbf{v}^{k} \tag{C.7}$$

Stability of the discrete reaching dynamics can be guaranteed by the same sufficient condition stated for the $\boldsymbol{\eta}$ discrete dynamics. A Lyapunov-type of function can be defined for this state:

$$V_{s}^{k} = \left(\mathbf{s}^{k}\right)^{T} \mathbf{s}^{k} \tag{C.8}$$

The discrete sufficient condition, equation (3.15), to stabilize the reaching dynamics will be:

$$(\mathbf{v}^k)^T\left[2\mathbf{s}^k+\mathbf{v}^k\right]<0 \tag{C.9}$$

The choice of attractor input (3.19) applied to equation (C.9) results in the following:

$$-b_0\left[2-b_0\right](\mathbf{s}^k)^T\mathbf{s}^k<0 \tag{C.10}$$

Condition (C.10) is satisfied if b_0 is strictly positive and less then two.

C.4. Robust ASMC

Consider the same Lyapunov function described by equation (C.1), the time derivative of such function under the uncertain reaching dynamics (equation 3.24) will be:

$$\dot{V}_s=\mathbf{s}^T\dot{\mathbf{s}}=\mathbf{s}^T\left[\mathbf{v}+\boldsymbol{\Delta}\right] \tag{C.11}$$

where:

$$\boldsymbol{\Delta}=\delta_{\boldsymbol{\xi}}(\boldsymbol{\eta},\boldsymbol{\xi},\mathbf{u})-\frac{\partial\boldsymbol{\phi}}{\partial\boldsymbol{\eta}}\delta_{\boldsymbol{\eta}}(\boldsymbol{\eta},\boldsymbol{\xi}) \tag{C.12}$$

A choice of input attractor ($\mathbf{v}$) has to satisfy the Lyapunov asymptotical stability condition (a strictly negative rate), an intuitive choice is an input with opposite sign of the reaching state:

$$\mathbf{s}^T\left[\boldsymbol{\Delta}-\beta sign(\mathbf{s})\right]<0 \tag{C.13}$$

where β is a strictly positive value. If $\boldsymbol{\Delta}$ also has an opposite sign of the reaching state condition (C.13) is automatically satisfied, in case that is not true then the β value has to greater then $\boldsymbol{\Delta}$. If the infinity norm of $\boldsymbol{\Delta}$ can be written in term of an upper bound as done in equation (3.26), this inequality can be written as:

$$\begin{aligned}\beta &> \rho(\boldsymbol{\eta},\boldsymbol{\xi})+\lambda\beta \\ \beta &> \frac{\rho(\boldsymbol{\eta},\boldsymbol{\xi})}{1-\lambda}\end{aligned} \tag{C.14}$$

The attractor choice (equation 3.25) satisfies the inequality imposed by (C.14) which guarantees the Lyapunov condition (C.13) for asymptotical stability of the reaching state.

C.5. Robust DSMC

Using the same Lyapunov-type functional as (C.8) for the discrete reaching dynamics with uncertainties (eq. 3.29) one can obtain:

$$V_s^k = \left(\mathbf{s}^k\right)^T \mathbf{s}^k$$
$$V_s^{k+1} = \left(\mathbf{s}^{k+1}\right)^T \mathbf{s}^{k+1} = \left[\mathbf{s}^k + \mathbf{v}^k + \boldsymbol{\Delta}^k(\boldsymbol{\eta}^k, \boldsymbol{\xi}^k, \mathbf{u}^k, T_s)\right]^T \left[\mathbf{s}^k + \mathbf{v}^k + \boldsymbol{\Delta}^k(\boldsymbol{\eta}^k, \boldsymbol{\xi}^k, \mathbf{u}^k, T_s)\right] \quad \text{(C.15)}$$

where $\boldsymbol{\Delta}^k$ is defined by equation (3.31).

The sufficient condition for stability of the discrete reaching dynamics can be expressed as:

$$V_s^{k+1} < V_s^k \quad \text{(C.16)}$$

Substituting (C.15) into (C.16) it will result in:

$$\left[\mathbf{s}^k + \mathbf{v}^k + \boldsymbol{\Delta}^k\right]^T \left[\mathbf{s}^k + \mathbf{v}^k + \boldsymbol{\Delta}^k\right] < \left(\mathbf{s}^k\right)^T \mathbf{s}^k \quad \text{(C.17)}$$

Further simplification of equation (C.17) results in equation (3.30). The control design goal is to find a $\mathbf{v}^k$ expression that satisfies equation (3.30). Notice that such task is not trivial and a generic solution requires the knowledge of the uncertain term $\boldsymbol{\Delta}^k$, which by the problem definition is unknown.

In case the discrete attractor law for the uncertain-free system (eq. 3.19) is applied to equation (3.30) the presence of uncertainties does not allow for a mathematical proof of sliding manifold reaching ($\mathbf{s}^k$=0), instead it can only be shown that the discrete reaching state will be bounded to a region about the switching hyperplane. The following stability condition is defined after the choice of feedback given by eq. (3.19):

$$\left[-b_0\mathbf{s}^k + \boldsymbol{\Delta}^k\right]^T \left[2\mathbf{s}^k - b_0\mathbf{s}^k + \boldsymbol{\Delta}^k\right] < 0 \quad \text{(C.18)}$$

Which can also be written as:

$$b_0\left(b_0 - 2\right)\left(\mathbf{s}^k\right)^T \mathbf{s}^k + 2\left(1 - b_0\right)\left(\mathbf{s}^k\right)^T \boldsymbol{\Delta}^k + \left(\boldsymbol{\Delta}^k\right)^T \boldsymbol{\Delta}^k < 0 \quad \text{(C.19)}$$

Condition (C.19) is a sum of three terms: the first one is a strictly negative scalar term, as long as the gain b_0 belongs to the open interval (0,2); the second term it's a real value (either positive or negative); and the third one is a strictly positive uncertain scalar. An illustrative choice of b_0 is the unity because it vanishes with the second term of the attractor stability condition, resulting in the following:

$$\left(\mathbf{s}^k\right)^T \mathbf{s}^k > \left(\Delta^k\right)^T \Delta^k \tag{C.20}$$

For the particular choice of $\mathbf{v}^k$ the discrete reaching state will converge to until condition (C.20) is no longer satisfied, the bounded oscillation around the sliding manifold is defined in the literature as the quasi-sliding mode of operation [81].

Appendix D

The following represents the model properties utilized during the simulations and completely define the dynamic behavior of the JIAUV. These values were selected such that the response of the vehicle, calculated in subsection 4.1.4, is able to capture the basic behavior of this bio-inspired system.

$$\mathbf{M}^{Low} = \begin{bmatrix} 107.95 & 0.7711 & 0.7711 \\ 0.7711 & 107.95 & 0.7711 \\ 0.7711 & 0.7711 & 123.37 \end{bmatrix} (kg) \tag{D.1}$$

$$\mathbf{M}^{Hi} = \begin{bmatrix} 129.54 & 0.9253 & 0.9253 \\ 0.9253 & 129.54 & 0.9253 \\ 0.9253 & 0.9253 & 148.05 \end{bmatrix} (kg) \tag{D.2}$$

$$\mathbf{D}_{\mathbf{v}}^{Low} = \begin{bmatrix} 210 & 0.14 & 0.07 \\ 0.14 & 210 & 0.07 \\ 0.07 & 0.07 & 140 \end{bmatrix} (kg/s) \tag{D.3}$$

$$\mathbf{D}_{\mathbf{v}}^{Hi} = \begin{bmatrix} 300 & 0.20 & 0.10 \\ 0.20 & 300 & 0.10 \\ 0.10 & 0.10 & 200 \end{bmatrix} (kg/s) \tag{D.4}$$

$$\mathbf{J}^{Low} = \begin{bmatrix} 5.9721 & 0.0019 & 0.0041 \\ 0.0019 & 5.9699 & -0.004 \\ 0.0041 & -0.004 & 11.451 \end{bmatrix} (kg\,m) \tag{D.5}$$

$$\mathbf{J}^{Hi} = \begin{bmatrix} 7.4652 & 0.0024 & 0.0052 \\ 0.0024 & 7.4624 & -0.005 \\ 0.0052 & -0.005 & 14.3138 \end{bmatrix} (kg\,m) \tag{D.6}$$

$$\mathbf{D}_{\boldsymbol{\omega}}^{Low} = \begin{bmatrix} 1.00 & 0.01 & 0.005 \\ 0.01 & 1.00 & 0.005 \\ 0.005 & 0.005 & 0.50 \end{bmatrix} (kg\,m/s) \tag{D.7}$$

$$\mathbf{D}_{\boldsymbol{\omega}}^{Hi} = \begin{bmatrix} 2.00 & 0.02 & 0.01 \\ 0.02 & 2.00 & 0.01 \\ 0.01 & 0.01 & 1.00 \end{bmatrix} (kg\,m/s) \tag{D.8}$$

$$\mathbf{h}_{\mathrm{g}}^{Low} = \begin{bmatrix} 0 \\ 0 \\ 0.0008 \end{bmatrix} (m) \tag{D.9}$$

$$\mathbf{h}_{\mathrm{g}}^{Hi} = \begin{bmatrix} 0 \\ 0 \\ 0.008 \end{bmatrix} (m) \tag{D.10}$$

These properties vary with respect to time following the relation described by equation (4.13) and the period in which they oscillate is:

$$T = 3 \ (s) \tag{D.11}$$

The external forces to the system are described as:

$$\mathbf{F}_{\mathrm{g}} = \begin{bmatrix} 0 \\ 0 \\ -756.4491 \end{bmatrix} (N) \tag{D.12}$$

$$\mathbf{F}_{\mathrm{B}} = \begin{bmatrix} 0 \\ 0 \\ 748.8846 \end{bmatrix} (N) \tag{D.13}$$

The actuator properties are also given below. There are four actuators symmetrically distributed around the body coordinate system and they are identical, *i.e.* produce the same force under the same commanded amplitude.

$$\mathbf{h}_1 = \begin{bmatrix} 0.25 \\ 0 \\ 0 \end{bmatrix} (m) \tag{D.14}$$

$$\mathbf{h}_2 = \begin{bmatrix} 0 \\ 0.25 \\ 0 \end{bmatrix} (m) \tag{D.15}$$

$$\mathbf{h}_3 = \begin{bmatrix} -0.25 \\ 0 \\ 0 \end{bmatrix} (m) \tag{D.16}$$

$$\mathbf{h}_4 = \begin{bmatrix} 0 \\ -0.25 \\ 0 \end{bmatrix} (m) \tag{D.17}$$

$$\overline{\mathbf{F}}_i = \begin{bmatrix} 0 \\ 0 \\ 1 \end{bmatrix} (N) \quad i = 1,2,3,4 \tag{D.18}$$

$$\tilde{\mathbf{F}}_i = \begin{bmatrix} 0 \\ 0 \\ 0.8\sin\left(\dfrac{2\pi t}{T}\right) \end{bmatrix} (N) \quad i = 1,2,3,4 \tag{D.19}$$

The model parameters described from (D.1) to (D.19) can be used to simulate the kinematic behavior of the JIAUV. These properties create a virtual testing environment for different control strategies for the vehicle.

In order to access the robustness of the control laws being developed the model parameters feed into the controller are slightly different then the ones used in the "real model" being simulated. Also they are defined as constants and not as time-varying components as described by equation (4.13).

$$\bar{\mathbf{J}} = \begin{bmatrix} 7.462 & 0 & 0 \\ 0 & 7.462 & 0 \\ 0 & 0 & 14.31 \end{bmatrix} (kg\,m) \tag{D.20}$$

$$\bar{\mathbf{D}}_{\omega} = \begin{bmatrix} 2 & 0 & 0 \\ 0 & 2 & 0 \\ 0 & 0 & 1 \end{bmatrix} (kg\,m/s) \tag{D.21}$$

$$\bar{\mathbf{h}}_g = \begin{bmatrix} 0 \\ 0 \\ 0.0081 \end{bmatrix} (m) \tag{D.22}$$

There are also the estimated actuators properties:

$$\bar{\mathbf{h}}_1 = \begin{bmatrix} 0.2 \\ 0 \\ 0 \end{bmatrix} (m) \tag{D.24}$$

$$\bar{\mathbf{h}}_2 = \begin{bmatrix} 0 \\ 0.2 \\ 0 \end{bmatrix} (m) \tag{D.25}$$

$$\bar{\mathbf{h}}_3 = \begin{bmatrix} -0.2 \\ 0 \\ 0 \end{bmatrix} (m) \tag{D.26}$$

$$\bar{\mathbf{h}}_4 = \begin{bmatrix} 0 \\ -0.2 \\ 0 \end{bmatrix} (m) \tag{D.27}$$

$$\bar{\mathbf{F}}_i = \begin{bmatrix} 0 \\ 0 \\ 1.1 \end{bmatrix} (N) \quad i = 1,2,3,4 \tag{D.28}$$

$$\tilde{\mathbf{F}}_i = \begin{bmatrix} 0 \\ 0 \\ 0.35\sin\left(\frac{2\pi t}{T}\right) \end{bmatrix} (N) \quad i = 1,2,3,4 \tag{D.29}$$